Observatoire de Neuchâtel - Université de Neuchâtel

Backscatter Lidar Measurement of Aerosol Stratification in the Atmosphere

---

Thèse présentée à la Faculté des Sciences
pour l'obtention du grade de docteur ès sciences
par:

Giovanni Martucci
Physicien diplômé de l'Université de Padoue, Italie

acceptée le 18 juillet 2006 par les membres du jury:

Prof. P. Thomann	Rapporteur, directeur de thèse
Prof. P. Seitz	Co-rapporteur
Prof. Dr. H. Richner	Co-rapporteur
Prof. R. Daendliker	Co-rapporteur
Dr. V. Mitev	Co-rapporteur

IMPRIMATUR POUR LA THESE

Backscatter Lidar Measurement of Aerosol Stratification in the Atmosphere

Giovanni MARTUCCI

UNIVERSITE DE NEUCHATEL

FACULTE DES SCIENCES

La Faculté des sciences de l'Université de Neuchâtel,
sur le rapport des membres du jury

MM. P. Thomann (directeur de thèse),
P. Seitz, V. Mitev, R. Dändliker et
H. Richner (ETH Zürich)

autorise l'impression de la présente thèse.

Neuchâtel, le 10 octobre 2006

Le doyen :

UNIVERSITE DE NEUCHATEL
FACULTE DES SCIENCES
Secrétariat-décanat de la faculté
Rue Emile-Argand 11 - CP 158
CH-2009 Neuchâtel

J.-P. Derendinger

Faculté des Sciences
Rue Emile-Argand 11 CP 158 CH-2009 Neuchâtel
Téléphone : +41 32 718 21 00 Fax : +41 32 718 21 03 E-mail : secretariat.sciences@unine.ch www.unine.ch

Key words: Elastic Backscatter Lidar; Atmospheric Aerosol; Boundary-Layer; Stratification; Upper Troposphere and Lower Stratosphere; Polar Stratospheric Cloud; Ultra-Thin Tropical Cirrus

Mots clés: Lidar élastique à retro-diffusion, Aerosol Atmosphérique, Stratification, Couche-Limite, haute troposphère ainsi que dans la basse stratosphère, nuages polaires stratosphériques, cirrus tropicaux ultra fins

Abstract: The atmospheric aerosol, its stratification and the principal dynamics controlling the air exchange at the top and the base of the aerosol layers are of key importance for understanding critical atmospheric phenomena such as the transport and impact of air pollution, the destruction of the ozone layer and the evolution of the greenhouse effect. In particular, it is the detection of stratification within the atmospheric boundary layer, the lower Troposphere and the regions around the Tropopause that are of importance to comprehending these phenomena. Elastic backscatter lidar is a novel tool promising to complement and partially to replace established atmospheric measuring techniques for quantifying these effects. The present thesis is investigating the theoretical and practical relevance of lidar in fulfilling this promise.

The thesis performs an evaluation of two lidar methods to identify the structure of the boundary layer as well as their validation with respect to traditional methods such as radiosondes employed in atmospheric measurements. The validation shows that the lidar derived structure of the boundary layer is congruent with the structure derived from radiosonde temperature measurements. This result substantiates the use of elastic backscatter lidar for considerably advanced boundary layer monitoring compared to presently accepted methods. These measurements are then used to determine the frequency of the boundary layer top height variation. It is demonstrated that this method permits the identification of gravity waves through the boundary layer, consequently allowing the use of lidar for the investigation of the vertical exchange of pollution constituents. The monitoring of the height of the boundary layer has subsequently been carried out over a one-year period of measurements above the urban site of Basel, Switzerland. This campaign demonstrates the key role of lidar in conducting measurements over such long intervals, which is otherwise not possible with established instruments.

The thesis provides complementary results collected by two airborne lidars in the upper Troposphere and the lower Stratosphere. The detection of specific clouds in this atmospheric region has critical importance for two aspects in the stratospheric ozone balance: polar stratospheric clouds are responsible for initiating ozone destruction, and the ultra-thin optical cirrus are linked to the water and radiation budget as well as to large-scale transport.

The significance of the present thesis lies in conclusively demonstrating that elastic backscatter lidar contributes with both unique and complementary information to the present inventory of atmospheric instruments. This is substantiated by showing that the obtained results allow straightforward interpretation of the probed atmosphere, where they are particularly advantageous in terms of simplicity, reliability and information content, with respect to traditional, established methods.

A ma famille

A ma précieuse B(e)

Acknowledgments

The work on this thesis was funded by the Swiss National Science Foundation and by the Canton of Neuchâtel.

My thesis has been realised thanks to many people. I would like to convey my gratitude to all of these and especially to:

Dr. Valentin Mitev who gave me all the knowledge in the lidar field and who enriched me in both professional and human fields.

Dr. Renaud Matthey, the first person I met at the beginning of this *experience*. He taught me all that I actually know in programming Matlab and he has always been an important friend for me.

Prof. Pierre Thomann, my thesis director. I will always thank him for the precious help he gave me especially during the last year of thesis and for the wonderful *mountain* moments we spent together with all our friends.

Prof. Hans Richner, for his scientific support during these four years of PhD work.

Dr. Mathias Rotach, for his attention and support during BUBBLE data study.

The colleagues of the University of Basel working in BUBBLE, for the surface meteorological measurements in this Project.

The Aerological Station of Meteosuisse in Payerne, for the upper atmosphere data they provided for my study.

The team of the aircraft M55 "Geophysica", who shared with me all the successes and the problems of the scientific campaigns through the last 4 years.

René Maurer, for his precious technical support and for his friendship.

A special thanks goes to all my friends here. They have been the most important things I have had in these four years here.

Thanks to Gianni, Véronique, Natascia, Sylvain, Roberto, Caroline, Rudi, Steve, Valérie, Christian, Evelina, Ariane, Lydie, Roger, Monique, Patrick, Yvan, Joanna, Marianne, Carole, Christoph and Marion.

Thanks to all my Italian friends spread throughout the world, working like me as PhD students or involved in other scientific experiences. We began together and I am proud to be part of each of you: Ale, Spud, Phelt, Grigio, Marco, Ste, Doc, Daaavis, Dario Cua, we'll be again all together one day!

Finally, my *family* and my beloved *B(e)*. Both of you provided me the strength to accept and to continue this experience through all difficulties. This result is important for me, but even more because now it is part of you.

Papà, Mamma, it is only thanks to you if I could arrive here.

Table of contents

Chapter 3 51

Frequency of boundary-layer top fluctuation in convective and stable cases 51

Chapter 4 73

Daily cycle development of urban boundary-layer. BUBBLE field campaign 73

Preface

Light detection and ranging (lidar) is a technology that allow one to determine the distance to an object or a surface using laser pulses. Lidar is one of the principal active remote sensing instruments. Together with the radiowave detection and ranging (radar) and the sound detection and ranging (sodar), it may provide detailed description of the atmosphere. Actually, lidar offers to the atmospheric science the possibility to use continuous, highly resolved measurements with covered height range potentially up to 100 km. From its beginnings till present, lidar had multiple applications in atmospheric science, when it always operated in the earth's atmosphere as an airborne or ground-based instrument. Now, progresses in technology allow to install lidars on satellites for Earth observation from orbit (i.e., NASA project: LITE; CNES project: CALIPSO). Projects exist also to set recently developed micro-lidars on spacecrafts for probing of extra-terrestrial planetary atmospheres (Carswell, et al, 2004).

Lidar can be used to investigate either very fast processes concerning turbulence, or daily development of the lower atmospheric layers with attention to macroscopic changes in their thickness. Use of lidar is important also in monitoring of pollution above urban sites and ozone flux. The lidar can provide fundamental atmospheric quantities, like aerosol and cloud distribution, molecular density profiles and then temperature and pressure estimations. Humidity and water vapour mixing ratio detected by lidar are among the useful atmospheric parameters detected by a lidar, as well as it is the wind (Measures, 1984; Weitkamp, 2005).

The primary advantage of the lidar is in the capabilities for remote sensing, i.e. a lidar can study atmospheric volumes at far ranges with no need to be moved. In addition to this, the reasons that determine the interest to the lidar technique with respect to the traditionally employed methods for atmospheric measurement, can be summarised in the following points:

i. The lidar provides the altitude (or range) profile of the measured value in selected and determined direction.

ii. The lidar provides continuous measurement and then gives the possibility to measure the temporal variation of the altitude-resolved atmospheric variables studied by the scientific community, i.e., a larger amount of data are available.

For the elastic backscatter lidar these advantages are applied in areas where the aerosol particles are of a critical importance either as a tracer to "visualise" the atmospheric processes or as a specific object of study (pollution, radiative and chemical balance of the atmosphere).

Aerosols can be envisioned as an aggregation of particles consisting of an integral number of molecules or monomers. The smallest aerosol particle could be defined as a system of two molecules or two monomers. Aerosols of larger size are generally referred to as *particulate* (or particulate matter, i.e., PM), and are tiny particles of solid or liquid suspended in the atmosphere. The atmospheric aerosol have a large number of sources, from both marine and continental environments (Seinfeld, 1986, Part III). The aerosol size ranges from less than 10 nanometers to more than 100 micrometers in diameter. This range of sizes represent scales from a gathering of a few molecules to the size where the particles no longer can be carried by the gas, but starts to sediment. With respect to lidar detection, this last is the case of fogs and clouds that can be regarded as aerosols when the size of droplets and crystals does not exceed the values that would activate sedimentation. Aerosols can be naturally originated, as from volcanoes, dust storms, forest and grasslands, or they can be injected in the atmosphere by anthropogenic processes. Presently, averaged over the globe, the aerosols produced by humans activities account for approximately 10% of the total amount of the atmospheric aerosol. The aerosols are wind-blown from their sources and they spread over very large atmospheric regions; for instance, one gram of aerosol particles have an average surface of 10 m^2. A consequence of the large spatial distribution of the aerosol in the atmosphere is the effect that it has on the climate by changing the way the radiation is transmitted through the atmosphere. The Intergovernmental Panel on Climate Change, IPCC, says: "While the radiative forcing due to greenhouse gases may be determined to a reasonably high degree of accuracy... the uncertainties relating to aerosol radiative forcings remain large, and rely to a large extent on the estimates from global modelling studies that are difficult to verify at the present time". This is a motivation to put efforts in studying the aerosol distribution through the atmosphere and to collect large amount of data representing the temporal evolution of principal atmospheric variables, useful also for numerical models assessments.

Another motivation in research and development of lidar applications comes from the fact that aerosol is a tracer for different atmospheric masses across the globe. The continuous monitoring, in time and altitude, of these air masses can provide information of key atmospheric processes not only in the region of probing, but also on the larger scales (i.e., air masses back-trajectories).

The part of the atmosphere where the aerosol is most present extends from the earth's surface up to the lower stratosphere. In the picture below is outlined the vertical structure of the first 100 km within this atmospheric portion. In two regions the lidar studies are of particular interest for direct effects on human lives: the lower troposphere and the altitudes around the tropopause (i.e., upper troposphere and lower stratosphere).

The part of atmosphere where most of the life processes develop corresponds to the first few kilometres above the ground level, within the troposphere. The lower boundary of this atmospheric part is the earth's surface that determines the principal dynamics of heat, moisture or momentum transport. Based on a qualitative definition (Stull, 1988), the boundary-layer (BL) is "that part of the troposphere that is directly influenced by the presence of the earth's surface, and responds to surface forcing with a timescale of about one hour or less". Because of the close interaction with the surface, the BL responds to topography with horizontal gradients in the vertical buoyancy and moisture fluxes. Complex terrain does not only mean complex topography as hill/mountain range with narrow valleys and coarse peaks, but also rough profiles of city buildings or variation of the surface type (soil, water, desert, etc…). During day and in cloud-free conditions, the solar radiation is homogeneously distributed on the surface. On the other hand, horizontal gradients of the radiative absorption happen due to different surface cover (grass, trees, asphalt, etc…) and different albedo. When surface is made by alternate ground and water, horizontal gradients in evaporation are expected as well. Different convergence and divergence zones, due to convective processes developing at the ground surface, are structures almost regular above flat terrain. Rising thermals surrounded by downdraft zones have a complex horizontal periodicity above uneven surfaces making the BL depth to be spatially highly variable. The study of the temporal evolution of the BL above both rural and urban terrains is important to understand the mechanisms of air-exchange at the interface between BL and free troposphere (FT).

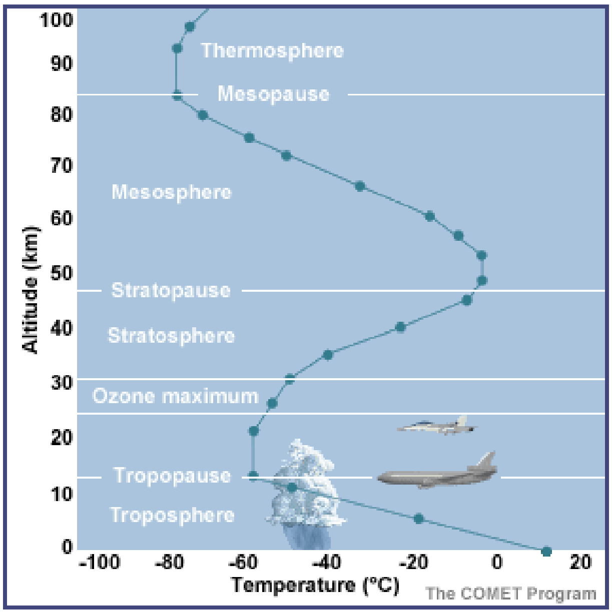

Fig. 1. Vertical structure of the atmosphere. In the first atmospheric layer, the Troposphere, all the life processes take place. Dark-blue line with filled circles is the vertical temperature profile through the atmosphere.

The aerosol stratification and dynamics within the BL are determined, in convective conditions, by the intensity of the air-mixing (mixed layer, ML) and, in stable, nocturnal conditions, by the vertical profile of the aerosol at the lower levels (nocturnal boundary-layer, NBL). The ML and the NBL are both part of the BL and represent, respectively, the diurnal and nocturnal layer development within the BL. The ML depth (MLD) and the height of the NBL are then important for the characterization of the air exchange with the free troposphere and for an estimation of the aerosol dilution within the BL (Stull, 1988; McIlveen, 1992; Siebert et al., 2001). A way to study the temporal and vertical evolution of BL top height through day and night is to use a lidar. The lidar, as an active probing instrument, is principally based on the vertical gradient of two variables: the extinction and the backscatter coefficients. There is relation between the aerosol vertical profile and the vertical gradients of atmospheric extinction and backscatter (Measures, 1984). Therefore a lidar is a suitable device to measure the atmospheric stratification using aerosol as a tracer. Due to its operation principles, continuous monitoring can be ensured both in time and space. The possibility to have long measurement of the status of the atmosphere is important not only for atmospheric science, but also for the ecological control of polluted areas. Actually, pollution above urban sites and countryside affects the quality of life and needs to be monitored in continuous mode.

Since the introduction of the lidar, scientists tried to optimize the various applications of this remote instrument to the study of the lower troposphere. The lidar signal gradient provides information about the structure of the BL, as demonstrated first by Russel (1974). Another method, the standard deviation, using also the backscatter lidar signal for the BL height evaluation was introduced by Hoopar and Eloranta (1986), and further developed by Piironen and Eloranta (1995). In this thesis attention will be on these two methods, i.e., the gradient and the variance. For the gradient, one single lidar backscatter profile is sufficient to give an estimation of the altitude and thickness of an atmospheric layer. The variance method needs several lidar profiles in order to compute the spatial (or temporal) variation of the lidar backscatter with respect to a mean value. Both methods are based on the lidar backscatter signal properties and need neither a priori assumption on the shape of the atmospheric layer, nor any imposed thresholds.

The detection of high altitude clouds is another example of how a lidar can determine the atmospheric stratification using the optical properties of the light scattering when the mean value of the extinction is negligible compared to the backscatter coefficient. One atmospheric region where this condition is achieved is the upper troposphere and the lower stratosphere (UTLS), i.e., a region comprised between about 8 and 30 km. The UTLS recently attracts attention because of the phenomenon, usually referred as "ozone problem". It is the polar lower stratosphere, where the processes leading to ozone destruction take place. These processes are initiated with a photo-chemical reaction destroying the CFCs (chlorofluorocarbons), taking place on the surface of tiny aerosol particles, forming the polar stratospheric clouds (PSCs) (Browell et al., 1990). The main ingredients in the ozone destroying reaction are transported to the stratosphere in the tropical UTLS, via strong convective processes. The physical means through which chemicals are convectively injected in the UTLS are deep cumulus clouds. These clouds and especially their tops are a source of extensive deck of sub-visible cirrus clouds as the ultra-thin tropical tropopause clouds (Peter et al, 2002). The latter play also an important role in the stratospheric water vapour and radiative balance.

Investigations of the UTLS and the processes concerning the ozone depletion are normally carried out by aircraft transported-instruments measuring over large geographical areas. In fact, the most interesting geographic regions for UTLS processes are without the proper infrastructure, it is then necessary to reach these regions also at large distances from scientific base-camps. In addition, the attractive cloud features are frequently of large expands (up to several hundreds kilometres surface), it is then useful to probe these vast areas in relatively short time with an aircraft prepared for measurements.

Objectives and structure of the thesis

This thesis consists of five chapters which may be grouped in three parts. The first part includes Chapter 1 and presents the fundamentals of lidar theory as well as an introduction to the principal lidar methods used to process the data in Chapters 2 to 5. At the end of the chapter are also presented the four lidars employed to obtained the measurements shown in Chapters 2 to 5. The second part comprises Chapters 2, 3 and 4 and shows three different approaches to study the BL during both day and night (ML and the NBL). The third part is represented by Chapter 5 and concerns four airborne scientific campaigns in which the UTLS is studied by two compact airborne lidars. A chapter of conclusion follows the other chapters summarizing and giving a final interpretation of the achieved results. A list of acronyms is provided after the Chapter of conclusion and before bibliography.

My PhD work began in July 2002 with the objective to demonstrate the applicability and the advantages of the backscatter lidar in typical atmospheric study cases.

This objective follows the state-of the-art and the set targets in the lidar studies: the backscatter lidar could be realized as a reliable instrument. Before including the lidar in the inventory of the atmospheric instruments it is necessary to validate the critical lidar results with respect to the presently accepted methods and to demonstrate that the information from the lidar leads to a new and complementary knowledge.

To fulfil this objective of the thesis it was necessary:

i. to select atmospheric case studies where application of the backscatter lidar monitoring is expected to provide new knowledge.

ii. To develop computational algorithms and codes to process the accumulated backscatter lidar data during the measurement campaigns in which our lidars participated.

iii. To validate and analyze the obtained results by applying and adapting the backscatter lidar theory to the different atmospheric conditions in which our lidar worked.

As a result of my PhD work, this thesis intends to demonstrate the capabilities of a backscatter lidar in describing specific regions of the atmosphere and their processes under different meteorological and environmental conditions.

My thesis consists of five chapters which may be grouped in three parts. The first part includes Chapter 1 and presents the fundamentals of lidar theory as well as an introduction to the principal lidar methods used to process the data in Chapters 2 to 5. At the end of the chapter, the four lidars used in the measurements shown in Chapters 2 to 5 are also presented. The second part comprises Chapters 2, 3 and 4 and investigates the backscatter lidar approach to study the BL during both day and night (ML and the NBL). The third part is represented by Chapter 5 and presents airborne lidar results obtained in four scientific campaigns to study UTLS. A chapter of conclusion summarises the relevance of the results and their perspectives.

As presented above, the elastic backscatter lidar signal is determined by the altitude profile of the atmospheric aerosol. Using aerosol as a tracer for convective and stable processes, the backscatter signal provides information about the BL stratification and dynamics. Then, concerning the lower troposphere, attention will be on the detection of the MLD and the NBL height. The information about the atmospheric stratification and cloud optical properties is retrieved from lidar data using the developed algorithms for signal processing and noise reduction. Three different approaches have been used to analyze the BL in Chapters 2, 3 and 4:

i. A number of diurnal and nocturnal cases have been collected in a single dataset to form a statistic and to compare lidar data with radiosonde measurements of BL height.

ii. Single case studies have been investigated to study the frequency of rising and sinking ML and NBL tops.

iii. Continuous monitoring of the urban BL above the city of Basel have been carried out for one year and compared, for some cases, to meteorological in situ parameters.

Detection of clouds in UTLS is presented in Chapter 5 and was performed using two compact automated lidars on-board a high altitude scientific aircraft during four airborne field campaigns. The common objective of these field campaigns is to improve the knowledge about the principal mechanisms leading to the ozone depletion in polar regions. To acquire this knowledge it is necessary to understand and realize the role of some trace gases transported by strong convection into the tropical stratosphere and then to polar regions. Different tropospheric and stratospheric clouds were the effective targets of the lidar measurements during the flights survey occurred in polar and tropical regions.

Chapter 1

Backscatter lidar theory and methods

The first chapter of this thesis will define a set of fundamental equations of the lidar theory. Lidar applications in atmospheric science are based on these equations and on the approximation of the principal variables according to the different scenarios in which a lidar is deployed for measurements. At the end of the chapter an introduction is given to the principal lidar methods used to process the backscatter signal and a description of the instruments arranged for measurements in the different studies presented through the thesis.

1.1. What a lidar is

Lidar, laser radar, optical radar, and ladar are all names used for "radar" systems utilizing electromagnetic radiation at optical frequencies. The radiation used by lidar is at wavelengths 10^4 to 10^5 times shorter than those used by conventional radar. Radiation scattered by the target (and the atmospheric volume) is collected and processed to yield information about the target and the path to the target. Early conventional radars and lidars observed only the intensity of the collected radiation and the time delay from transmission to collection. Modern lidars also observe intensity and time delay. However some, called coherent laser radars (CLR's), record information about the phase of the scattered radiation with respect to a local reference. Lidars may be continuous-wave (CW) or pulsed.

Pulsed lidars use much higher power levels during the laser pulse than can be maintained with a CW laser, producing higher signal-to-noise ratios for the collected radiation. Pulsed lidars are usually chosen for long-range remote sensing and when long signal integration is impractical. For a single laser-pulse emitted in the atmosphere a simplified description of the lidar principles and its interaction with the atmospheric targets is outlined in Fig. 1.1. A portion of the propagating light interacts with the various elements constituting the atmosphere – like molecules, particles, clouds, … – and is scattered, while the rest of the light travels further. The beam is progressively attenuated with the distance in the process of propagation. The backscatter light is collected by the telescope of the instrument, detected and converted into electrical signal. This electrical signal is then measured. Acquired data are finally stored on a mass memory and processed by a computer. The time difference between the moment the laser pulse is emitted and the reception of the light, often called "time-of-flight" is related by the known speed of the light to the range reached by the pulse. For instance in 1 µs the light covers 300 m, meaning that it has been backscattered at a range of 150 m. On the other side, the intensity of the signal contains information about the scattering item, i.e. the probed atmospheric layer. The lidar signal profile is obtained by measuring – after the laser pulse was emitted – the signal at several moments, corresponding at several ranges or altitudes (*r* or *h* in Fig. 1.1).

The difference between a lidar and a range-finder is exactly at this point. A range-finder also emits a light pulse and detects the part backscattered by a solid or liquid target. However it does not measure a profile, what means several time-of-flights, like the lidar. It only measures the time spent till a signal larger than a certain value is detected.

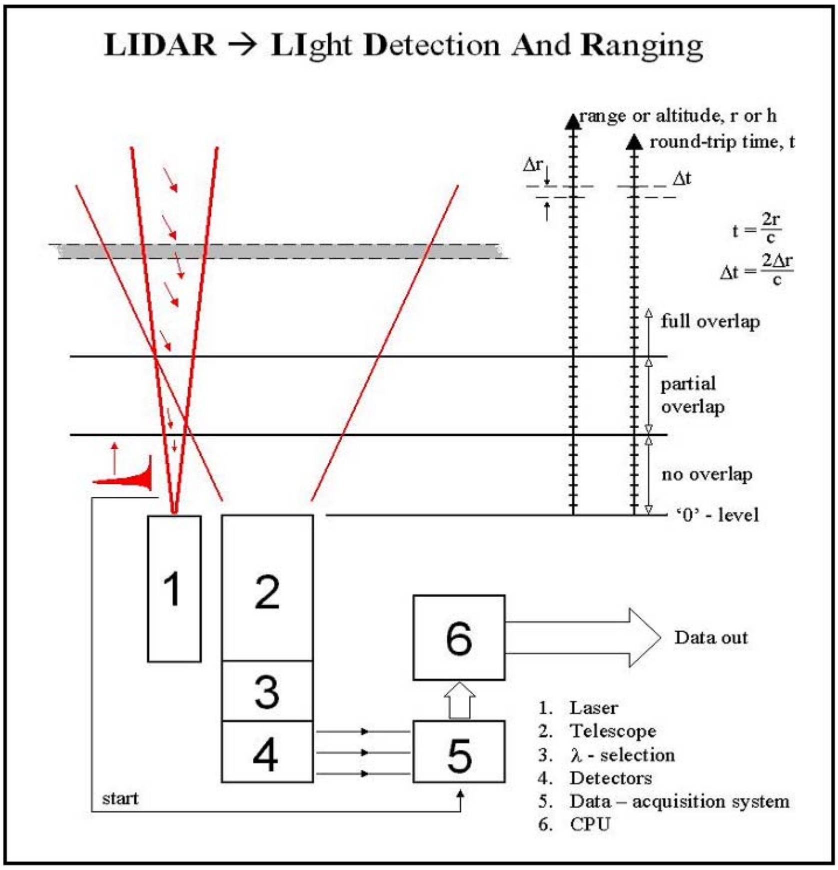

Fig. 1.1. Lidar measurement principle

Various type of lidars were developed during the last 40 years. Scattering is the physical property of particles and radiation characterizing the different lidar instruments. In scattering theory, Rayleigh and Mie effects represent one specific form of scattering, the elastic one. Rayleigh effect exists when the probing wavelength λ, emitted by the lidar, is much greater than the mean diameter of the probed atmospheric targets. A distribution of scattering centres with diameters less than $10^{-1}\cdot\lambda$ is an ideal pattern to engender Rayleigh scattering. Lidars using the Mie scattering are based on the assumption that the scattering centres (with mean value of diameters greater than those of Rayleigh) are almost spherical. The theory holds for exception in shape as for spheroids and ellipsoids, but not for arbitrary targets with no-spherical symmetry. The two kinds of scattering let unchanged the energy transported by the incident wavelength and preserve then the frequency after being scattered by the target. Another type of lidar is the Raman lidar, based on the Raman scattering. In this case incoming energy is not the same as the one backscattered along the same path. The scatter is then inelastic. In Fig. 1.2 is sketched the laser beam propagation in the atmosphere experiencing Rayleigh/Mie or Raman scattering.

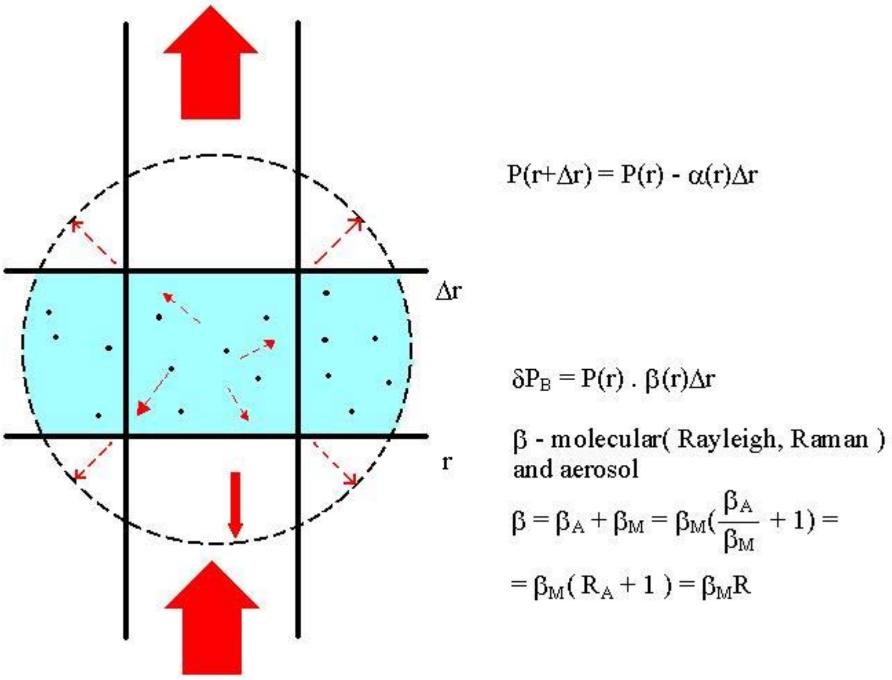

Fig. 1.2. Outline of beam propagation and scattering in the atmosphere. Equations on the right side represent the received power (δP_B) from the range interval (r, r + Δr) impinging onto the receiver and the total (molecular and aerosol) backscatter coefficient, β. The meaning and the use of these equations are presented in larger explanation in Sect. 1.6.3 and in Chapter 5.

This thesis work shows data and results based on the elastic backscatter lidar signal. The lidar theory overview given further has then to be understand basing on Rayleigh and Mie scattering only.

1.2. Backscatter lidar equation

The lidar equation is for the power of the light received by the detector of the instrument. Here the lidar equation is derived for the case of elastic atmospheric backscatter only. It is assumed that the wavelength of the emitted and detected radiation is the same, λ (elastic scattering from the target), and that λ is out of the absorption bands of the atmosphere. Also only the range r is taken into account, not the vector position $\boldsymbol{r}$, what implies uniformity of the radiation and target medium.

When a short laser pulse of wavelength λ is emitted into the atmosphere, the detected power P of the backscattered light at distance r from the instrument may be expected to be a function such as

$$P(r,\lambda) = P(r,\lambda,S,\beta,\alpha). \tag{1-1}$$

Here P depends on the instrument parameter set S, on the nature of the interaction β between the laser light and the target medium at range r and on α. The coefficient α expresses the way the laser light is attenuated when propagating in the atmosphere being scattered in all directions by the atmospheric volume in the line of propagation.

Let the temporal shape of the laser pulse be approximated by a rectangular laser pulse of energy E_0, duration τ_L, emitted at time 0. If $A_L(r)$ is the area on which the laser light is distributed at range r, the laser irradiance I (in $[W/m^2]$) over $A_L(r)$ is given by

$$I(r,\lambda) = \frac{E_0 T(\lambda,r)}{\tau_L A_L(r)}, \tag{1-2}$$

$T(r,\lambda)$ represents the atmospheric transmission factor at wavelength λ from instrument position to range r. It results from the Beer-Lambert law that

$$T(r,\lambda) = \exp\left(-\int_0^r \alpha(r',\lambda)dr'\right). \tag{1-3}$$

The extinction coefficient α (in $[\mathrm{m}^{-1}]$) and the volume backscattering coefficient β (in $[\mathrm{sr}^{-1}\mathrm{m}^{-1}]$) are expressed as

$$\alpha(r,\lambda) = n(r)\int d\Omega \frac{d\sigma(\lambda)}{d\Omega} \quad \text{and} \quad \beta(r,\lambda) = n(r)\left[\frac{d\sigma(\lambda)}{d\Omega}\right]_{\Omega=\pi}, \tag{1-4}$$

where $n(r)$ is the scatterer number density at range r and $d\sigma(\lambda)/d\Omega$ its differential scattering cross-section at wavelength λ (in $[\mathrm{m}^2\mathrm{sr}^{-1}]$).

In the approximation of single scattering, for the chosen shape of the laser pulse, at time t $(=r/c)$, where c is the speed of the light in the air, only the volume $V = \mathrm{A_L}(r)\cdot c\tau_L/2$

extending from ranges $c(t-\tau_L/2)$ to ct contributes to the radiation power I_b backscattered in the acceptance solid angle $d\Omega_b(r)$ of the receiver:

$$I_b(r,\lambda) = I(r,\lambda)\beta(r,\lambda)V d\Omega_b(r) \quad \text{with} \quad d\Omega_b(r) = \frac{A}{r^2}, \tag{1-5}$$

where A is the effective area of the receiver lens or telescope. The range-dependant parameters have been regarded as constant since r is generally much greater than $c\tau_L/2$.

If K is a constant expressing the overall optical efficiency of the lidar transmitter and receiver sub-systems, and $\eta(\lambda)$ is the wavelength-dependent quantum efficiency of the detector, the detected signal power P is

$$P(r,\lambda) = K\eta(\lambda)O(r)I_b(r,\lambda)T(r,\lambda). \tag{1-6}$$

$O(r)$ is the overlap function corresponding to the part of the laser irradiation area $A_L(r)$ within the field of view of the receiver optics. Rewriting (1-6) with the equations (1-2) to (1-5), the lidar equation is obtained:

$$P(r,\lambda) = E_0 K\eta(\lambda)O(r)\frac{A}{r^2}\frac{c}{2}\beta(r,\lambda)\exp\left(-2\int_0^r \alpha(r',\lambda)dr'\right). \tag{1-7}$$

From the detected power, we may derive the energy received by the detector during the "integration period" τ:

$$E(r,\lambda) = E_0 K\eta(\lambda)O(r)\frac{A}{r^2}\frac{c\tau}{2}\beta(r,\lambda)\exp\left(-2\int_0^r \alpha(r',\lambda)dr'\right). \tag{1-8}$$

$E(r,\lambda)$ is the energy of the signal backscattered from the range interval $[r, r+\Delta r[$ where $\Delta r = c\tau/2$. The integration time τ, and thus Δr, is given by the lidar set-up (detector, acquisition system). Δr is called "range resolution".

1.3. Approximations in the lidar equation

The lidar equation has been derived using simplifying and approximating assumptions. They are here briefly discussed. Extended forms of the equation are also presented.

In the computation of the equation (1-7) the detector response time τ_D has been neglected. This is possible only if $t >> \tau_D$. In the general case, the range resolution is limited to $c(\tau_L+\tau_D)/2$.

As the receiver optics of a lidar is usually focused at infinity, the radiation from a target plane located at short or intermediate ranges from the instrument will not be focused onto the focal plane. Instead it forms a diffuse region of illumination on this plane. The presence of a limiting aperture (diaphragm, detector of small size) in the focal plane can reduce the amount of detected power. This effect is referred to as "geometrical signal compression", and may be accounted by an upgraded overlap function called also "geometrical form factor".

The extinction coefficient α and the volume backscattering coefficient β may be considered as the sums of the contributions of molecules and aerosol particles:

$$\alpha(r,\lambda) = \alpha_{mol}(r,\lambda) + \alpha_{aer}(r,\lambda) \quad \text{and} \quad \beta(r,\lambda) = \beta_{mol}(r,\lambda) + \beta_{aer}(r,\lambda)\,, \tag{1-9}$$

where the subscripts *mol* and *aer* represent, respectively, the molecular and aerosol contributions.

In case λ coincides with an absorption band of an atmospheric species, the integrand in the transmission factor expression (1-3) must be changed:

$$\alpha(r',\lambda) \longrightarrow \alpha(r',\lambda) + n(r')\sigma(\lambda) \tag{1-10}$$

where $n(r)$ is the number density of the absorbing species at range r, and $\sigma(\lambda)$ its absorption cross-section at wavelength λ.

For inelastic (Raman) scattering, the wavelength of the backscattered radiation λ_e is not the same as the wavelength of the incident radiation λ_i . In this case, β is the backscattering coefficient based on the differential cross section of the light-molecule interaction inducing the wavelength shift (cf. equation (1-4)). The extinction part of the lidar equation (1-7) is then

$$\exp\left(- \int_0^r \left(\alpha(r',\lambda_i) + \alpha(r',\lambda_e) \right) dr' \right). \tag{1-11}$$

An important difference between ground-based lidars and satellite or air-borne ones is the *surface return*. For a diffuse Lambertian extended[1] hard target or surface, which scattering occurs only into a single hemisphere the emitted radiance (in [$\mathrm{Wm^{-2}sr^{-1}}$]) is (Jelalian, 1991)

$$I(\vartheta) = I(\vartheta = 0)\cos\vartheta\,, \tag{1-12}$$

where ϑ is the angle with the surface normal vector. The total emitted radiation R (irradiance) is then

$$R = \int I(\vartheta)d\Omega = \pi I(0)\,. \quad \text{Thus} \quad I(0) = \frac{R}{\pi}\,. \tag{1-13}$$

---

[1] Here "extended" means that the surface of the target is larger than the footprint of the laser beam. Wouldn't it be the case, that the response would depend on the scattering area and on the inverse fourth power of the range, r^{-4}.

With this result, the lidar equation of a diffuse Lambertian extended target[2], like a ground surface, is given by

$$P(r,\lambda)=\frac{E_0}{\tau_L}K\eta(\lambda)O(r_{sur})\frac{A_t}{r_{sur}^2}\frac{a}{\pi}\exp\left\{-2\int_0^{r_{sur}}\alpha(r')dr'\right\} \quad \text{if } r\in[r_{sur},r_{sur}+c\tau_L[\,. \tag{1-14}$$

For other ranges r, $P = 0$. r_{sur} is the distance along the probing beam between the satellite- or air-borne lidar and the Earth's surface; a is the surface albedo. Following equation (1-13), this expression is valid only if the lidar looks perpendicularly to the ground surface, or target. Specially from aircraft (nadir probing) or satellite, the surface echo helps to evaluate the atmospheric optical depth, particularly above areas with constant and known albedo (i.e., oceanic surface)

Instead of considering P as the detected electric power of the backscattered signal – power directly after the photocathode –, it is also possible to define it as the received optical power before the detector. In this case, the wavelength-dependent quantum efficiency of the detector, $\eta(\lambda)$, is removed from the lidar equation. From now on I will use this definition of P as optical power on the detector.

1.4. Ambient background and noise sources

The total measured signal contains the backscattered lidar signal resulting from the interaction of the laser beam with the atmosphere as only one of its components. It consists also of other contributions which are called noises, because they degrade the quality of the signal. Depending on the detection mode, analog or photon-counting, they are not always present. The most important of them (Saleh, 1991, Jelalian, 1992; Measures, 1984) are listed in Table 1.1

Noise type	Ph.-count.	Analog
Noise in signal (quantum, photon noise)	x	x
Background ambient noise	x	x
Photoelectron noise	x	x
Dark (current) noise	x	x
Gain noise		x
Thermal (Johnson) noise		x

Table 1.1. Type of noise encountered in lidar measurement depending on the detection mode .

---

[2] Also for the rest of this work, if not stated otherwise, all considered hard targets and surfaces are assumed to be lambertian.

The signal entering the detector (input signal) has an intrinsic photon (quantum) noise. The photoeffect converts the photons into photoelectrons. In the process, the mean signal decreases by a factor equal to the quantum efficiency of the detector. The noise decreases also but by a lesser amount than the signal. If a photodetector gain mechanism is present, it amplifies both the signal and the photoelectron noise, and introduces its own gain noise as well. Finally, circuit noise enters at the point of current collection. The background ambient noise is associated with light reaching the detector from extraneous sources, i.e. from sources other than the signal of interest. The dark-current noise is generated by the photodetection device even in the absence of light.

Careful evaluation of noises is of very high importance in remote sensing. It prevents from mis-interpretation, because they may appear as to be a signal while they are actually not real. In order to understand their source and their behaviour they are briefly discussed now.

1.4.1. Backscatter signal and shot (quantum) noise

Let $P_s(t)$ be the optical power of the backscatter signal impinging onto the detector (in [W]; cf. equation (1-7)). In case of photon counting detection, the number of photons $N_s(t,\tau)$ counted during the integration period τ is

$$N_s(t,\tau) = \xi_d \tau P_s(t) \quad \text{where} \quad \xi_d = \frac{\eta}{h\nu}. \tag{1-15}$$

The conversion factor ξ_d indicates the number of photoelectrons created per unit of optical energy for the considered detector. η is the detector quantum efficiency at the detected optical frequency ν, h the Plank constant. This equation is valid as long as the photon count rate $N_s(t,\tau)/\tau$ is smaller than the maximum linear count rate of the detector and its engendered photoelectrons.

In analog detection, the related current $i_s(t)$ (in [A]) at the detector output is

$$i_s(t) = \rho_d G_d P_s(t) \quad \text{where} \quad \rho_d = \frac{\eta e}{h\nu}. \tag{1-16}$$

ρ_d is the responsivity of the photodetector (in [A/W]), G_d denotes its gain[3] and e is the electron charge.

The photon flux associated with the optical power impinging onto the detector $P_s(t)$ is inherently uncertain due to the quantum nature of this signal. Thus a noise is generated. This noise is called *quantum* or *photon noise* because it is induced by the signal only when the signal exists. It obeys the Poisson probability distribution, under assumption that photon arrivals are statistically independent. A photon incident on the photodetector either generates

---

[3] Typical gain values for photomultiplier tubes are 10^5-10^6 and 30-100 for avalanche photodiodes.

a photoelectron[4] with probability η or fails to do so with probability 1-η . The *photoelectron noise* refers to the resulting fluctuations.

The quantum noise is given by the root-mean-square fluctuation of the received signal $\sigma(N_s)$ and it is equal to,

$$\sigma^2(N_s) = N_s\,. \tag{1-17a}$$

In analog mode, the photon stream incident on the detector results in a stream of electrical pulses which add together to constitute the electric current $i_s(t)$. The fluctuations associated with this current and attributable to the random way in which electrons are emitted or generated in the detector form a noise named *shot noise*.

Using equations (1-15) and (1-17a)[5], the current fluctuation is

$$\sigma^2(i_s) = 2eBG_d\,\mu i_s\,. \tag{1-17b}$$

B has been introduced as the photodetection *electrical bandwidth* and defined as $B=1/(2\tau)$. μ is added as an *excess noise coefficient* (also called *excess noise factor*). It accounts for the *gain noise* contributions during the amplification process.

1.4.2. Background radiation and background noise

The ambient background light is due to natural and artificial sources: sun, moon, lamps, etc. It consists in fact of any undesired optical radiation on the receiver. The power $b(t)$ of the received background radiation (arising from natural sources) is given as

$$b(t) = K_r S_b(\lambda)\Delta\lambda\Omega_r A \tag{1-18}$$

where K_r is a constant expressing the optical efficiency of the receiver, $S_b(\lambda)$ the spectral radiance from the sky at the instrument location and instant *t* (in [Wm^{-2}sr^{-1}µm^{-1}]), $\Delta\lambda$ the optical bandwidth of the receiver (in [µm]), Ω_r the receiver field of view (in [sr]) and *A* the effective aperture area of the receiver (in [m^2]).

---

[4] We should rather speak of "photoevent" to include both generation of photoelectrons in the case of PMT and photoelectron-hole pair in the case of APD.

[5] If *s* is a variable that follows Poisson statistic, then $E\left[\left(k(s-\bar{s})\right)^2\right] = k^2\bar{s} = k(k\bar{s})$. N_s is such a variable. Here we have $i_s=N_s e G_d/\tau$. More precise and exact derivation of this formulae may be found in (Yariv, 1991; Saleh, 1991).

In a similar way as for the backscatter signal but this time for the background radiation, the number of photons $N_b(t,\tau)$ detected during the integration period τ and the current i_b at the output of the photodetector are

$$N_b(t,\tau) = b(t)\xi_d \tau \quad \text{and} \quad i_b(t) = b(t)\rho_d G_d \,. \tag{1-19}$$

In comparison to P_s, P_b varies much less as function of the time. Among all parameters it depends on, $S_b(\lambda)$ is the one which fluctuates the most. While the duration of the atmospheric response to a single laser pulse is typically of the order of the millisecond, the sky radiance change rate will rather be of the order of the second or more. For this reason the background radiation is considered as constant during the acquisition of a single profile and its time-dependency may be neglected; it contributes as a constant offset to the total measured signal. In this sense it is of less importance.

Much more important are the fluctuations caused by the background radiation, that is the quantum or shot noise of the background radiation component. As it is an optical signal, it causes also fluctuations in the same way as the backscatter signal. These fluctuations are given in photon-counting, respectively analog, detection mode by

$$\sigma^2(N_b) = N_b \quad \text{and} \quad \sigma^2(i_b) = 2eBG_d \mu i_b \,. \tag{1-20}$$

What is usually called background noise is not the background radiation itself but the fluctuations that it induces.

1.4.3. Dark current and dark noise

The dark current is the leakage current produced by the photodetector when no radiation is incident upon the surface. It is mostly generated by thermal release of electrons from the semiconductor constituents of the photodetector and is consequently strongly dependent on the their temperature. This current, at the output of the photodetector and further referred to as i_d , is also associated to the term *dark counts* in photon-counting detection mode because it consists of small pulses that are distinct from each other when sufficiently rare. The dark count level, *d*, is usually provided per time unit, i.e. dark counts per second.

Let $N_d(t,\tau)$ be the number of dark counts during the integration period τ .

$$N_d(t,\tau) = d\tau \tag{1-21}$$

As the dark current is of randomness nature, the variance of its fluctuations in photon-counting, respectively analog detection mode, are again given by

$$\sigma^2(N_d) = N_d \quad \text{and} \quad \sigma^2(i_d) = 2eBG_d \mu i_d \,. \tag{1-22}$$

Here again, the dark current itself is of few importance because its change rate is much smaller than the duration of a profile and may be considered as constant, acting like an offset. Its fluctuations are of meaning; they are further simply called *dark noise*.

1.4.4. Thermal noise

The *thermal* or *Johnson noise* is associated with the thermal agitation of the current carriers in the load resistance R_{ld} (more precisely equivalent resistance depending on the pre-amplifier configuration) at the output circuit of the photodetector. It exists therefore only in the analog detection mode. The mean value of this thermal current i_{th} is 0 but not its fluctuations – actually referred to by the term thermal noise – which variance is given by (Yariv, 1991).

$$\sigma^2(i_{th}) = \frac{4kT_{ld}B}{R_{ld}}, \tag{1-23}$$

where k is the Boltzmann constant, T_{ld} the absolute temperature of the resistance, and B, as previously mentioned, the photodetection electrical bandwidth.

1.5. Lidar instruments used in the thesis

The equations in Sections 1.2 and 1.3 provide general considerations for the wavelength selection of the backscatter lidar. The laser wavelength shall not coincide with any absorption line of the atmospheric constituencies, so in the transmission term (Eq. 1-3) it is presented only the extinction due to the scattering. The wavelength shall be such that the contributions of the aerosol backscatter and the molecular backscatter in the lidar signal shall be comparable. i.e., where the signal is determined predominantly by the molecular backscatter (as in the free troposphere or in the UTLS without aerosol layers and thin clouds) the lidar signal shall be well above the noise level, so it may be used for calibration of the lidar signal part backscattered by the aerosol-rich altitudes.

From practical point of view, the most convenient laser source for pulsed backscatter lidar is the Nd:YAG laser. This laser has fundamental wavelength of 1064 nm, its second harmonic is at 532 nm and the third harmonic is at 355 nm. The lidar wavelength shall allow the use of sensitive and low noise detectors. The best candidate is the photomultiplier tubes (PMTs), with high quantum efficiency (sensitivity) for wavelengths 532 nm and 355 nm. The widespread Si-APD has only a few percent quantum efficiency at 1064 nm. The detection of this wavelength requires a special type IR enhanced APD (with a sole supplier Perkin Elmer). This reduces further the selection of most appropriate wavelengths for backscatter lidar probing to the second and third harmonics of the Nd:YAG laser.

For the specific tasks in aerosol stratification probing presented in the thesis, only the second harmonic of the Nd: YAG laser (532nm) has been used.

The results presented in Chapters 2 and 3 were obtained by a ground-based backscatter lidar with detection in analog mode and installed in the laboratories of the Observatory of Neuchâtel. The lidar employed for measurement during the campaign in Basel (see Chapter 4) is a compact, automated backscatter lidar with detection in photon-counting mode. The last two lidars deployed for measurement during four field campaigns presented in Chapter 5 are two compact, automated airborne lidars with detection in photon-counting mode. For each instrument I give here an introductory description.

1.5.1. Ground-based lidar in Neuchâtel

For the measurements presented in this study, the backscatter lidar operated with the second harmonic (532 nm) of a Q-switched Nd-YAG laser. The lidar normally works also with beams at the fundamental wavelength at 1064 nm and the third harmonic at 355 nm. The received backscatter light at the wavelength of the second harmonic is separated from the the fundamental and third harmonics. The received light at 532 nm may be additionally separated in two orthogonal polarizations with respect to the polarization direction of the 532 nm beam. The emitted output pulse energy ranges between 30 and 45 mJ at a pulse repetition rate of 20 Hz. The receiver has a diameter of 25 cm. The altitude of the full overlap is about 400 m. Photomultipliers and digital oscilloscope are used for data acquisition in analog mode. Altitude and temporal resolutions of a single lidar profile are 6 m and 60 seconds, respectively. The temporal resolution $\Delta t = 60$ s comes from the selected acquisition system mode: for one profile $\Delta t = (1000 \text{ shots} \times 2 \text{ Hz}) + T$, where T is the transfer time of the accumulated signal, $T \approx 10$ s. It comes that $\Delta t \approx 60$ s is the time of measurement of a single profile determined by the capacity of the acquisition system. Part of the transmitted laser power is deviated to a power monitor and used to normalize the detected atmospheric backscatter signal. In Fig. 1.3 is depicted the functional diagram of the ground-based lidar.

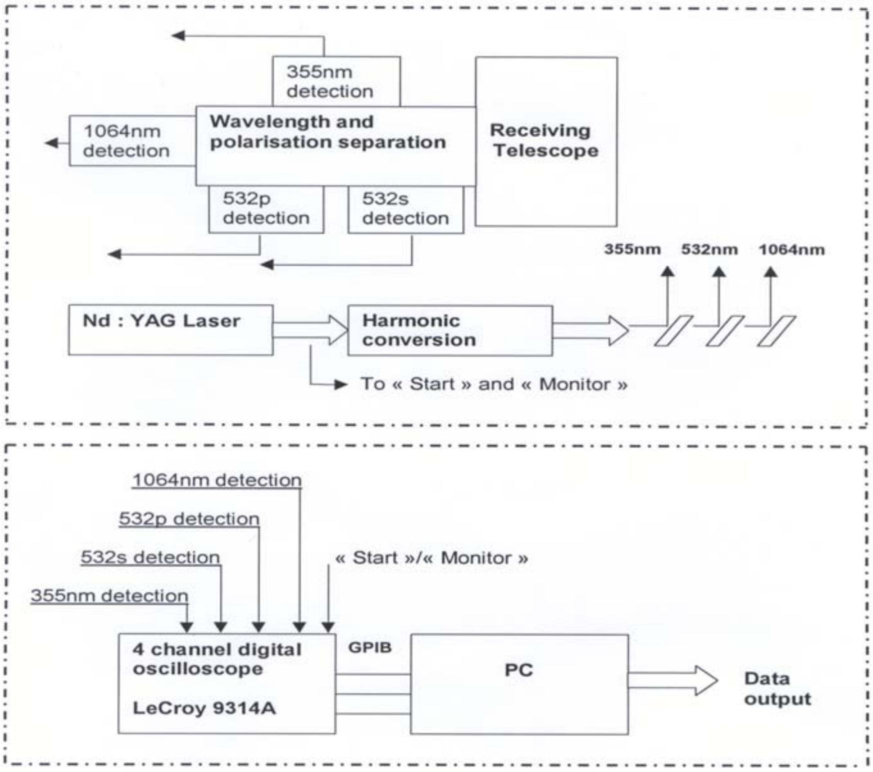

Fig. 1.3. Functional diagram of the Nd-YAG ground-based lidar. The upper panel shows the laser source and the emitting/receiving systems. The lower panel presents the data acquisition by oscilloscopes and CPU.

1.5.2. Lidar in Basel: project "BUBBLE"

"BUBBLE" (Basel Urban Boundary Layer Experiment) is the name of the project in which this lidar was operated for one year (see Chapter 4). The used lidar system, shown in the block diagram in Fig. 1.2 is a single-wavelength, backscatter depolarization lidar. The lidar makes use of a passively Q-switched micro-chip Nd:YAG laser with second harmonic conversion emitting at 532 nm. The laser beam is linearly polarized. The divergence of the transmitted beam is achieved by a beam-expander. A half-wave plate is used to fit the linear polarization of the transmitted beam in accordance to the polarization beam-splitter in the receiver chain. The data acquisition system is a photon-counting one. It is independent for the two polarizations (*p*, *s*). In this study only *p*-polarization signal is used. The data acquisition system has an adjustable range, best fitting to the distance between the successive laser pulses and the data storage capacity. The range used in BUBBLE lidar is adjustable, for the experiment in Basel it was fixed to 15 km.

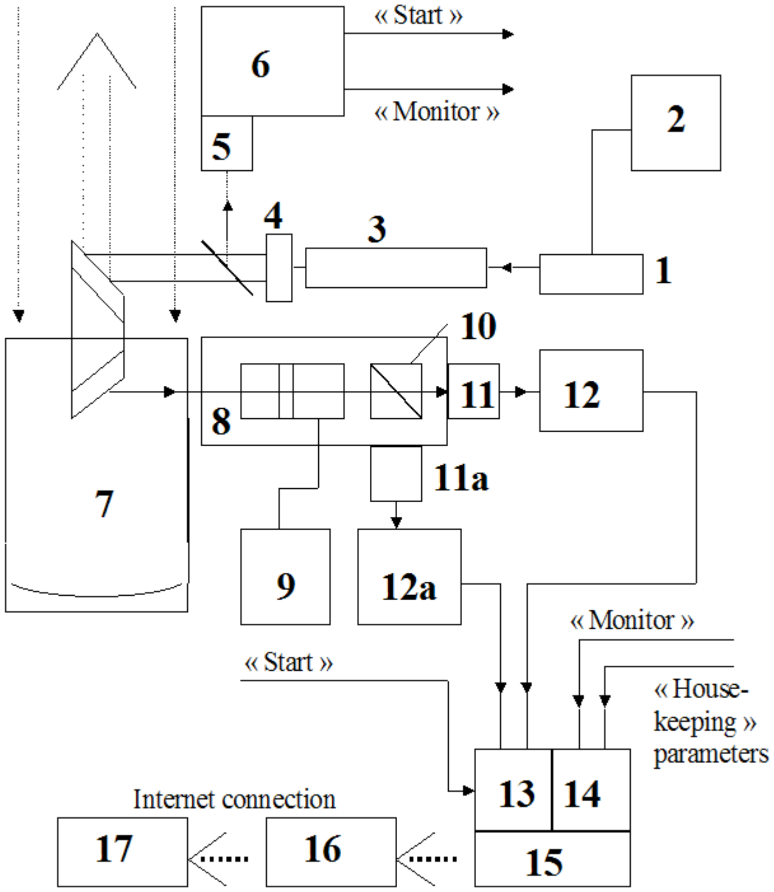

Fig. 1.2: Block-diagram of the lidar. (1) Laser optical head; (2) Laser power supply; (3) Beam expander; (4) Half-wave-plate; (5) Photodiodes for power monitoring and synchronization ("Start"); (6) Power monitor and "Start" electronic (7) Receiver telescope; (8) Narrow-band interference filter; (9) Thermo-stabilization electronics of the interference filter; (10) Polarization beam-splitter; (11) & (11a) Detectors (PMTs) for the p- and s- polarizations; (12) & (12a) Amplifier-discriminator chains; (13) Photon-counting data-acquisition system for two independent detectors; (14) House-keeping parameters recording system; (15) Micro-processor based control system; (16) Local PC; (17) Remote-control PC.

In Table 1.2 are presented the lidar sub-system and the technical performances.

Table 1.2. Performance of the subsystems of the lidar prototype.

Transmitter	
Laser type	Micro-joule (micro-chip)
Operational wavelength	532 nm
Average output power	18-20 mW
Polarization	Linear
Beam divergence	0.25 mrad full angle
Pulse duration	< 1 ns
Pulse repetition rate (prr)	5-6 kHz
Receiver	
Telescope type	Newtonian
Effective aperture	100 mm ∅
Field of view	0.5 mrad full angle
Range of full lidar overlap	180 m
Detection and data acquisition	
Type	Photon counting, two independent channels ('p' and 's' polarizations)
Detectors	Two PMT Hamamatsu
Raw signal range resolution	10 m
Detection range, Adjustable:	till approx 19 km @ 5-6 KHz prr; till approx 38 km with 2.5 KHz prr
Number of laser pulses for a single measurement	Adjustable, 100-2'000'000 pulses
Interface to the local PC for operational control	Serial RS232
Configuration (without PC)	
Lidar unit, Dimensions	740 x 560 x 560 mm
Lidar unit, Electrical power, voltage and consumption	230 V (optional 12 V, 28 V) consumption 0.3 A at 230 V

1.5.3. Miniature Aerosol Lidars (MAL1 and MAL2)

MALs (Miniature Aerosol Lidars) are two compact lidars installed since 1998/99 on the high-altitude research aircraft Myasishchev M55 'Geophysica' (Russia). One lidar is installed for probing in upward direction, while the other is installed for probing in downward direction. The lidars are single-wavelength, elastic backscatter-depolarization instruments. The performances of the lidar subsystems are presented in Table 1.3. The lidars use a high pulse-repetition rate diode-laser pumped Nd:YAG laser. The second harmonic of this laser (with a linear polarization) is used for lidar probing. The high-repetition rate combined with low pulse energy of the laser gives the possibility to use a photon-counting detection/acquisition system with high dynamic range. This makes possible to start the lidar profile as close to the aircraft, as allowed by the geometrical overlap function. The block diagram of MAL is shown in Fig. 1.3.

Table 1.3. Characteristics of the subsystems of lidars MAL

Transmitter	
Laser type	Nd-YAG micro-chip, passive Q-switched
Operational wavelength	532 nm
Average output power	16-18 mW
Polarization	linear
Beam divergence	0.25 mrad full angle
Laser pulse rep. rate	approx. 6 kHz
Receiver	
Telescope type	refractor
Effective aperture	50 mm ∅
Field of view	0.5 mrad full angle
Detection and data acquisition	
Type	Photon counting, two independent channels ('p' and 's' polarizations)
Detectors	PMT
Raw signal range resolution	MAL1: 21 m MAL2: 21 m
Dark noise	35 – 160 cps
PMT output pulses	TTL positive, 30 ns width
Count rate sensitivity	typ. 3 x 10^5 cps/pW
Number of range gates	1024
Single measure. duration	about 3 s
Configuration	
Unit and dimensions	single box, 510 x 320 x 170 mm^3
Unit mass	27 kg
Consumed current / voltage	max. 3 A / 28 VDC, incl. instrument heating
Operation control	continuous housekeeping parameter record

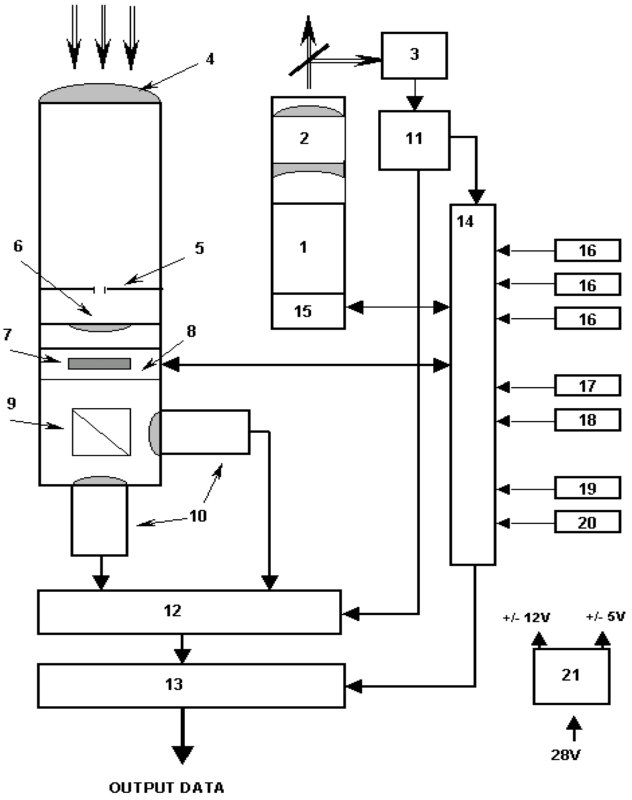

Fig. 1.3. Block diagram of MAL. Legend: micro-chip Nd:YAG laser with second harmonic conversion (1); beam expander (2); dual-element photodiode (3); receiver lens (4); diaphragm (5); collimating lens (6); interference filter (7); interference filter housing (8); polarisation beam-splitter (9); photomultiplier photon counting module with field lens (10); synchronisation and power monitoring electronics (11); acquisition electronics (12); embedded PC (13); housekeeping and safety loop electronics (14); laser temperature stabilisation (15); temperature sensors (16); sensor for pressure inside the pressurised box (17); pressure switch outside the pressurised box (18); input voltmeter (19); consumed current amperometer (20); DC-DC converters (21).

1.6. Methods for data evaluation

From calculations in Section 1.2, the power of the signal, $P(h)$, backscattered by an atmospheric layer of thickness (range gate) Δh centred at altitude h can be expressed also in the form (Weitkamp, 2005):

$$P(h) = P_L K O(h) \frac{A}{h^2} \Delta h \beta(h) T^2(h) + N \tag{1-24}$$

Where $T(h) = \exp\left\{ -\int_0^h \alpha\left(h'\right) dh' \right\}$.

Symbols and variables have the same connotation as in Eq. (1-8). P_L is the emitted optical power, K the overall optical efficiency of the instrument, A the telescope area, and $T^2(h)$ the round-trip transmission factor. The last term N is new with respect to Eq. (1-8) and takes into account the sum of the electronic and optical background noise. Only altitudes where the field of view (FOV) of the telescope completely overlaps the laser beam section are considered. For these altitudes, $O(h) \equiv 1$. The full overlap altitude value is different for each lidar and will be specified all the chapters.

In the signal processing, the range corrected signal (*RCS*) is computed as

$$RCS(h) = [P(h) - N] \cdot h^2 \tag{1-25}$$

In this thesis the *RCS* is averaged in altitude (binning) to decrease the shot noise component. Binning is different for the different studies presented in the next chapters. In particular, the number of bins used to average depends on what each study will focus on.

1.6.1. Gradient method

The gradient of the logarithm of the signal (Bösenberg and Linné, 2002), *GS*, allows to extract the extinction coefficient-at level *h* in linear form:

$$GS(h) = \frac{d}{dh}\log(RCS) = \frac{d}{dh}\log(\beta(h)) - 2\alpha(h). \tag{1-26}$$

The value of *GS* is around zero at altitudes where the aerosol backscatter is approximately constant. This condition is fulfilled where the aerosol is absent or very low (like in the FT), or where the aerosol content is homogeneously mixed (like in the ML). Gradient *GS* shows local peaks when passing from a layer with high aerosol to one with low aerosol content (negative peak) or vice versa (positive peak). For ground-based lidar measurements, the height corresponding to the minimum value of *GS*, h_{GSmin}, marks the height of the drop in the aerosol concentration and defines the BL top during the period of lidar observation. In all its various applications through this thesis, the single *GS* profiles are computed from Eq. (1-26) using single *RCS* profiles integrated over 60 s.

1.6.2. Variance method

The variance of *RCS* is defined as (Menut et al., 1999):

$$Var(h) = \frac{1}{N}\sum_{k=1}^{k=N}\left(RCS_k(h) - \overline{RCS(h)}\right)^2 . \tag{1-27}$$

The length of the *k*-index is equal to *N*, a parameter set to its optimum value depending on the specific study for which is used. The index *k* of summation represents the individual measurements $k = 1,\ldots, N$ in the *N*-interval. The mean value $\overline{RCS(h)}$ is obtained by averaging the single RCS_k profiles over *N*. The variance indicates how much the backscatter signal at a fixed *h* varies with respect to $\overline{RCS(h)}$ during the *N*-interval. as for the *GS* method, also for *Var* the RCS_i profiles are integrated over 60 s.

The lidar signal variance is very convenient in determining altitudes of enhanced aerosol mixing. Important example is the transition zone between the BL and the troposphere.

1.6.3. *Backscatter ratio of aerosol layers and thin clouds in the UTLS*

The UTLS is the atmospheric region where the MALs lidars carry out the measurements. In this region it is possible to consider the square Beer-Lambert transmission factor T^2 to be approximately 1. In the region of full overlap ($O(h) \equiv 1$), the lidar equation (1-24) may be expressed by the signal $S(h)$ after the corrections for the electronic and solar background noises and for laser power and range, appearing as:

$$S(h) = P_L K \frac{A}{h^2} \Delta h \beta(h) \tag{1-28}$$

In Chapter 5 is provided a description of the value of the parameters contained in Eq. (1-28) in the frame of the UTLS. Here, I introduce an important variable called *Backscatter ratio*, *BR*(*h*), which value linearly depends on the single molecular and aerosol backscatter coefficients:

$$BR(h) = \frac{(\beta_{mol}(h) + \beta_{aer}(h))}{\beta_{mol}(h)} \tag{1-29}$$

Combining the two equations (1-28) and (1-29) it is possible to retrieve the value of *BR*(*h*) for any air volume and for all *h*-altitude along the probed profile. For this it is also necessary to identify the atmospheric altitudes with presence of no (or negligible) aerosol.

Chapter 2

Aerosol stratification in the lower troposphere

This Chapter presents a validation of backscatter lidar methods to determine the aerosol stratification in the boundary-layer during both day and night. The validation is carried out using a traditionally accepted method based on the temperature stratification through the lower troposphere as measured by radiosondes. Correlation coefficients between lidar and radiosonde in both convective (day) and stable (night) conditions are between 0.88 and 0.97.

Motivations of the study

The MLD and the height of the residual layer (RL) top are two important parameters characterizing the aerosol stratification in the BL (Stull, 1988; Garratt, 1992; McIlveen, 1992). As the BL is the atmospheric region where almost all life processes take place, it is important to improve the knowledge about the depth of the diurnal (ML) and nocturnal (RL) layers developing within it. A thicker BL means a more diluted air and a lower concentration of pollutants; vice versa, when the BL is shallow and with no rain for several days the quality of the air decreases abruptly. That is why models describing the accumulation and transport of pollution shall take into account the MLD and the RL top height.

In 1930, meteorologists received a new efficient tool for measurement of the upper atmosphere state parameters, a radiosonde. In 1958, the first radiosondes were launched from Soviet weather ships. The technique of radiosounding of the atmosphere has found extremely wide applications. Radiosondes are regularly released from many aerological stations to bring the data on change in the vertical profiles of such important meteorological parameters as air temperature and humidity, atmospheric pressure and cloud cover. The well-known relation between the vertical gradients of the potential temperature and the height of the BL top was one reason for the temperature measurements by radiosoundings in the last 75 years. The information retrieved from this technique is precise, but limited to few soundings per day. The large infrastructures required to launch a sounding balloon from an aerological station limit also the possibility to realize several stations in the most interesting areas, i.e., the urban sites. Remote sensing instrumentations (radar, lidar, sodar, wind profiler etc…) can provide as well good information about the height of the BL top. When using a lidar in such measurement, the first question is how the lidar-determined aerosol stratification is relevant to the stratification of the temperature, which is presently accepted as one of the baseline methods (Siebert et al., 2001). Also, how the various lidar methods are consistent with each other. Up to now, it is not clear which is the real range of reliability of these remote sensing measurements with respect to the estimations retrieved by radiosonde techniques. In the previous studies the comparison between lidar and radiosonde methods to determine the MLD was mainly performed in convective conditions and on a few cases (Menut et al., 1999; Sicard et al., 2006; Wiegner et al, 2006). There is hardly any systematic comparison between radiosonde and lidar methods to determine RL height in stable nighttime BL. In this way, the motivation of this study is to determine the range of confidence between radiosonde and lidar measurements of the BL top during day and night. A good agreement between the two measurement would definitely confirm that a lidar can provide a reliable value of the depth of the BL and that it can do it in automatic and continuous way.

Background

Several studies focused on the dynamics of nighttime and daytime BL and aimed to forecast its temporal evolution (De Wekker et al. 1997; Rampanelli et al. 2004; Zampieri et al. 2005). The approximation of the current BL height (both day and night) is usually retrieved from the temperature inversion at the top of the BL as measured by radiosonde, or from the gradient in water vapour mixing ratio (Heffer et al. 1980; Stull 1988). One convenient and widely used method for the daytime determination of MLD by radiosonde measurements (Cramer 1972; Van Paul et al 1994; De Wekker et al. 1997) is based on the local maxima of the potential temperature vertical gradient.

The elastic backscatter lidar signal is determined by the altitude profile of the atmospheric aerosol. By using aerosol as a tracer for convective and mixing processes, the backscatter signal provides information on the BL stratification. As a remote sensing instrument, the lidar has advantages in detecting the MLD and RL height, in particular, in the possibility to perform continuous measurements and to choose the direction of probing.

Lidar signal gradient gives information about the structure of the BL, as it was demonstrated by Russel (1974). References to this method are in recent studies like Menut et al (1999); Bösenberg and Linné (2002); Frioud et al. (2003); Frioud et al. (2004); Matthias et al. (2004). Another method used for the MLD evaluation was developed by Hoopar and Eloranta (1986), and Piironen and Eloranta (1995), i.e., the standard deviation of backscatter signal. Menut et al. (1999) described this method referring to it as *centroid* method. In this reference, the altitude of the maximum of lidar signal variance over a period of 5 minutes was considered as an estimation of the MLD. The authors compared the MLD obtained with such procedure and the MLD determined from the *Richardson number*, where the latter was retrieved from radiosonde measurements. They considered four daytime convective cases and found good agreement between both methods. Other approaches directly using the backscatter lidar signal are given here as an overview of the state-of-the-art concerning the BL height determination. Melfi et al. (1985) evaluated the altitude where the backscatter signal drops below a defined threshold and assigned this value to the BL height. A technique to determine the altitude of this drop, based on wavelet technique, was suggested and used in a number of studies (Hayden et al. 1997, Steyn et al 1998; Steyn et al 1999; Hoff et al. 1997; Hägeli et al. 2000). This method has been further developed in (Cohn et al. 2000, Davis et al. 2000, Brooks 2003), with aim to obtain algorithms allowing automated data processing. The wavelet approach became very convenient also for lidar study of BL above complex terrain (Blumen, 1990), where the multiple layering of the aerosol is a typical situation in both daytime and nighttime.

The advantage of the lidar in such BL study is in the possibility to carry continuous measurement in the vertical cross section. Such continuous measurement reveals the dynamic of the BL development, what is not possible to achieve by other methods.

The objective of the present study is to compare two lidar methods with one based on the potential temperature gradient to determine the BL stratification during day and night. The two lidar methods are based respectively on lidar signal gradient and variance. The comparison includes 98 cases collected during two years between 2001 and 2003, 61 of which are at noon and 37 at midnight. All cases coincide in time with radiosounding from a nearby aerological station. The cases from data collection were selected for cloud-free (cumulus, stratus, altostratus) and fog-free conditions, however cirrus might be present. No other criteria of selection have been applied, like season or synoptic pressure conditions. All the nocturnal cases presented at least one elevated aerosol layer above the RL top. This is typical for the city of Neuchâtel, which has a complex topography that strongly contributes to the formation of several nocturnal aerosol layers.

2.1. Boundary layer dynamics and local circulation

Knowledge of the potential temperature lapse rate is usually sufficient to determine the static stability of an atmospheric layer and to identify its boundaries. An inversion corresponds to a sharp increase in local lapse rate of the potential temperature (θ) and respectively to an increase in the static stability (Stull, 1988) of the inversion layer. Starting from the ground level, the first maximum of $\partial\theta/\partial h$ (where h is the altitude) is considered as reference height for the actual BL top.

The lidar measurements were performed in Neuchâtel (47.000°N, 6.967°E, 485 m a.s.l.). The city (see Fig. 2.1a) is situated at the south slope foot of the Jura mountain range (oriented NE-SW with highest elevation at 1609 m a.s.l.), at the side of Lake of Neuchâtel (38.3 km long and 8 km wide, oriented in the mountain range direction). In such topographic conditions, it may be expected that the local circulation contributes to the BL development (Stull 1988; McIlveen 1992) during both day and night.

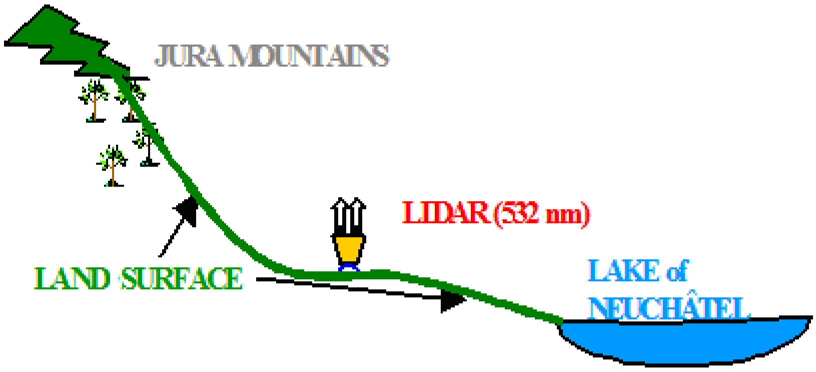

Fig. 2.1a. Local topography around the city of Neuchâtel (47.000°N, 6.967°E, 485 m a.s.l.).

During daytime, convection may drive anabatic wind (Blumen, 1990; McIlveen, 1992, 315-317) along the Jura slope. The anabatic wind normally enhances the mixing process inside the ML. In some cases, when the ML above Neuchâtel is shallow, the anabatic wind may flow over the ML. The outflow results then in an aerosol layer above the Neuchâtel ML. In addition, when the wind is from W and NW, aerosol layers are advected from the Jura top in the FT above the Neuchâtel ML. As these layers appear above the ML, so they do not affect the retrieval of the MLD from the lidar signal.

During nighttime, most part of the aerosol sediment in the stable NBL, but particles remaining from daytime ML are still present in the RL. The constituents can mix at the RL top with advected aerosol layers when they are lying immediately above the RL, diluting its aerosol content. One process of mixing inside the NBL and RL is due to surface winds. The lake and the mountain slope initiate breeze circulation and katabatic flow (Blumen, 1990; McIlveen, 1992, 315-317). The combined flows mix with the already established air masses and hence modify the NBL stratification (Wallace and Hobbs, 1977). The two local winds advect air from the Jura slope with aerosol content different from the one in the NBL. When the winds are strong the turbulent mixing may affect also the RL. Also the atmosphere above the RL is influenced by the local topography, like in daytime. The north-westerly wind blowing over Neuchâtel may advect aerosol layers coming from the Jura range and produce in the lidar signal profiles several peaks above the RL top. These peaks are referred further as nocturnal aerosol layers (NAL).

Fig 2.1b shows an outline of the diurnal and nocturnal layers that form within the BL (after Garratt, 1992). Layers developing inside the BL are indicated with the corresponding acronyms used in the text.

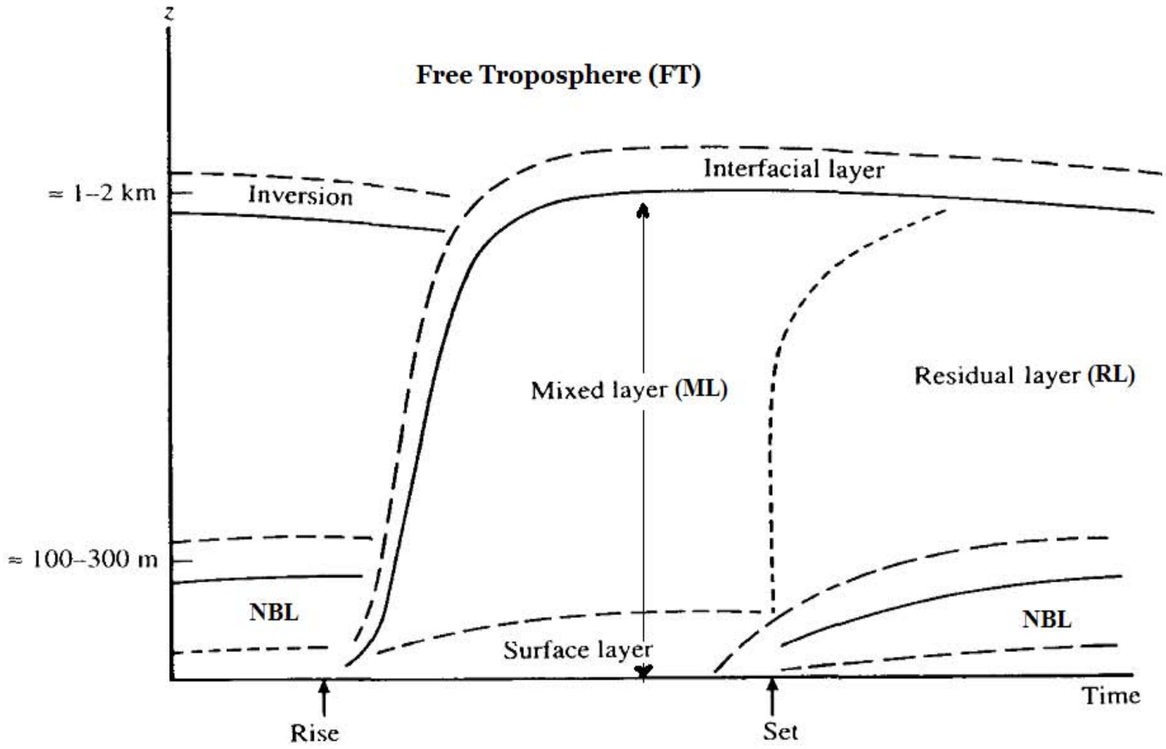

Fig. 2.1b A simplified presentation of the boundary-layer evolution (modified after Garratt, 1992). The altitude stratification of the aerosol is correlated with the dynamics of the layered BL structure. The vertical scale may give an initial idea for the necessary range and the range resolution of the backscatter lidar, operating for this type of measurements.

2.2. Lidar instrument and signal processing

Lidar measurements were performed from May 2000 till February 2003. During this period the lidar was deployed in the frame of the EC project EARLINET (Bösenberg et al. 2002; Bösenberg, Matthias 2003). The instrument used for this study is described in section 1.5.1.

The backscattered lidar power, $P(h)$, and the range corrected signal, *RCS* are expressed by Eqs. (1-24) and (1-25). The altitude of full overlap, i.e. the altitudes h for which $O(h) \equiv 1$ are $h > 400$ m a.g.l.

Before further processing to retrieve the MLD, RL and NAL heights, the *RCS* is averaged in altitude to decrease the shot noise component. The new altitude gates (bins) combine a given number of the original 6 m-bins. This number increases quadratically with the altitude; the vertical resolution Δh becomes 60 m at 1 km and 180 m at 4 km. The altitude averaging process leads to a decrease of the vertical resolution with the altitude, but the shot noise component is maintained almost constant.

2.2.1. Gradient method for long average profile

In Sect. 1.6.1 the gradient method was presented as a single *GS* profile directly computed from a single *RCS* profile. In this chapter the single gradient GS_i are computed as from Eq. (1-26), but over a time interval of one hour. The length of index i in Eq. (2-1) is then the length of the time interval over which the GS_i profiles are averaged to obtain the final *GS* profile:

$$GS_i(h) = \frac{d}{dh}\log\left(RCS_i\right) = \frac{d}{dh}\log\left(\beta_i(h)\right) - 2\alpha_i(h). \tag{2-1}$$

For noon and midnight, i goes from 1 to 60, corresponding to one-hour of measurement. Single GS_i profiles are computed by Eq. (2-1) using single RCS_i profiles integrated over 60 s and after altitude quadratic binning.

During daytime, in the ML, the level of the aerosol content remains almost constant with the altitude up to the height of the first temperature inversion that marks also the transition from the BL to the FT. Around this height, the aerosol concentration abruptly decreases and the backscattered signal drops accordingly showing a local minimum in GS_i value.

During nighttime, the first temperature inversion layer above the NBL (capping inversion) corresponds to the top of the RL (as it is shown in Fig. 2.1b). The fall speed of particles with diameter $d \leq 1$ μm is on the order of 0.03 cm s^{-1} and less (Salby, 1996). Aerosol particles with this diameter, and below this, remain suspended in the residual layer during the night. Since the lidar backscatter signal at the wavelength of 532 nm is more sensitive to particles with the smaller diameters, the RCS_i have quite homogeneous altitude distribution in the RL and a sharp decrease around its top. Corresponding to this altitude, GS_i profiles show local minima to be expected within the inversion layer, capping the RL.

The final *GS* profile, used for the comparison presented further, is obtained as arithmetic average of the GS_i profiles, measured during 60 minutes, starting 30 minutes before noon or midnight. Starting from the ground level, the height corresponding to the minimum value of *GS*, h_{GSmin}, marks the height of the drop in the aerosol concentration and defines the BL top during the period of lidar observation..

The use of d/dh{log[*RCS*(*h*)]} (Eq. (2-1)) for the determination of h_{GSmin} is advantageous compared to the use of simple gradient, d/dh[*RCS*(*h*)]. An advantage is to have the extinction coefficient in linear form, that allows to maxima and minima to appear with better expressed contrast. The two different types of derivative are compared in Fig. 2.2 The small value of the signal fluctuation allows to minimize the uncertainty in discriminating false signal gradients produced by the shot noise component from the ones produced by real atmospheric features.

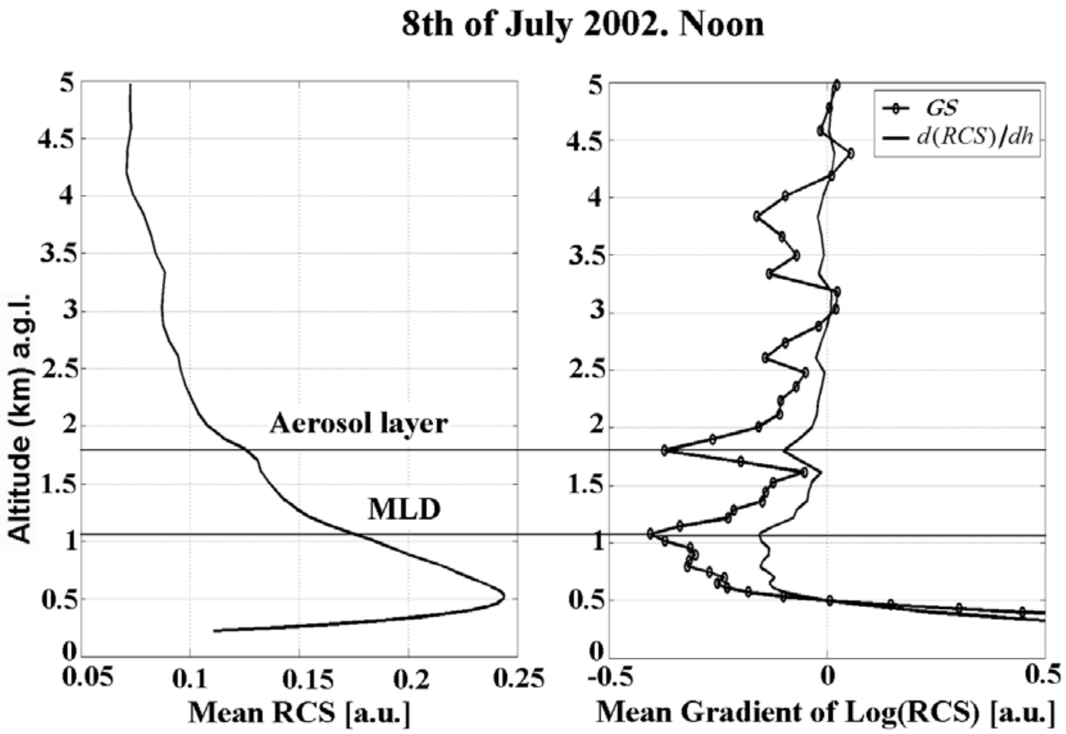

Fig. 2.2 Both panels show mean profiles, averaged over one hour around noon. The left panel depicts the mean *RCS*, the right panel the mean *GS* (heavy solid line) and the mean gradient of the signal (light solid line). Horizontal lines intersect the y-axis at the height of the MLD and the first aerosol layer above it.

2.2.2. Variance method for long average profile

As for the gradient method, also the variance has the same expression as in Chapter 1, in Eq. (1-27), but is now computed as a *sliding* variance over a time interval of one hour. The variance has then the form:

$$Var(h)_i = \frac{1}{N} \sum_{k=i+1-N/2}^{k=i+N/2} \left(RCS_k(h) - \overline{RCS(h)_i} \right)^2 . \qquad (2\text{-}2)$$

For a period of 60 minute, the external *i*-index goes from 5 to 55. The length of the *k*-index is equal to *N*, (see Fig. 2.3), here with value $N = 10$. The internal *k*-index of summation represents the individual measurements $k = i - 4 \ldots i + 5$ in the *N*-interval. The mean value $\overline{RCS(h)}_i$ is obtained by averaging the single RCS_k profiles over *N*. The variance indicates how much the backscatter signal at a fixed h varies with respect to $\overline{RCS(h)}_i$ during the N-interval. Eq. (2-2) applies to all i-profiles; passing from profile i to profile $i + 1$, the N-interval shifts by 1 minute and makes reference to $\overline{RCS(h)}_{i+1}$.

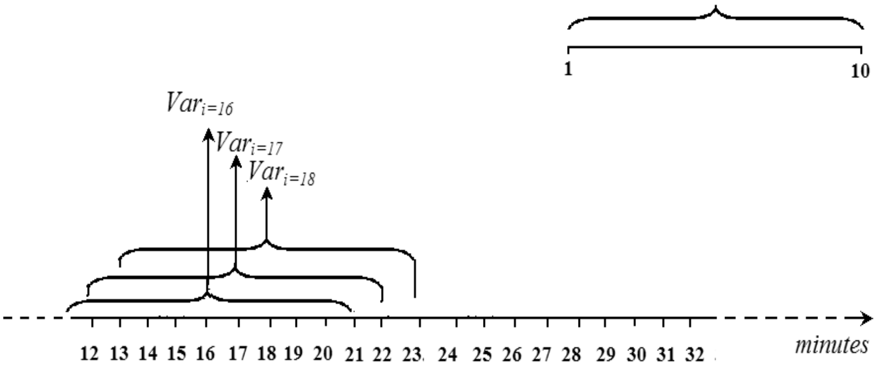

Fig. 2.3 The outline shows the single Var_i profiles computed by Eq. (2-2) using a moving average over the N-time interval where $N = 10$ minutes. The N-time interval shifts of 1 minute from profile i to profile $i + 1$.

In daytime convective conditions, ascending air parcels (updrafts) are thermals rising from the ground surface and developing through the ML. Descending air parcels (downdrafts) are produced by thermals break down at the top of ML entraining air from the FT. Fig. 2.4a illustrates the up- and downdraft dynamics around the top of the ML in a convective situation with a typical noon MLD at 1 km. When the convection is moderate, the *free convection scaling velocity*, w_*, i.e., a velocity scale for the convective boundary-layer, can be on the order of $w_* \approx 1.5$ to 3.5 m s^{-1}. The entrainment zone (EZ) thickness may amount to 300-400 m for a MLD of about 1 km (Flamant et al., 1997; Hägeli, 1998). Thermals entering and passing through the EZ will then require about 5 to 12 minutes (Stull, 1988, p. 463) to reach the ML top. In a mean zonal flow of few meters per second, there will be a diagonal shift of the ascending and descending air parcels. Passing through the FOV of the lidar telescope at different instants, they will cause variability in the backscattered signal. Applying these considerations to the variance method, I have determined the value of $N = 10$ in Eq. (2-2), i.e. a sub-interval duration of 10 minutes. In this way each single Var_i profile likely cover at least one up/downdraft event. In cloud-free condition the buoyancy flux at the surface fuels the thermals at an almost constant rate, keeping active the up- and downdraft process. It is then useful to use a *moving variance* to capture all up- and downdraft events during the period of measurement. Since the top of the ML corresponds to the level at which mixing of air parcels between ML and FT is most probable, the Var_i maxima are expected to match the ML top. Thermals may engender large signal variability not only as part of the up- and downdraft process, but also in producing gravitational distortion of the inversion layer with the similar time period as above. The final Var profile is obtained as arithmetic average of the single Var_i profiles.

In convective conditions, the zone where the aerosol concentration drops and the zone where the exchange with the FT takes place coincide. For this reason it can be expected that the altitudes of local minimum in *GS* and local maximum in *Var* will be inside this zone– see Fig. 2.4a.

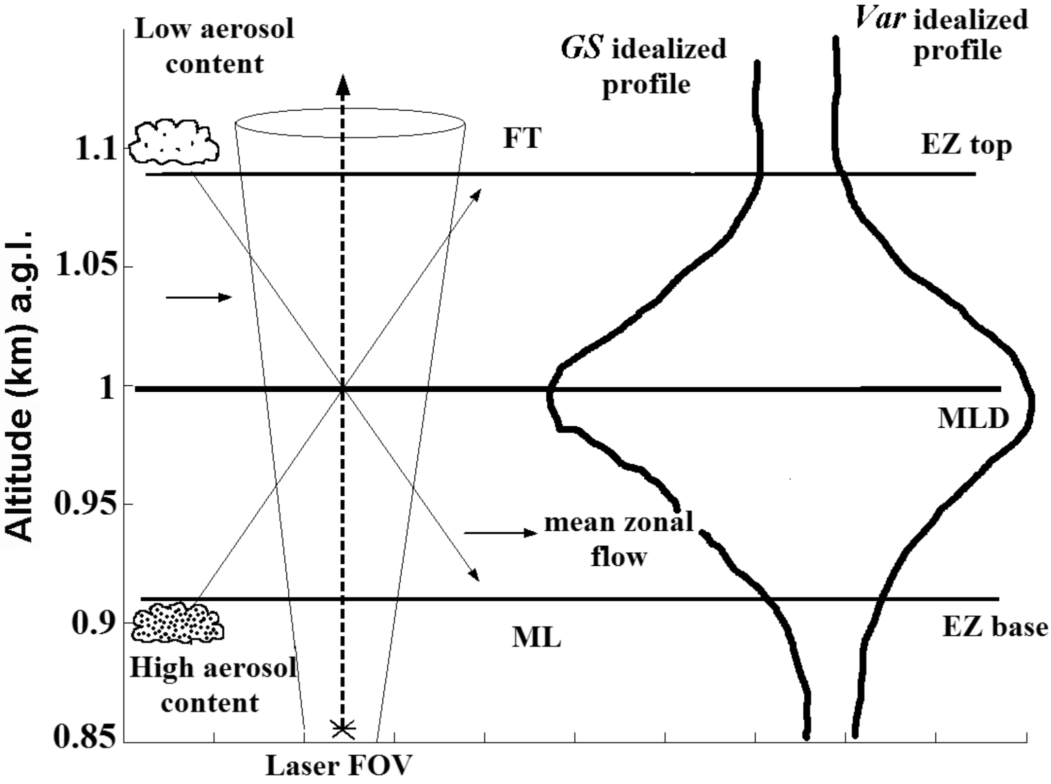

Fig. 2.4a. Simplified presentation of the up- and downdraft dynamics at MLD level. The dashed heavy line is the upward laser beam; empty and filled clouds on the left are the air parcels undergoing updrafts and downdrafts through the EZ, and slant light lines show the illuminated atmospheric (cone shaped) volume by the laser. Diagonal shifting is caused by the mean horizontal wind. Idealized *GS* and *Var* vertical profiles show minimum and maximum values, respectively, at MLD level.

During nighttime stable conditions, distortions of the inversion layer due to gravity waves may lead to backscatter signal variability at that altitude. At the level of the boundary between RL and FT the turbulent mixing due to wind shear also generates time-variation of lidar signal. When the wind shear is weak or absent, it exists nevertheless a mixing between RL and FT, in this case it is significantly lower than in daytime convective conditions and determines a smaller *Var* peak. Above the RL top, at the level of the first NAL, the wind profile may show a gradient at both NAL's boundaries. In such case, the turbulent mixing takes place at both boundaries producing a double maximum in *Var*. The vertical distance between the two maxima provides an evaluation of the thickness of the temperature inversion corresponding to NAL (see Fig. 2.4b).

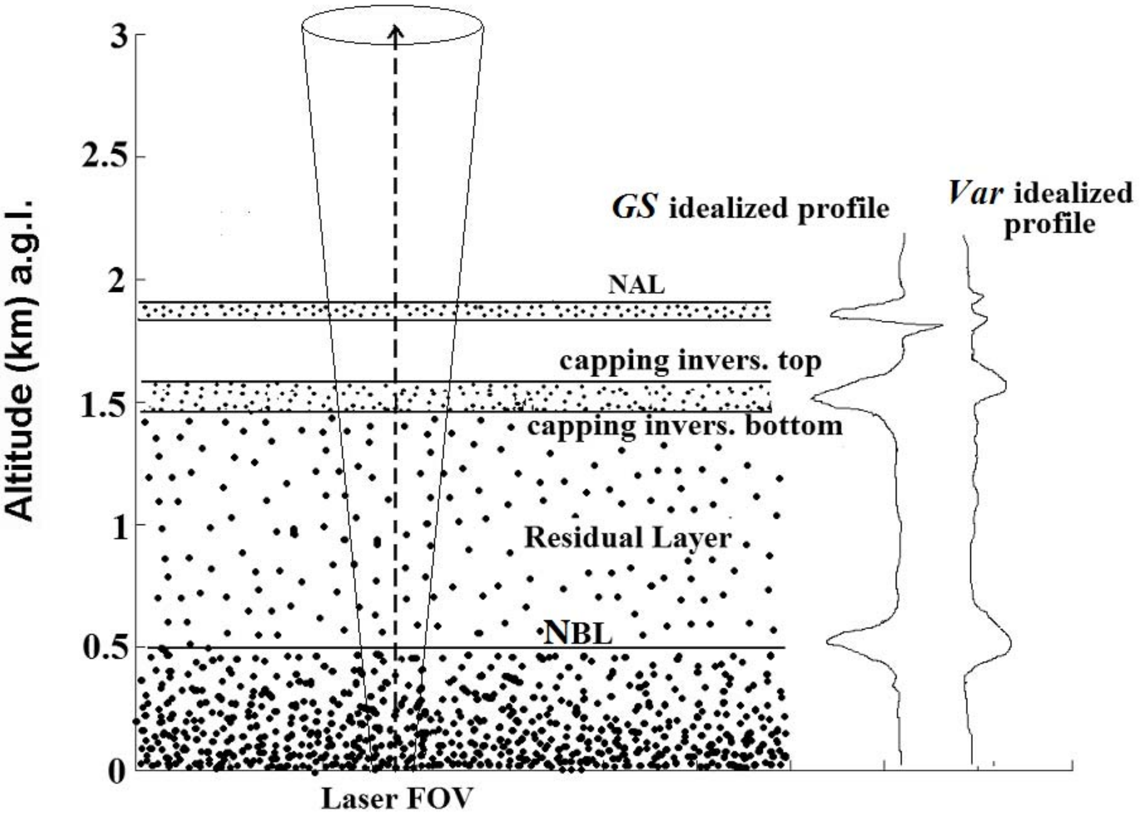

Fig. 2.4b. Outline of the aerosol stratification in the nocturnal lower troposphere (NBL, RL and NAL). Larger aerosols sediment to the bottom of the NBL. Only smaller aerosols stay at higher levels during the whole night as in the capping inversion at the RL top and at the level of NAL, above the RL. Slant light lines show the illuminated atmospheric (cone shaped) volume by the laser. The upward heavy dashed line shows the laser beam propagation direction. On the right side, the idealized *GS* and *Var* profiles are reproduced. Notice that *Var* has two local maxima: one at the top and one at the bottom of NAL.

Following Taylor's hypothesis, a measurement at one point in space over a long time period can be interpreted as an observation of a large region of space at an instant in time. This is possible when the *frozen turbulence* condition is accomplished ($\sigma_W < 0.5 \cdot W$, where W is the horizontal wind magnitude and σ_W the standard deviation of the wind speed). This condition is achieved for the already treated idealized case of constant zonal flow of few meters per seconds. The one-hour time averaged *Var* profile can then be thought as a space averaged one. The signal variance at the height of the temperature inversion will show a local maximum representing a measure of the current BL top height. Finally, , during daytime, the *Var* maximum at the level of the inversion layer is due to the combined action of the distorting plumes and the air parcel mixing. During nighttime, the principal *Var* maximum, is determined by both the gravity waves and wind shear.

2.2.3. Comparison algorithm

The automated procedure I developed, first determines the MLD, RL and NAL heights from the lidar data and, separately, the altitudes of temperature inversions from $\partial\theta/\partial h$. It then correlates the lidar to the radiosonde computed values. For lidar-derived heights, no assumptions about the aerosol stratification are needed.

The steps of the automatic lidar data processing start from:

i. the measured lidar raw signals with 60 s and 6 m temporal and altitude resolutions; the signals are corrected for the electronic noise, laser power variations, optical background and range (altitude). The initial vertical resolution in the corrected signal is decreased by the quadratic altitude binning between 0 and 8 km a.g.l. to reduce the fluctuations due to the signal shot noise component at farther ranges.

ii. Single GS_i profiles and the averaged *GS* are obtained as described in Section 2.1., Eq. (2-1), with final averaging time of 60 minutes. Single Var_i profiles and the averaged *Var* are obtained as described in Section 2.2.2, Eq. (2-2), with final averaging time of 60 minutes.

iii. The heights of the first (starting from the ground level) minimum and maximum of *GS* and *Var* profiles respectively, are detected by the algorithm and the mean value between the two heights is kept as reference height (h_{ref}) for the next steps.

iv. The θ profile and its gradient $\partial\theta/\partial h$ are computed from the radiosonde data.

v. A vertical window centered in h_{ref} and with extension equal to $0.15 \cdot h_{ref}$, limits the vertical region in which to search the principal maximum of $\partial\theta/\partial h$ (e.g., for $h_{ref} = 1$ km, the window extension is 150 m, from 0.925 km to 1.075 km).

vi. The three altitudes obtained from *GS*, *Var* and $\partial\theta/\partial h$ represent each an estimation of MLD, RL or NAL height.

2.3. Observations

Each case of the elaborated comparison database consists in a lidar measurement over 60 min around noon and midnight, i.e., from 1130 to 1230 and from 2330 to 0030 UTC, respectively. Each measurement comprises 60 single profiles of 1-minute integration time each. Radiosoundings were performed at the MeteoSuisse aerological station in Payerne, approximately 20 km South of Neuchâtel. Radiosonde data contain wind, pressure, temperature, relative humidity, and dew point.

The potential temperature θ is retrieved from temperature and pressure as measured by radiosoundings using *Poisson's equation* (Stull, 1988):

$$\theta = T_1 \left(\frac{1000}{p_1} \right)^{0.286} \tag{2-3}$$

where T_1 is the initial temperature in degrees K and p_1 is the initial pressure in hPa. The numerator of the fraction is the surface pressure, also expressed in hPa. Potential temperature θ and its vertical gradient $\partial\theta/\partial h$ provide the heights of the temperature inversions. These altitudes are then correlated with the MLD, RL and NAL heights as obtained from *GS* and *Var* methods. Vertical resolution of θ is not constant and depends on the vertical velocity of the sounding balloon; however, θ vertical resolution is always higher than that of *Var* and *GS* in the studied range of altitudes, from 0 to 5 km a.g.l..

2.3.1. Noon and midnight lower troposphere: two examples

The cases shown in Figs. 2.5 and 2.6 are measurements taken respectively on 20 May 2002, noon, and 13 August 2001, midnight. They are presented as examples to illustrate the considerations given in Section 3.c for the comparison algorithm.

The height of the inversion layer as detected by $\partial\theta/\partial h$ and the MLD retrieved from the two lidar methods are depicted in Fig. 2.5. The center of the average time interval for mean *GS* and *Var* profiles corresponds to noon, when the radiosonde measurement is carried out. The black horizontal line intersects the *y*-axis at the MLD level (i.e., 1.215 km a.g.l.) computed by the *GS* method (MLD computed by *Var* method is slightly lower, at 1.146 km a.g.l.). Black circles highlight the temperature inversions and the corresponding positive peak in $\partial\theta/\partial h$. The height computed by *GS* appears in the plot at about 100 m above the top of the temperature inversion layer and about 200 m above the local maximum of $\partial\theta/\partial h$, corresponding to the centre of the inversion layer. The aerosol-rich air mass is confined below the first temperature inversion. Therefore, the main decrease in signal amplitude appears immediately above the inversion level. Consequently, the computed *GS* minimum is just above the top of the inversion layer. The *Var* maximum height is principally determined by its *mixing* component; it is not influenced by the contribution from the gravitational distortion of the inversion layer. Since I work with the mean *Var* profile, the altitude fluctuations of the inversion layer during the time of measurement do not affect its mean position, but make it more spread. Thus, the *Var* maximum corresponds to the level where most of the exchange process takes place, namely at or immediately below the inversion layer top.

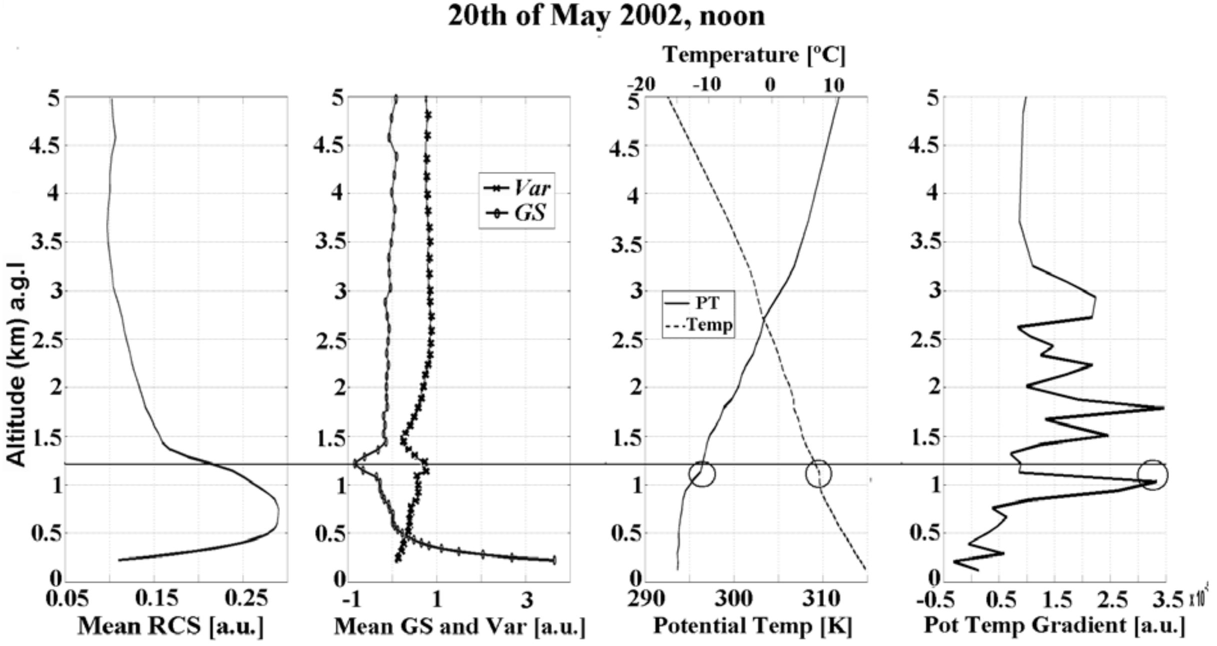

Fig. 2.5. The four panels show, from left to right, the vertical profiles of mean *RCS*, mean *GS* and *Var*, temperature and θ, and $\partial\theta/\partial h$. Mean *GS* and *Var* vertical profiles are averaged over 1 hour. Altitude is in km a.g.l.; Payerne is at 491 m a.s.l. and Neuchâtel at 485 m a.s.l., *y*-axis are shifted for the 6 meters difference. The black horizontal line intersects the *y*-axis at the MLD level computed by the *GS* method. Circles show the temperature inversions and the corresponding positive peak in $\partial\theta/\partial h$.

A summer midnight case, 13 August 2001, is presented in Fig. 2.6. The gradient $\partial\theta/\partial h$ in the fourth panel shows several local maxima, indicating a complex nocturnal BL. Despite this multilayer structure, the heights of *GS* minima coincide with those of $\partial\theta/\partial h$ maxima. Horizontal lines in the figure show the heights of NBL top, RL and NAL as computed by *GS*. The presence of nocturnal multiple aerosol layers above the RL represents a difficulty when retrieving the RL top height, in particular when these layers are close to it. The first maximum of $\partial\theta/\partial h$ at about 200 m matches the centre of the superadiabatic layer, i.e. the NBL. Above this level the first horizontal line intersects the *y*-axis at 537 m a.g.l., at the level of the NBL top. As expected (Stull, 1988, p. 17), the top of the NBL does not correspond to any temperature inversion; nevertheless, it is indicated by the decrease in the backscatter signal and respectively by the negative peak in *GS*. Above the NBL, at the RL top, the dashed horizontal line passes through the *GS* minimum appearing slightly above the corresponding $\partial\theta/\partial h$ maximum. The two solid horizontal lines above the RL intersect the *y*-axis at 1.215 km and 1.707 km showing the levels of two elevated NALs. In both cases the lines match the corresponding $\partial\theta/\partial h$ maxima. The *Var* profile shows, at the levels of NBL, RL and first NAL, similar structures: one more pronounced maximum at lower altitude, below the *GS* minimum and another, less pronounced peak at higher altitude, above or at the level of the *GS* minimum. From the radiosonde data the vertical profile of wind direction was inspected, and found a shear at the altitudes corresponding to the RL top and the first NAL. The turbulent mixing at these levels due to wind shear, determines the two *Var* peaks. Gradient *GS* has a minimum inside the inversion layer matching the level of the maximum decrease of aerosol backscatter. The maxima of $\partial\theta/\partial h$ are found approximately at or a little below the level of the *GS* minimum and definitely below the higher *Var* maximum (as illustrated in Fig. 2.4b).

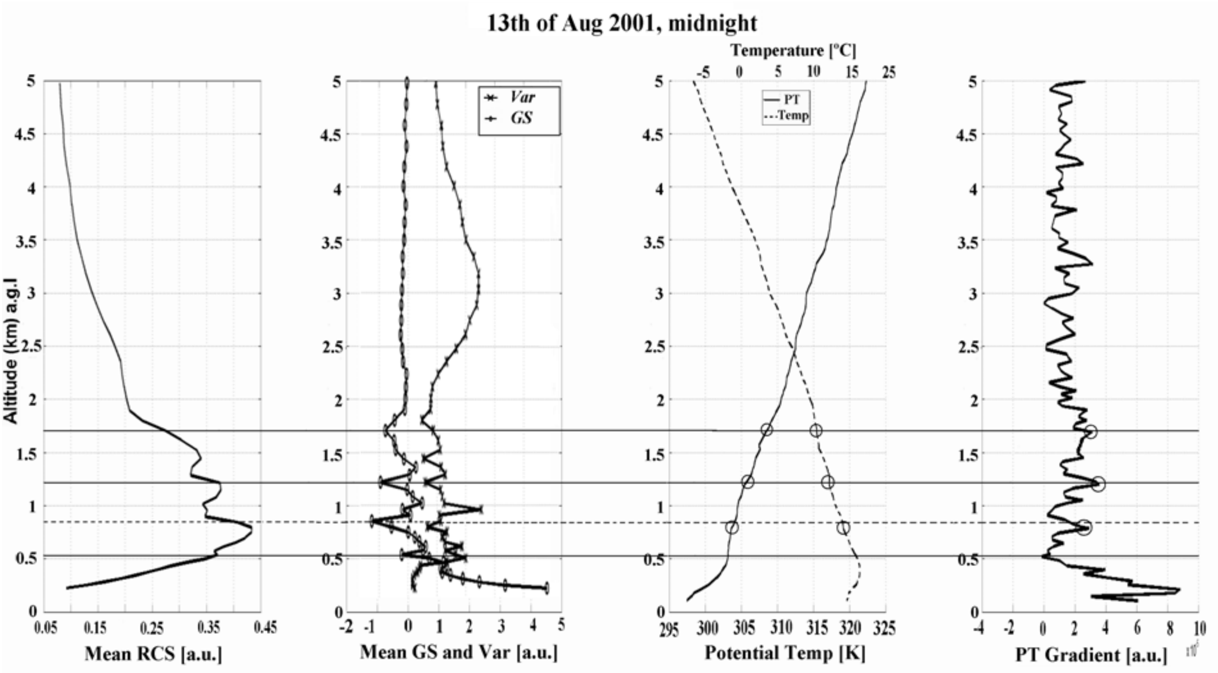

Fig. 2.6. From left to right the panels show mean *RCS*, mean *GS* and *Var*, temperature and θ, and $\partial\theta/\partial h$. The first (from ground level) black horizontal line intersects the *y*-axis at the NBL top level. The dashed line intersects the RL top level. The other two solid lines intersect with the *y*-axis at the level of the NALs above the RL top. All the lines pass through the heights computed by the *GS* method.

2.3.2. *Uncertainty estimation*

The combined temporal and altitude averaging reduces the shot noise level. As example, the shot noise component σ_{shot} at 2 km, for a single *RCS* profile without altitude binning, is 4% of the *RCS* value. Averaging reduces the shot noise contribution by a factor $E = \left(N_p \cdot N_b\right)^{0.5}$, where N_p and N_b are, respectively, the number of profiles and the number of bins used for averaging. Hence, the shot noise after the average process is $\sigma_{\text{Av}} = \sigma_{\text{shot}} \times E^{-1}$.

Typically, $N_p = 60$ and $N_b = 17$ at 2 km, so E equals about 32. It shall be noticed that the resulting temporal and vertical resolutions after averaging are comparable with those applied in previous lidar studies of MLD (Matthias et al., 2004). In the present analysis, σ_{Av} is reduced to negligible values compared to the uncertainty contributions described below.

Possible uncertainty sources affecting lidar and radiosonde comparisons could be the geographic distance between Neuchâtel and Payerne, the difference in the time duration of the two measurements (one-hour average for the lidar and several minutes for the radiosonde ascent) and the bias induced by using two different methods, *GS* and *Var*.

The area of Payerne is expected to be affected by similar local circulation as the area of Neuchâtel. The aerological station is 20 km south of Neuchâtel on the opposite lake shore. During night, the lake presence modifies the NBL by engendering breeze circulation in both Neuchâtel and Payerne. When the wind blows from NW, elevated aerosol layer are advected from the Jura mountains towards Neuchâtel. In a mean northwesterly flow of 10 m s^{-1}, this aerosol layer may be advected from Neuchâtel to Payerne in about 30 minutes. Following these considerations, I assume that the geographic distance between the two sites does not introduce major uncertainties in this study.

While lidar computed altitudes result from an average over one-hour, radiosoundings are spot measurements of only few minutes of duration carried out during the central part of the lidar observation. An estimation of the induced uncertainty is given by the altitude variations of the minimum, respectively, the maximum of single GS_i and Var_i profiles during the one-hour measurement. Some representative cases have been taken from the database to compute the vertical differences between the highest and the lowest peaks of GS_i and Var_i obtained during the one-hour interval. For each method (*GS* or *Var*) and for each type of measurement (noon or midnight) a mean value of these differences represents an estimation of the uncertainty. For midnight and noon (subscripts *m* and *n*) it is indicated by the symbol $\xi_{m,n}$. As $\xi_{m,n}$ are computed for each lidar method, I have a total of four uncertainties: $\xi_{m,n,GS,Var}$. The four obtained ξ-values are: $\xi_{n,GS} \approx 340$ m; $\xi_{n,Var} \approx 240$ m; $\xi_{m,GS} \approx 110$ m; $\xi_{m,Var} \approx 90$ m.

There is *a priori* no reason for either one of the two methods to be closer to the "true" value than the other (here the "true" value is determined by $\partial\theta/\partial h$). In Fig. 2.7 and Fig. 2.8, histograms show frequencies of the differences between the altitudes retrieved from *GS* and *Var* in noon and midnight cases, respectively. I assume that the differences MLD_{GS}-MLD_{Var} and RL_{GS}-RL_{Var} distribute according to the standard normal density function. The Gaussian $F_{x,\mu,\sigma}$ is superimposed to the histograms, where the *x*-values are the differences MLD_{GS}-MLD_{Var} and RL_{GS}-RL_{Var}, μ and σ are respectively the mean value and the standard deviation of the *x*-values. The standard deviation represents the uncertainty in evaluating the MLD and the RL height using *GS* or *Var* methods.

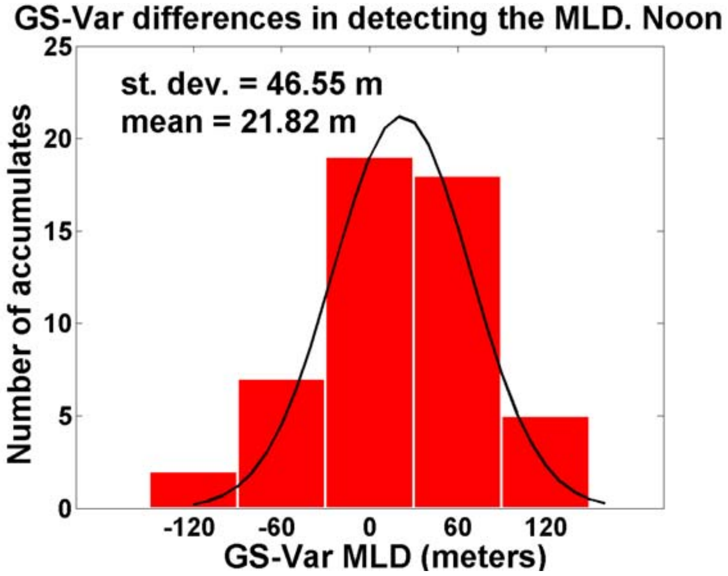

Fig. 2.7. Histogram of MLD_{GS}-MLD_{Var} noon values. *x*-axis resolution is 60 meters equal to the *GS* and *Var* vertical resolution at 1 km.

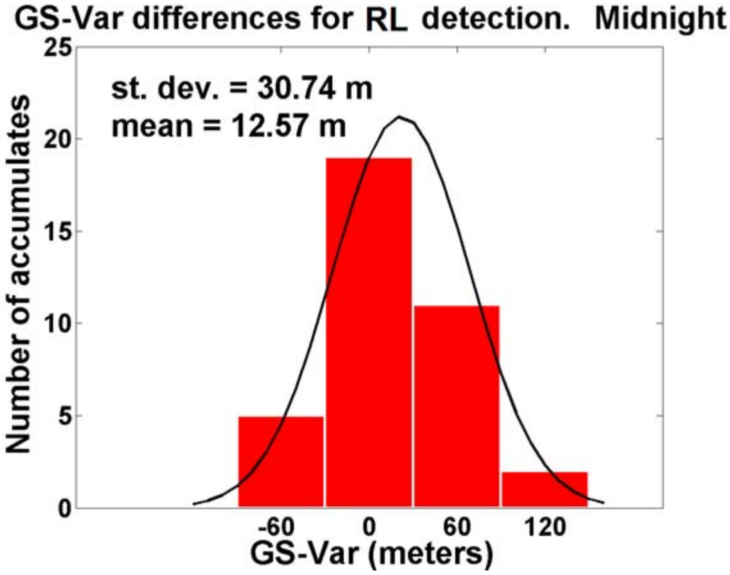

Fig. 2.8. Histogram of RL_{GS}-RL_{Var} midnight values. *x*-axis resolution is 60 meters equal to the *GS* and *Var* vertical resolution at 1 km.

The approximated normal distributions show a mean positive shift for both noon and midnight cases. For noon cases, the mean value μ is 22 m and the standard deviation σ is 47 m, for midnight cases μ is 13 m and σ is 31 m. The results show that "zero" is the most frequently obtained value, for both noon and midnight cases, hence, "zero" is the statistic *mode* of the distributions. The positive values of μ lead to conclusion that the heights computed by *GS* method are statistically higher than the heights computed by *Var* method.

The resulting bias is $b_{m,n} = \mu \pm \sigma$ where the subscripts m and n have the same meaning as for $\xi_{m,n}$.

The total uncertainty is then:

$$U_{tot} = b_{m,n} \pm \xi_{m,n,GS,Var} / 2 \qquad (2\text{-}4)$$

The values of ξ are used in the correlation plots (Figs. 2.9a to 2.10b) to express the amplitude of the error bars $\pm \xi_{m,n,GS,Var}/2$.

2.3.3. Correlation between lidar methods and potential temperature

Correlations are shown in Figs 9a-11b. All data distributions are linearly fitted without forcing the line to pass through the axis origin. The line equations in the plots have the form $y = ax + b$. Correlation coefficients have to be interpreted in respect to the offset "b" and slope "a". Both parameters are due to the combined presence of bias $b_{m,n}$ and statistical under- and overestimate introduced by the use of *GS* and *Var*. As overestimate I understand that the height computed by *GS* or *Var* is higher than the one retrieved from $\partial\theta/\partial h$, and vice versa for underestimate. Investigation of x and y values for which *GS* or *Var* overestimate $\partial\theta/\partial h$ is done by studying the relation $y/x > 1$.

2.3.3.1 GS and θ

The correlation between MLD_{GS} and MLD_{θ} for noon cases is illustrated in Fig. 9a. Measurements from the data collection are representative for different seasons as well as for various atmospheric conditions in terms of temperature, humidity, wind and pressure. Nevertheless, the data points in Fig. 9a are distributed closely around the linear fit with a correlation coefficient $R^2 = 0.96$ (error bars are $\pm \xi_{n,GS}/2$). This demonstrates that convective MLD obtained from lidar and radiosonde methods are statistically well correlated, independently from the difference in synoptic conditions. Data between 0.5 and 1.5 km distribute fairly homogeneously and represent the 75% of the cases. Relatively to $\partial\theta/\partial h$, *GS* provides statistical overestimate of the MLD for altitudes up to 1.8 km (linear fit: $y = 0.98x + 0.03$).

Correlation between RL_{GS} and RL_{θ} for midnight cases is shown in Fig. 9b. The two thirds of data distribute between 0.4 km and 1 km. Correlation coefficient R^2 is equal to 0.90, the offset is 73 m and the slope is 0.92 with error bars $\pm \xi_{m,GS}/2$. From these parameters it comes that *GS* underestimates the height of the RL top for ranges above 0.96 km. Examining the distribution in the plot, it emerges that the data are split at about 40% above and 60% below this range.

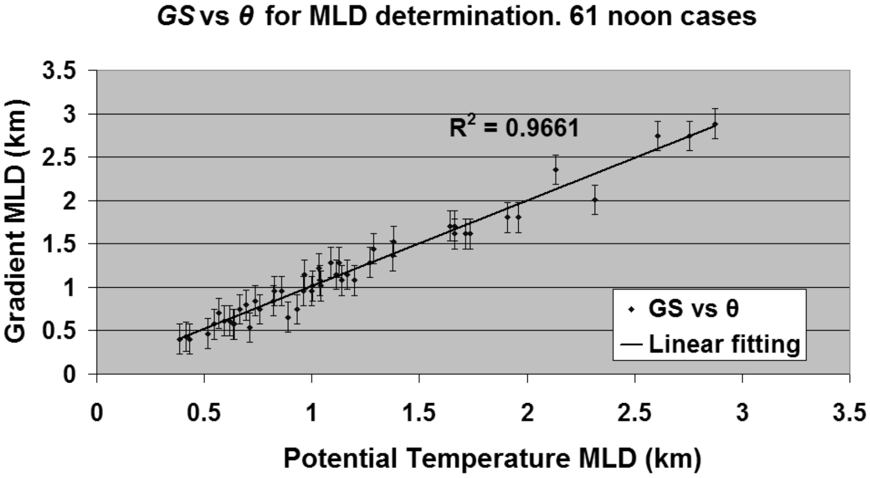

Fig. 2.9a. Correlation between MLD computed by *GS* and $\partial\theta/\partial h$ for 61 noon cases. Error bars amplitude $\xi_{n,GS}$ on y-values is equal to 340 m, correlation coefficient is 0.96. The slope and the offset of the fit line are 0.98 and 0.028 km, respectively.

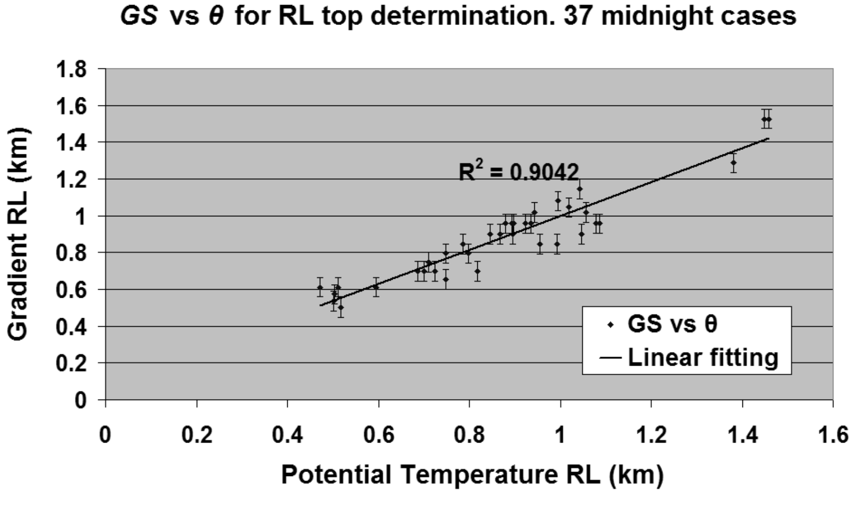

Fig. 2.9b. Correlation between RL computed by *GS* and $\partial\theta/\partial h$ for 37 midnight cases. Error bars amplitude $\xi_{m,GS}$ on y-values is equal to 110 m, correlation coefficient is 0.92. The slope and the offset of the fit line are 0.944 and 0.063 km, respectively.

2.3.3.2 *Var and θ*

Figures 2.10a and 2.10b present the correlation between *Var* and $\partial\theta/\partial h$, respectively for noon and midnight cases. Error bars have the same meaning as in Figs. 2.9a and 2.9b, but with the different values $\pm\,\xi_{n,Var}/2$ in Fig. 10a and $\pm\,\xi_{m,Var}/2$ in Fig. 10b. Correlation coefficient R^2 in Fig. 2.10a equals 0.97, a value slightly higher than for (*GS*, $\partial\theta/\partial h$) noon correlation. Nighttime correlation coefficient is again lower than daytime, with a value $R^2 = 0.88$. In Fig. 2.10a, *Var* overestimates the MLD value for altitudes below 1.1 km (40% of the data). In Fig. 2.10b, the overestimate occurs for altitudes below 0.7 km (30% of the data). In both daytime and nighttime correlation plots, *GS* estimations of MLD and RL height are statistically higher than those computed by *Var* for most of the altitude intervals. This is consistent with the positive bias $b_{m,n}$ shown in Figs. 2.7 and 2.8.

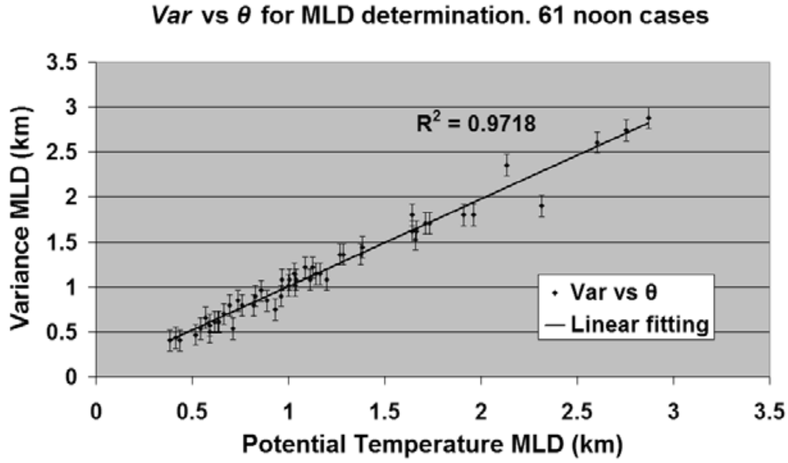

Fig. 2.10a. Correlation between MLD computed by *Var* and $\partial\theta/\partial h$ for 61 noon cases. Error bars amplitude $\xi_{n,Var}$ on y-values is equal 240 m, correlation coefficient is 0.90. The slope and the offset of the fit line are 0.924 and 0.073 km, respectively.

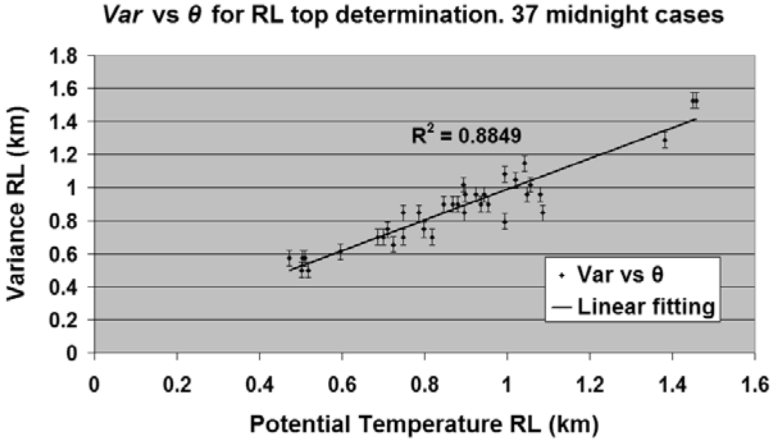

Fig. 2.10b. Correlation between RL computed by *Var* and $\partial\theta/\partial h$ for 37 midnight cases. Error bars amplitude $\xi_{m,Var}$ on y-values is equal to 90 m, correlation coefficient is 0.88. The slope and the offset of the fit line are 0.932 and 0.057 km, respectively.

2.3.3.3 Height of nocturnal aerosol layers

For the determination of NAL height I select the altitude of the higher *Var* maximum, i.e. the one likely matching the top of NAL (see Fig. 2.4b). The uncertainty due to the variation of the single NAL heights computed during the one-hour average is indicated by $\xi_{m,GS,Var}$ and determines the amplitude of the error bars in the correlation plots (see Figs. 2.11a and 2.11b).

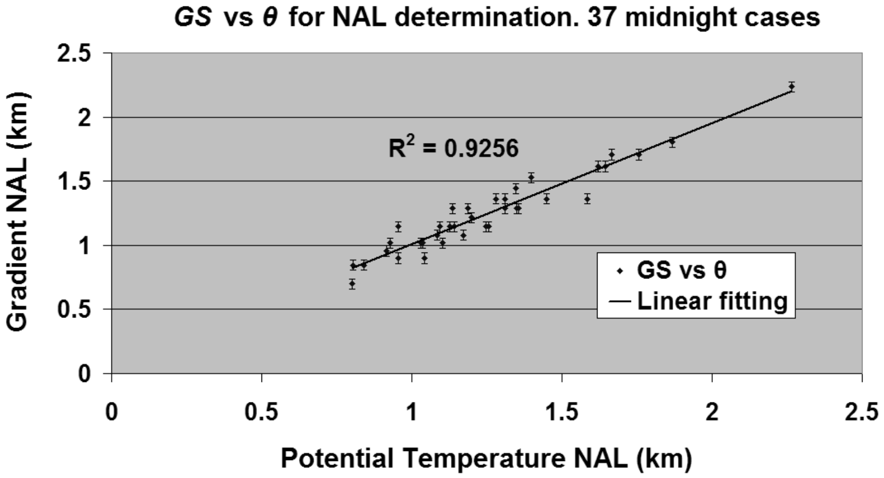

Fig. 2.11a. Correlation between NAL computed by *GS* and $\partial\theta/\partial h$ for 37 midnight cases. Error bars amplitude $\xi_{m,GS}$ on y-values is equal to 80 m, correlation coefficient is 0.92. The slope and the offset of the fit line are 0. 944 and 0.063 km, respectively.

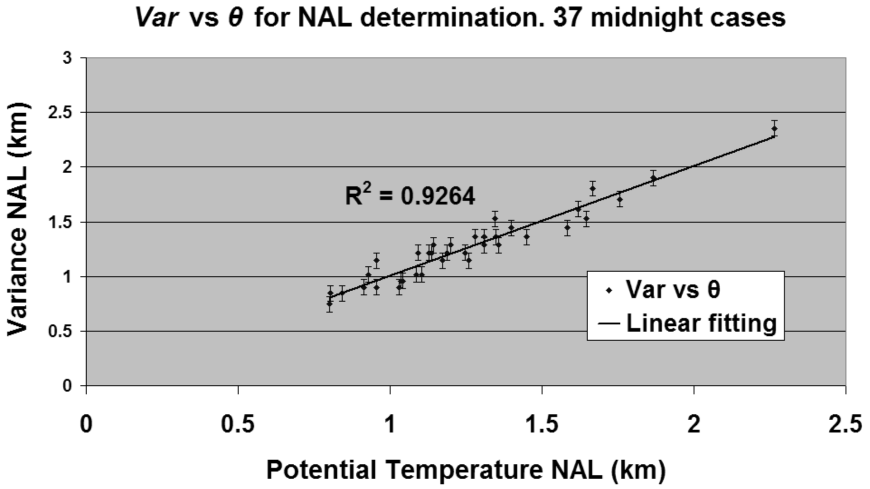

Fig. 2.11b. Correlation between NAL computed by *Var* and $\partial\theta/\partial h$ for 37 midnight cases. Error bars amplitude $\xi_{m,Var}$ on y-values is equal to 140 m, correlation coefficient is 0.92. The slope and the offset of the fit line are 1.005 and 0.001 km, respectively.

As for MLD and RL determination, for NAL also the values of $\xi_{m,GS}$ and $\xi_{m,Var}$ come from an average of the vertical differences between the highest and the lowest peak of GS_i and Var_i during one-hour for some representative case. The obtained values for $\xi_{m,GS}$ and $\xi_{m,Var}$ are 80 m and 140 m, respectively. The value of U_{tot} for NAL heights has the same expression as in Eq. (2-4), where the bias $b_{m,n}$ is replaced by b_m computed from the distribution in Fig. 2.12.

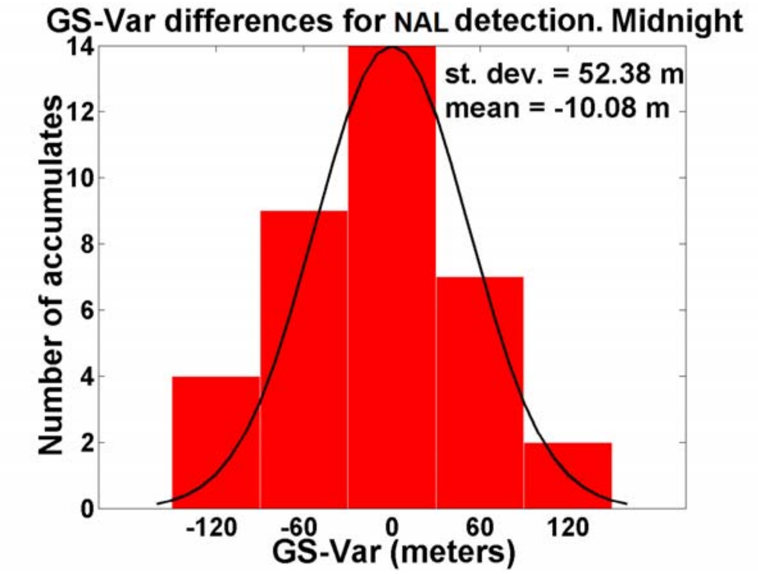

Fig. 2.12. Histogram of NAL_{GS}-NAL_{Var} values. *x*-axis resolution is 60 meters equal to the *GS* and *Var* vertical resolution at 1 km.

As evidenced in Figs. 11a and 11b, NAL heights distribute mainly between 0.8 and 1.8 km. The retrieved correlation coefficients R^2 are comparable: 0.925 for (GS, $\partial\theta/\partial h$) and 0.926 for ($Var$, $\partial\theta/\partial h$). In the altitude interval 0.8-1.8 km, the linear fit of (GS, $\partial\theta/\partial h$) provides underestimate of NAL height for altitudes above 1.16 km, i.e. in 65% of the cases. In the same altitude interval, *Var* maxima gives an overestimate of the NAL height as it is detected by $\partial\theta/\partial h$, for altitudes above 0.87 km, i.e. the 80% of the cases. In accordance to this, the mean value of the distribution of differences between NAL_{GS} and NAL_{Var} in Fig. 2.12 is negative. This shows that the levels of *Var* maxima are statistically higher than the levels of *GS* minima.

2.4. Wind shear vertical profile for MLD and aerosol layers detection: two case studies.

Wind shear can also be an indicator for the ML top altitude. Rapid changes in wind direction immediately above the ML normally correspond to the level at which the horizontal wind passes from sub- to nearly-geostrophic. A comparison between the wind shear vertical profile and the aerosol layers detected by the lidar signal, gives valuable information about the aerosol stratification. Actually, the relation between the altitudes of largest shear and those of maxima and minima in *Var* and *GS*, respectively, is an additional, useful tool to compare lidar and radiosonde methods.

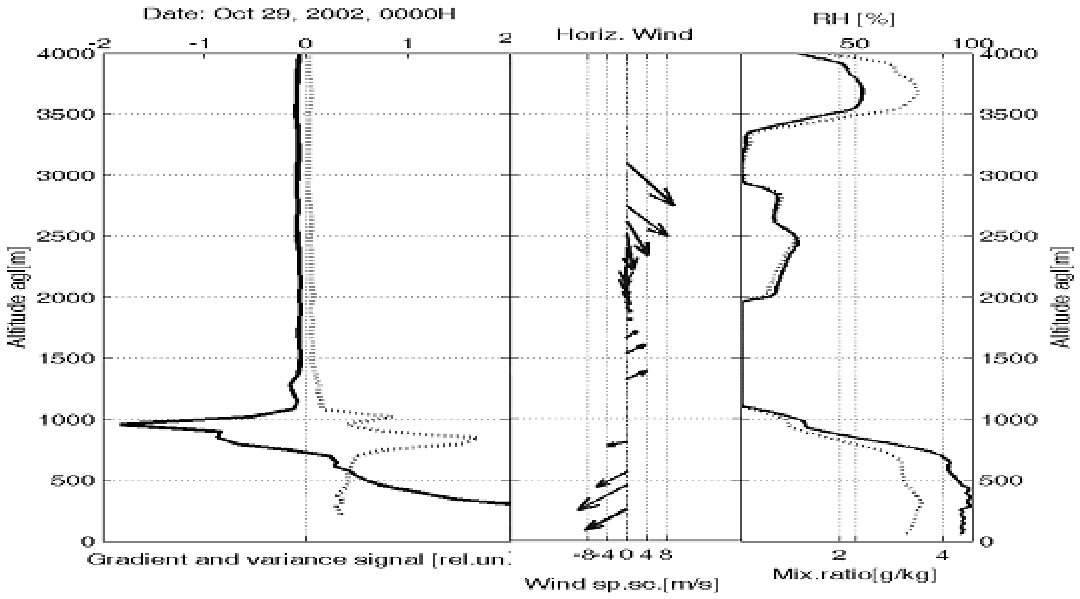

Fig. 2.13. October 29, 2002, 0000 UTC. In left panel: gradient (continuous, upper axis) and variance (dotted, upper axis) profiles. Second and third panels: profiles from radiosonde measurement at Payerne station. In the central-panel, wind vector with respect to altitudes; In right panel: relative humidity (dotted) and water vapour mixing ratio (continuous) profiles.

In Fig. 2.13 it is presented a case of lidar and radiosonde comparison in which the wind shear and the relative humidity (and water vapour mixing ratio) have the same role as the potential temperature vertical profile in the previous sections. The case is the 29 October 2002 and measurements were carried out at midnight in Neuchâtel (lidar) and in Payerne (radiosonde). From the vertical vector-profile of the wind it is possible to retrieve the information about the RL top altitude. The wind intensity decreases with altitude and reaches a minimum at around 1000 m, above this level the intensity starts to increase again. The wind direction is also symmetrical about the RL top as detected by *GS* and *Var* having a maximum shear around 1000 m. Actually, the wind blows from NE inside the BL and from SW immediately above it. The right panel in Fig. 2.13 shows the vertical profiles of the relative humidity and the water vapour mixing ratio. The relative and real water contents drop at the level of the RL top and confirm the level already detected by the wind shear.

Another example is shown in Fig. 2.14, in this case the sharp gradient in the wind direction is compared to the lidar data only. While the case described above correlates the maximum of wind shear with the height of the BL top, the case below intends to establish the correlation between wind shear and an aerosol layer above the ML.

13th of August 2001, noon

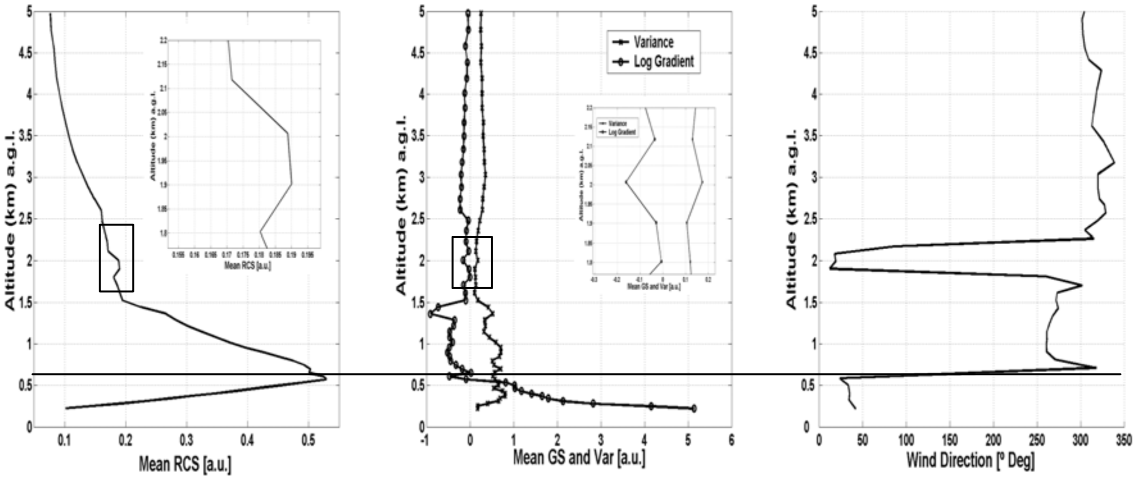

Fig. 2.14. From left to right, the three panels show vertical profiles of: mean *RCS*, mean *GS* and *Var*, and wind direction. Lidar data were averaged over a time interval of 1 hour. The centre of the time interval corresponds to noon when wind radiosoundings were carried out. The horizontal solid line intersects the *y*-axis at the level of MLD as computed by the *GS* method (612 m a.g.l.). The two inner rectangles in the left and central panels are zooms showing the aerosol layer at 2 km well defined by the wind shear.

Fig. 2.14 sketches an example for such comparison performed on 13 August 2001, at noon. The vertical wind profile in the right panel is retrieved from radiosonde performed at the Meteosuisse aerological station in Payerne. The horizontal solid line intersects the *y*-axis at the level of the MLD as computed by the *GS* method (612 m a.g.l.). At this height, the wind abruptly changes its direction by about 90º, likely matching the ML top as detected by lidar. Above the ML, the wind direction remains almost constant except for a layer centred at 2 km. At this altitude, the *RCS*, *GS* and *Var* profiles show a little peak highlighted by the black rectangles and shown in detail in the zooms. This case study is a clear example of full correspondence between lidar methods *GS* and *Var* and the wind shear not only in retrieving the MLD, but also in detecting the aerosol stratification above it.

2.5. Conclusion

This study presents a comparison between backscatter lidar and radiosonde temperature methods for the determination of the BL stratification. Measurements were performed in different synoptic conditions, but always in cloud-free low troposphere. The retrieved lidar MLD for daytime and the heights of RL and NAL for nighttime have been compared to the heights of temperature inversion layers detected by radiosounding. A total of 98 cases (61 for daytime, 37 for nighttime), have been statistically evaluated.

For daytime the correlation coefficient R^2 equals 0.96 when comparing the lidar gradient method (*GS*) with the radiosonde potential temperature gradient ($\partial\theta/\partial h$). A similar value, 0.97, is obtained when correlating the lidar variance method (*Var*) with $\partial\theta/\partial h$.

For nocturnal cases the correlation coefficients are slightly lower, $R^2 = 0.90$ for (*GS*, $\partial\theta/\partial h$) and $R^2 = 0.88$ for (*Var*, $\partial\theta/\partial h$). The lower values of R^2 during nighttime are due to the aerosol multilayer structure present immediately above the RL top that makes more difficult its height detection.

The top altitude of NAL detected by the lidar instrument is in good agreement with θ vertical profiles. The correlation coefficients are $R^2 = 0.92$ for (*GS*, $\partial\theta/\partial h$) and $R^2 = 0.93$ for (*Var*, $\partial\theta/\partial h$).

As we see, the correlation between lidar and radiosonde methods in detecting MLD, RL and NAL heights has coefficients always greater than 0.88 for both day and nighttime. The combination of the lidar signal gradient and variance allows non-ambiguous identification of the MLD in convective conditions, as well as the aerosol stratification, including RL and NAL heights in nocturnal stable BL. The evaluation of these altitudes is done by a simple and efficient algorithm that consents automated data processing. This is an advantage when performing continuous long-term lidar measurements of the BL development. In summary, this study shows that the heights of ML, during day, and of the RL and NAL, during night, can be retrieved directly from backscatter lidar data and may be related to the BL structure as represented by the temperature profile.

As an additional information on the BL vertical extent and the aerosol stratification above it, it is shown, in Section 2.4, the wind radiosonde measurements. The value of wind shear through the BL and the few kilometres above it, is an indicator of the transition zone between two systems in which the low-level flow is decoupled (in intensity and direction) from the flow above. This is true for both transitions between BL and FT and between an aerosol layer and the air above and below it, as shown in Fig. 2.13 and 2.14. In conclusion, a maximum of shear in the vertical profile of the wind can be related to the maximum and minimum of, respectively, *Var* and *GS*.

As it was put previously, the validation of lidar measurement of the aerosol stratification through the BL and the few kilometres above it is presently a very active topic in this research field (Menut et al. 1999; Sicard et al, 2006; Wiegner et al, 2006). The presented study is the first in its kind in terms of covering all diurnal cycles and seasons, as well as by its large statistical database. It provides a conclusive justification for using lidar for the characterization of the daily cycle of the BL development.

Chapters 3 and 4 are precisely two such examples of the characterization of the boundary-layer made possible by the results of Chapter 2. The algorithm used here will be further developed in Chapter 3 to obtain the fast-variation of the BL top, as well as it will be used in Chapter 4 when processing the routine measurements performed in Basel.

Chapter 3

Frequency of boundary-layer top fluctuation in convective and stable cases

The previous chapter presented a validation, showing that the BL aerosol stratification obtained by lidar corresponds to the temperature stratification obtained by radiosonde measurements. This gives the possibility to investigate a further process occurring within and at the top of the BL using the elastic backscatter lidar. The new problem is if it is possible to use the lidar methods to determine the variations of the BL top with high resolution. Part of this problem is to identify if the obtained frequency of BL top variation brings information about the nature of the processes occurring at these altitudes.

The frequency of thermals up- and downdraft, during the day, and that of gravity waves, during night, were retrieved by applying a fast Fourier transform to the temporal evolution of the convective and nocturnal BL tops. The principal components of each obtained spectrum of frequency were related to the dominant processes occurring at the convective and nocturnal BL tops. For diurnal cases, in conditions of weak horizontal wind, the purely convective process dominates. For these cases, the up- and downdraft frequency is higher for shallow convective BL and decreases for deeper ones. In case of strong horizontal wind, the frequency directly depends on wind velocity. For nocturnal cases, the principal frequencies did not show a direct relation to the nocturnal BL depth. Fluctuations at the nocturnal BL top height can occur even if the conditions through its depth are statically stable. These oscillations are principally due to wind shear and buoyancy (gravity) waves at the altitude of the nocturnal BL top. The objective of this work is to study the convective and nocturnal BL top fluctuation and to identify their main frequencies of variation.

Motivations of the study

One of the most critical processes controlling the balance of pollutants at the top of the convective boundary-layer is represented by the air-exchange between air parcels coming from the layer aloft, the FT, and those coming from below the boundary-layer top. The region in which this exchange process can be observed is the EZ. Previous studies (Neu et al., 1994; Beyrich and Gryning, 1997) investigated the mechanisms leading to air-mixing within the EZ with the objective to individuate the best methods to determine its depth and to understand the role that the EZ and the temporal variation of its thickness have in the concentration of near-surface pollution within the BL. A question left open by these studies is still the quantification of the *rate* of this air-exchange and then the possibility to determine how and where pollutants are transported outside of the BL. Actually, experimental measurements of the fast-evolution of the BL top using remote sensing instrumentation represent an important source of information for studies and modelling of long-range transport. A way to study the process of air-exchange between BL and FT and the *rate* at which it happens through the daily cycle is the continuous observation of the convective processes (up- and downdrafts) occurring at the convective BL (CBL) top and the inertial waves that modify the altitude of the nocturnal BL (NBL) top. The observation of waves within and at the top of the BL using remote sensing instrumentations has been done up till now mainly involving scientific campaigns and airborne measurements over specific areas. The motivation of this study is to understand if it is possible to observe these mechanisms of air-exchange using a ground-based lidar and to identify the frequency of the principal process producing it.

Background

The up- and downdrafts of BL convection is the primary way the atmosphere moves heat, moisture, momentum, and pollutants between the earth's surface and the atmosphere. Thus, BL convection is important for the global climate modelling, numerical weather prediction (De Wekker et al. 1997; Rampanelli et al. 2004; Zampieri et al. 2005), air quality, and the dynamics of numerous mesoscale phenomena. The CBL is part of BL, its height is an important parameter characterizing the mixing of its constituent (Stull, 1988; McIlveen 1992; Siebert et al. 2001).

In order to draw a detailed information from the lidar signal it is required a good signal to noise ratio (SNR) from lidar profiles. The temporal and vertical resolutions are two key parameters that contribute to determine the final value of the SNR (see discussion in Sections 2.3.2 and 5.2.1). High resolutions allow to detect fine structures in the temporal evolution of the interface between the CBL and the FT, but increase significantly the noise component in the signal. Previous studies (Steyn et al, 1998; Hägeli, 1998; Hägeli et al, 2000) used high resolutions and described the dynamics of the region containing this interface, i.e. the EZ. Steyn et al (1998) proposed a new method to identify the mixing layer depth and the EZ thickness; this method, based on fitting a four parameter, idealized profile to observed profiles, was improved further by Häegeli et al. in 2000. Häegeli focused on the importance of the flux ratio in describing properly the process of air-entrainment from the FT into the CBL and vice versa. The results of its investigation showed that the *entrainment flux ratio* (the ratio of the air entrained from the FT to the one entrained from the CBL) is spatially highly variable and that induces relatively large variations in the observed CBL height (CBLH). Due to intense exchange between CBL and FT air parcels, at the level of the CBL top, the backscatter lidar signal varies considerably with time accordingly to the probed aerosol load. The process of mixing at this altitude suggests then to use, as a convenient tool for the CBLH detection, the temporal variability of the backscatter signal, i.e., the variance.

During the night the dynamics of air mixing and exchanging are substantially reduced and are, at mid-latitude, rarely induced by convective processes. Turbulent motions within the NBL often occurs in short, but intense, bursts. The wind speed profile is often referred to as a low-level, or nocturnal jet. The low-level flow is often decoupled from the flow aloft within the low-level jet. It is possible for the surface winds to be calm, while, a few tens of meters aloft, the winds are 30-40 m s^{-1}. When the vertical shear of the wind is large, instability arises in form of Kelvin-Helmholtz (KH) waves. The condition for KH instability to be activated is that the (gradient) Richardson number is negligible compared to the wind shear. The NBL top often corresponds to the level at which this condition is accomplished. In Section 3.3.3 the possible causes of the NBL top fluctuations are investigated by analyzing the frequency spectra of five selected winter cases.

This chapter presents lidar observations performed during five diurnal summer cases and five nocturnal winter cases measuring, respectively, the CBL and NBL temporal evolutions with high resolutions. The two groups of five case studies each were selected on the basis of similar meteorological conditions with comparable values of temperature, pressure and wind direction to study the frequency of rising and sinking CBL and NBL tops. In Chapter 2, it has been shown the convenience of using the gradient and the variance methods to retrieve the altitude of the current BL top (both day and night) as well as the altitude of the (advected) aerosol layers aloft. For this study the variance method will be used, combined with the gradient, to compute the CBLH/NBLH from each lidar profile during the period of measurement. An automated algorithm implements both lidar methods to retrieve from lidar data the CBLH/NBLH with high temporal and altitude resolutions. The algorithm outputs are the temporal evolution of the diurnal and nocturnal BL top altitudes and the time series of the range corrected lidar signal.

3.1. Thermal formation

The site of measurement is, as in Chapter 2, the city of Neuchâtel (47.000°N, 6.967°E, 485 m a.s.l.). The local topography is then again represented by the lake on the south of the city and by the Jura mountain range on its north.

During summer days, in cloud-free conditions, hot air, heated by the ground surface, rises and generates thermals. The convective process produces an inflow toward the centre of the thermal base and initiates breeze from the lake. When thermals are vigorous, the air entrained from the surroundings may force a down-flow along the Jura slope contrasting the anabatic circulation (Blumen, 1990; McIlveen, 1992). The growing convergence zone draws air with different aerosol content inside the actual CBL. When the lifting condensation level (LCL) approximately corresponds to the CBL top, thermals containing a sufficient amount of moisture may reach it and condense forming cloud layer (Stull, 1988. Outline at p. 11). Conversely, thermals growing over dry land are less buoyant and rarely reach the LCL. The first temperature inversion above the ground is the level at which the buoyant air parcels cease to lift. In conditions of moderate convection the maximum level reached by thermals coincides with the CBL top and both correspond to the capping temperature inversion. Actually, when the top of thermals rises into the inversion layer, becomes negatively buoyant and decelerates. This can eventually lead to thermals sinking back down into the CBL, a process called penetrative convection (Scorer, 1957; Deardorff, et al., 1969; Stull, 1973). Several small thermals have not the necessary energy to reach the CBL top and collapse at some level inside the convective layer. This is confirmed by the fact that the number of well-defined thermal events decreases with height within the CBL (Greenhut and Khalsa, 1987). When convection is strong (like in tropical regions), thermals can rise through the first statically stable layer and develop through the FT. In this study are considered cases in which thermals grow through the depth of CBL, reach its top and then sink back down into it. In particular, this study focuses on the last two phases of the process developing inside the EZ and causing the CBL top to rise and fall.

As mentioned before, thermals that form above a humid surface are more buoyant than if they formed above dry soil. When a thermal does not reach the LCL, the undiluted air inside the core rises up to the thermal top and gradually loses its energy. At the top, the air starts to diverge from the core and then to sink in columns of downdraft. When a thermal reaches the LCL, the air within starts to condense releasing latent heat and maintaining the core warm. At the thermal's edges, the evaporation cools the air that begins to drop through the EZ. Downdrafts at the thermal sides entrain air from the FT. This introduces new air into the CBL resulting in dilution of its aerosol content and growth of its depth.

An upward looking, ground-based lidar can probe several air parcels with different aerosol load when operating with moderately high temporal resolution. When rising moist air in the thermal core enters the field of view (FOV) of the lidar, a large value of the backscattered signal returns to the telescope. On the other hand, when the lidar probes the sinking drier air parcels, the backscatter signal value considerably decreases.

3.2. Lidar instrument and methods

3.2.1. The lidar

The lidar deployed for the measurements presented in this chapter has been described in Chapter 1 and 2 (Sections 1.5.1 and 2.2). The case studies selected for this study are part of a large dataset collected during the period from May 2000 to February 2003, in the frame of the EC project EARLINET (Bösenberg et al., 2002; Bösenberg and Matthias, 2003). The lidar equation and the two lidar methods, the gradient *GS* and the variance *Var*, have the expressions shown in the previous chapters (i.e., Eq. (1-24) and Eqs. (2-1) and (2-2), respectively). The equations of *GS* and *Var* are nevertheless presented below, in Section 3.2.2, to highlight the differences in the use of the two methods with respect to Chapter 2. The altitude of full overlap between the FOV of the telescope and the laser beam section is, for the selected cases, about 400 m (i.e., $O(h) \equiv 1$ when $h > 400$ m a.g.l.). After corrections, profiles with initial vertical resolution of 6 m are averaged over two vertical bins decreasing the resolution to 12 m.

3.2.2. Lidar methods: GS and Var

In this study, the two methods, *GS* and *Var*, are implemented in only one algorithm computing the altitudes of local minima and maxima. The process is iterated over a time interval with length equal to the index *i* in Eq. (3-1) and (3-2). Differently from Chapter 2, here all single GS_i and Var_i profiles are used to provide single evaluations of the BL heights (BL height temporal evolution) and not to be averaged over a long time interval (BL height single averaged value).

The equation of the gradient method *GS* is:

$$GS_i(h) = \frac{d}{dh}\log\left(RCS_i(h)\right) = \frac{d}{dh}\log\left(\beta(h)\right) - 2\alpha(h) \tag{3-1}$$

Where RCS_i are again the single profiles of range corrected lidar signal. The index *i* identifies each single profile and has length equal to the total duration of the measurement. Since the time resolution of a single profile is 60 s, for one-hour-and-a-half measurement *i* goes from 1 to 90.

A standard vertical profile of the aerosol backscatter represents the CBL and the few kilometres above it. The backscatter value and gradient along its vertical profile provide a comprehensive information of the lower tropospheric stratification. Actually, in the CBL, the aerosol backscatter remains almost constant due to homogeneous mixing of air parcels up to the altitude of the first temperature inversion. The aerosol backscatter abruptly decreases starting from this level and a corresponding local *GS* minimum indicates the CBL top.

As in Chapter 2, variance method is applied for each point *sliding* on the temporal axis (see Fig. 2.3 in Chapter 2). Variance of *RCS* has then the expression:

$$Var(h)_i = \frac{1}{N} \sum_{k=i+1-N/2}^{k=i+N/2} \left(RCS_k(h) - \overline{RCS(h)_i} \right)^2 \tag{3-2}$$

For 90 minutes of measurement i goes from 5 to 85. The parameter N is the length of k-index, $N = 10$. The index of summation k, represents the individual measurements $k = i - 4 \ldots i + 5$ along the N-time interval. The mean value $\overline{RCS(h)_i}$ is obtained by averaging the single RCS_k profiles over the N-interval. Each single $Var(h)_i$ profile gives the information about the variability of the backscatter signal at altitude h, during the N-interval with respect to $\overline{RCS(h)_i}$.

3.2.3. Thermal up- and downdraft frequency

In purely convective condition the up- and downdraft process moves air between the top and the bottom of the CBL with a time period $t_* = (CBLH_*)/w_*$ depending on the depth of the CBL, $CBLH_*$, and on the vertical velocity, w_*. In several cases the horizontal wind is not negligible and may become dominant in determining the up- and downdraft frequency at the CBL top. The regular change of up- and downdraft regions, advected by the wind through the laser FOV, has a higher frequency according to an increasing horizontal wind speed. If wind is light, thermals may stay attached to the hot spot where they form. If not, thermals may form repeatedly over the hot spot and drift downwind. Thermals drift with the average wind over their height, so they may travel at a higher speed and in a somewhat different direction than the surface wind. In such condition, at the top of the CBL, two consecutive thermals pass through the lidar FOV with a time rate $t = (1.5 \cdot CBLH)/u$ (Caughey and Palmer, 1979; Young, 1988), where u is the mean horizontal wind speed at the CBL top and the CBLH equals now the thermal mean diameter. The factor 1.5 in the expression of t comes from airborne observations of the horizontal thermals distribution (Young, 1988). Since generally u is much greater than w_*, ($u \gg w_*$), it follows that the time of a whole up- and downdraft process through the lidar FOV is $t < t_*$ even when $(1.5 \cdot CBLH) > CBLH_*$ (see Fig. 3.1).

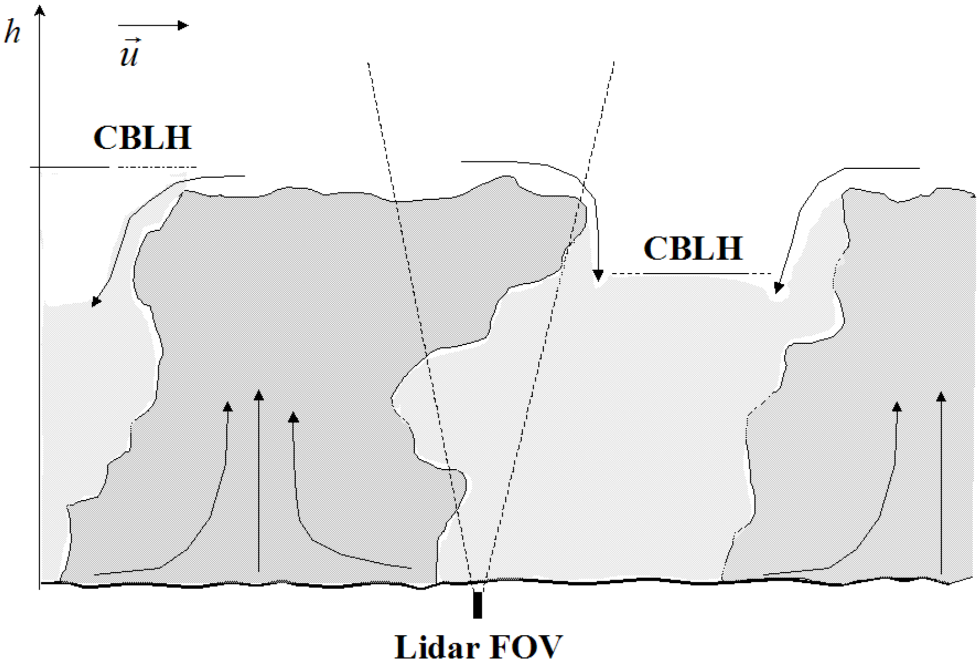

Fig. 3.1. The outline shows an idealized vertical cross section of thermals. The vector quantity $\vec{u}$ represents the horizontal wind moving the thermals downstream through the lidar FOV. The CBLH is at higher level in updraft regions and at lower level in downdraft regions.

3.3. Signal processing and observations

3.3.1. *The algorithm*

In Fig. 3.2 are sketched the algorithm operations for the CBLH retrieval from lidar data. The algorithm computes mean $\overline{GS}$ and $\overline{Var}$ profiles from single GS_i and Var_i profiles averaged over 30-minutes with i going from 1 to 30. The applied altitude and time averaging on RCS_i profiles reduces, as discussed in Chapter 2, the shot noise contribution by a factor $E = \left(N_p N_b\right)^{0.5}$, where N_p and N_b are again the number of profiles and the number of bins used for averaging. Hence, the uncertainty due to shot noise after the average is $\sigma_{Av} = \sigma_{shot} \times E^{-1}$. In the case of $\overline{GS}$ and $\overline{Var}$, $N_p = 30$ and $N_b = 2$, so E is about 8. The reduction of false signal peaks allows to consider the principal minima and maxima of $\overline{GS}$ and $\overline{Var}$ as real atmospheric features and not as induced by shot noise.

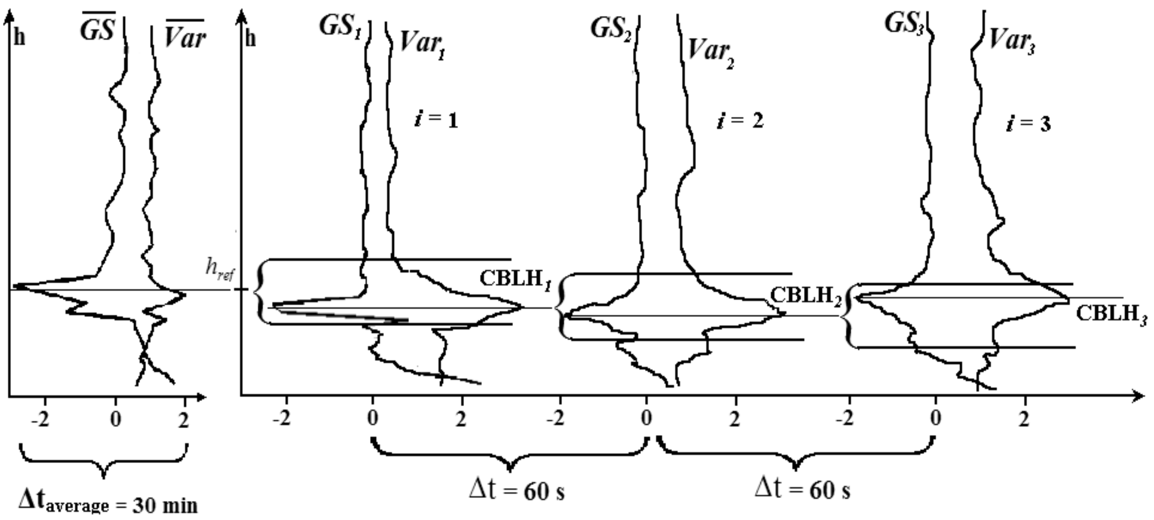

Fig. 3.2. Synopsis of the lidar algorithm for CBLH retrieval. Mean $\overline{GS}$ and $\overline{Var}$ are averaged on a time interval $\Delta t_{average}$ = 30 min. Using the mean profiles I compute the reference height h_{ref}., used to initiate the process. Single GS_i and Var_i profiles have temporal and vertical resolutions, respectively, Δt = 60 s and Δz = 12 m.

The algorithm steps are:

i. Starting from the ground level, the algorithm detects the heights of the first minimum and maximum of $\overline{GS}$ and $\overline{Var}$, respectively. The mean value between the two heights is a reference height, h_{ref}. For a set of measurements starting at 1200 UTC, $\overline{GS}$ and $\overline{Var}$ are the mean profiles representing the time interval 1200-1230 UTC.

ii. For $i = 1$, a vertical window centered in h_{ref} and with extension equal to $0.15 \cdot h_{ref}$, limits the vertical region in which to search the principal minimum and maximum of GS_1 and Var_1, respectively. As an example, for $h_{ref} = 1$ km, the window extension is 150 m, from 0.925 km to 1.075 km. The mean value between the detected heights of the GS_1 minimum and that of the Var_1 maximum represents the altitude of the CBL top (CBLH$_1$).

iii. With reference to Fig. 3.2, sliding along the time-axis, the algorithm detects, in the range of altitudes imposed by the window (for $i > 1$ the window extension is $0.15 \cdot \text{CBLH}_{i-1}$), a new value of CBLH at each i-step.

iv. When $i = 31$, the algorithm computes two new $\overline{GS}$ and $\overline{Var}$ profiles averaged over the successive interval 1230-1300 UTC. The whole process computed for the first 30 i-steps is repeated for i from 31 to 60 with a new initial h_{ref} value. All CBLH$_i$ values computed at each steps result from an average between the heights of GS_i minimum and Var_i maximum.

v. The algorithm is structured in blocks of 30 steps untill the end of the dataset. No residual profiles are left out of the last block being the total dataset length equal to 90.

3.3.2. *Observations: convective case*

Five case studies of CBL temporal evolution are selected. The initial and final time of measurement and the parameters characterizing the CBL during the observation are shown in Table 3.1. All measurements have duration of one-hour-and-a-half and are performed during the central hours of the day, between 1230 and 1830 UTC. The described automated algorithm retrieves the CBLH temporal evolution from the lidar data during the periods of observation reported in Table 3.1.

Table 3.1. Physical and thermodynamic parameters characterizing the CBL during five convective case studies

Date	Period of measurement (UTC)	T (ºC)	u_{30m} (m s^{-1})	$u_{\overline{CBLH}}$ (m s^{-1})	$\overline{CBLH}$ (m)
22 Aug 2001	1230-1400	24.5	4.2	13	1035
23 Aug 2001	1230-1400	24	1.8	2	660
22 Jun 2002	1330-1500	28.5	2.5	20	2500
15 Aug 2002	1700-1830	25	3	3.5	1450
30 Aug 2002	1240-1410	24.5	3	9.5	1440

In Figs 3.3 (a)-(e) are shown the time-evolutions of CBLH (white or black line) and the *RCS* time series.

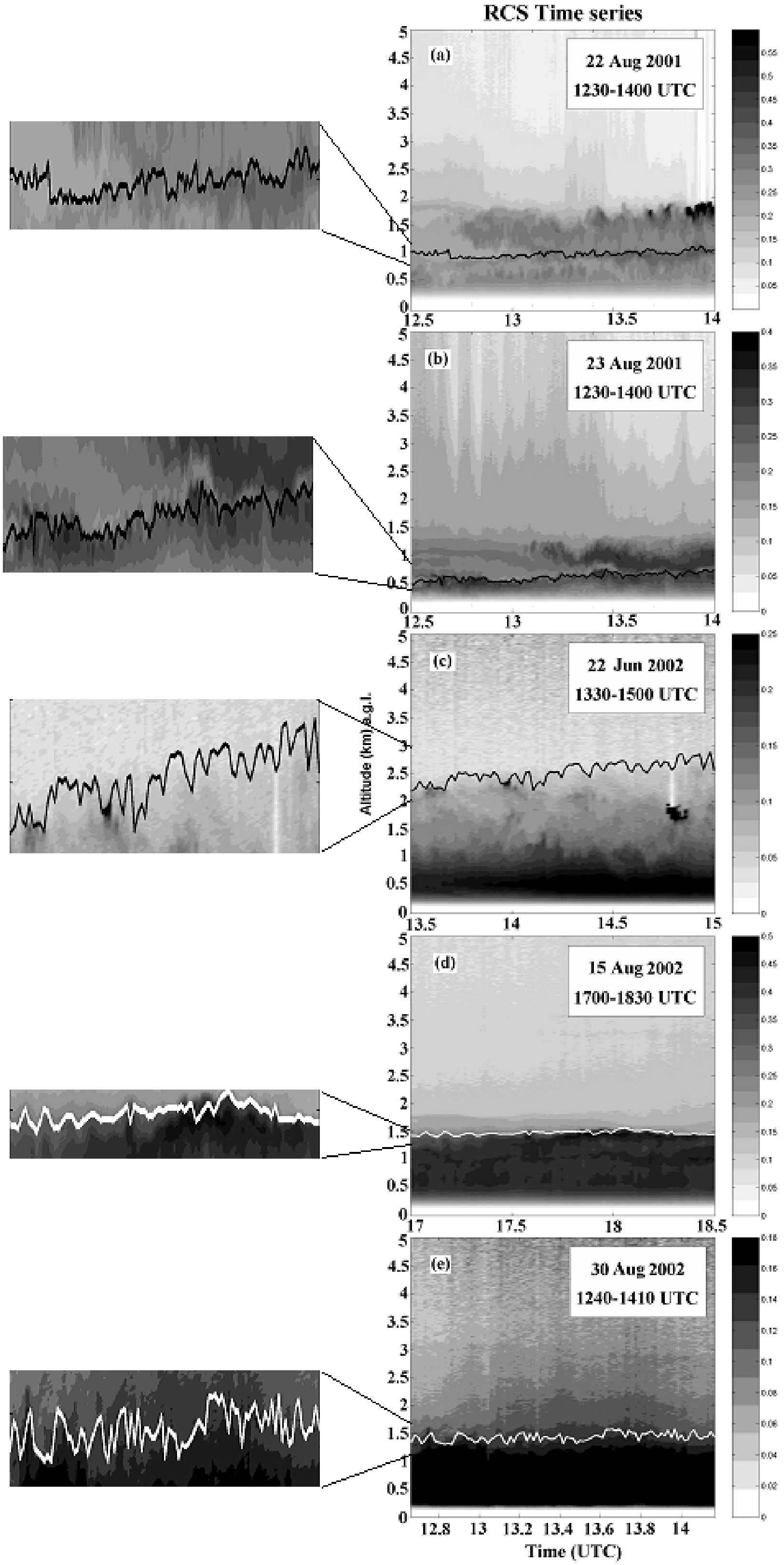

Fig. 3.3. Five case studies of CBLH temporal evolution (white or black line) and *RCS* time series are computed by the algorithm described in Sect. 3.3.1 and depicted in Fig. 3.2. Darker regions correspond to high aerosol backscatter. All measurements have duration one-hour-and-a-half from 1230 to 1830 UTC. On the left side of the figure enlarged parts of the CBLH temporal evolution are shown in rectangles.

Due to time resolution and total duration of measurement, each temporal evolution of CBLH counts 90 data points from the beginning to the end of measurement. A fast Fourier transform (FFT) is applied to the 90 CBLH-points to study the periodical fluctuations of the CBL top. The rate of sampling, imposed by the acquisition system, is $f_s = 0.016$ Hz. The Nyquist frequency is then $f_{Nyq} = 0.5 \cdot f_s = 8 \cdot 10^{-3}$ Hz which allows the investigation of the part of spectrum between 0 and f_{Nyq} Hz.

The Brunt-Väisäillä frequency is defined as:

$$N^2 = g \frac{d \ln \theta}{dh} \tag{3-3}$$

Where g is gravitational acceleration and θ the potential temperature. The Brunt-Väisäillä frequency N^2 depends on altitude h and, at the height corresponding to the mean CBL top altitude, has values between 0.009 and 0.016 Hz for all the studied cases. This a priori excludes the presence of the Brunt-Väisäillä component in the spectrum [0 - f_{Nyq}] Hz. This is a useful information when interpreting the FFT spectra in Figs 3.4(a)-(e).

3.3.2.1 Case studies

In purely convective conditions (negligible horizontal wind speed), the up- and downdraft process is responsible for the principal fluctuations of the CBL top. Table 3.1 shows the averaged depth of the CBL over each time interval, these values are different for each case. For comparable values of w_* I expect the time $t_* = CBLH_*/w_*$ to increase with increasing $CBLH_*$ values. The distance Δf (expressed in Hz) between the principal frequency components of each spectrum is not so large as it could be expected if the conditions were always purely convective. Also the sign of Δf, is not for all cases the one it could be expected. For example, the cases of 23 August 2001 and 22 June 2002 have two very different averaged *CBLH* values, 660 m and 2500 m, respectively. If the conditions were purely convective It could have been expected a much higher frequency for the case of 23 August 2001 with shallow CBL depth. On the contrary, the principal frequency components in the two cases are in the reverse order, i.e. a higher frequency with a thicker CBL. To explain this apparent inconsistency, it is necessary to consider the horizontal wind velocity at the level of the CBL top. The horizontal wind plays an important role in moving thermals downstream with time rate $t = (1.5 \cdot CBLH)/u$. Values of wind velocity at the level of CBLH shown in Table 3.1 come from noon-radiosoundings (UTC time) performed at the Meteosuisse aerological station in Payerne (20 km South of Neuchâtel). Values of temperature and horizontal wind speed at 30 m come from the Meteosuisse meteorological station in Neuchâtel.

The cases of 22 and 23 August 2001 in Figs. 3.4, in panels (a) and (b), show principal frequency peaks in agreement with the respective CBLH values: a higher frequency for the case 23 August 2001 with shallow CBL (660 m, mean depth) and a lower frequency for 22 August 2001 with a deeper CBL (1035 m, mean depth). The wind is almost constant through the CBL depth for the 22 August 2001 and increases with altitude for 23 August 2001.

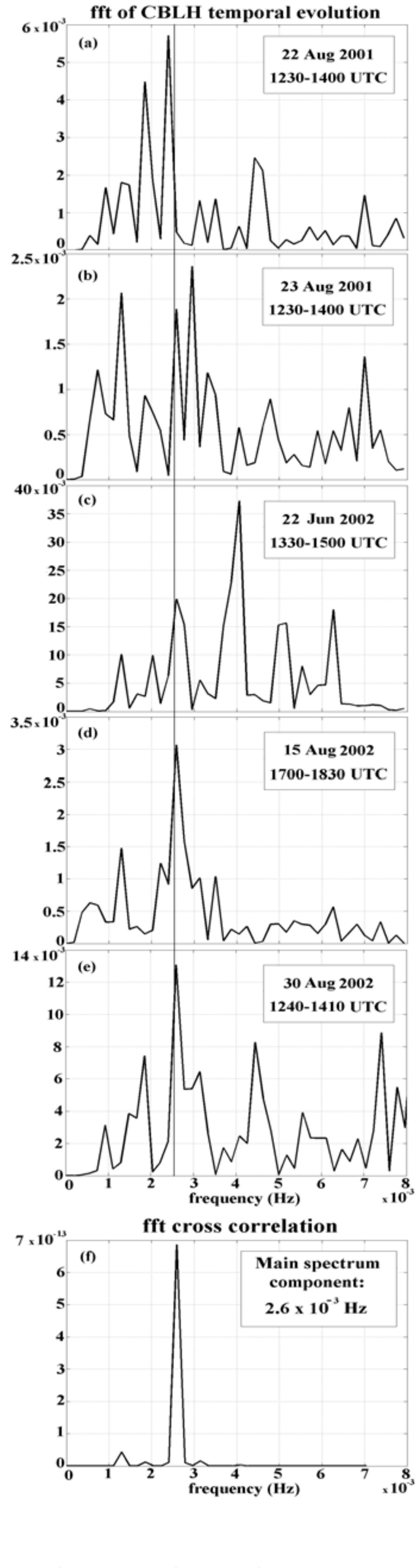

Fig. 3.4. From panel (a) to panel (e) are shown the FFT spectra computed from the temporal evolution of the CBLH in Fig. 3.3. In panel (f) is presented the cross correlation of the above five spectra. One frequency is common to all spectra, $f_{cross} = 2.6 \cdot 10^{-3}$ Hz. Each spectrum counts 90 data points; the frequency of sampling is $f_s = 0.016$ Hz. The Nyquist frequency is then $f_{Nyq} = 0.5 \cdot f_s = 8 \cdot 10^{-3}$ Hz

For the case of 22 June 2002 the horizontal wind at the CBLH had a value of 20 m s^{-1}, considerably higher than the other cases. The main spectrum component in panel (c) corresponds to a relatively high frequency ($\sim 4 \cdot 10^{-3}$ Hz) with respect to its value CBLH (2500 m, mean depth) and if compared to the principal frequency values in the other spectra. This frequency is then determined principally by the process with time period $t = (1.5 \cdot CBLH)/u$. The last two cases, the 15 and 30 August 2002, have similar CBLH, temperature and 30 m-wind speed values. The two respective spectra have both a principal maximum around $3 \cdot 10^{-3}$ Hz. It is then probable that the main process determining the CBL top fluctuation for these two cases is the purely convective one.

3.3.2.2 Cross correlation between the individual spectra

Panel (f), in Fig. 3.4, shows the cross correlation between the FFT spectra in panels (a) to (e). The main spectrum component is $f_{cross} = 2.6 \cdot 10^{-3}$ Hz, a frequency corresponding to a fluctuation occurring in all the five cases. The presence of a common frequency in all spectra indicates that the fluctuation f_{cross} cannot depend directly on the parameters presented in Tab. 3.1. This fluctuation must depend on common CBL dynamics, or on topography, or on wind direction (wind blows from SE in all the studied cases). One interpretation of f_{cross} arises from the combined effects that topography and wind direction have on the temporal evolution of the CBL top. Two different measurements of the wind direction have been retrieved, one from the MeteoSuisse meteorological station in Chasseral (1599 m a.s.l) and one from the Neuchâtel station (485 m a.s.l.). Both, Neuchâtel and Chasseral, give for the five case studies the same direction of horizontal wind (SE) during the period of lidar observations. The concurrence of wind direction at two different atmospheric levels let suppose a general south-easterly wind circulation over a synoptic area. Wind blowing from SE comes across an obstacle before reaching Neuchâtel. A low-elevation hill range between the Lake of Neuchâtel and the Lake of Morat extends parallel to the Jura axis for about 8 km. The highest peak is Mt. Vully (653 m a.s.l.), 260 m above the level of both lakes. Due to the small altitude of the hill range, the *Froude number* (Stull, 1988) is $\mathrm{Fr} \approx 1$, even for weak wind. Lee waves may then form vertically above or horizontally downwind the obstacle. In the linearity theory, the *Scorer* parameter is defined as,

$$l^2(h) = \frac{N^2}{U^2} - \left(\frac{\partial^2 U}{\partial^2 h} \right) \frac{1}{U}. \tag{3-4}$$

It depends on altitude h, wind velocity, U, and Brunt-Väisäillä frequency, N^2. The value of $l(h)$ is usually strongly decreasing with height inside the CBL. Above the level of the first temperature inversion, $l(h)$ is nearly constant with height and conditions are favourable for vertically propagating mountain waves. Since the hill range altitude is below the level of the first temperature inversion for all the studied cases, waves forming beyond the hill range become trapped inside the CBL and propagate toward Neuchâtel (see Fig. 3.5).

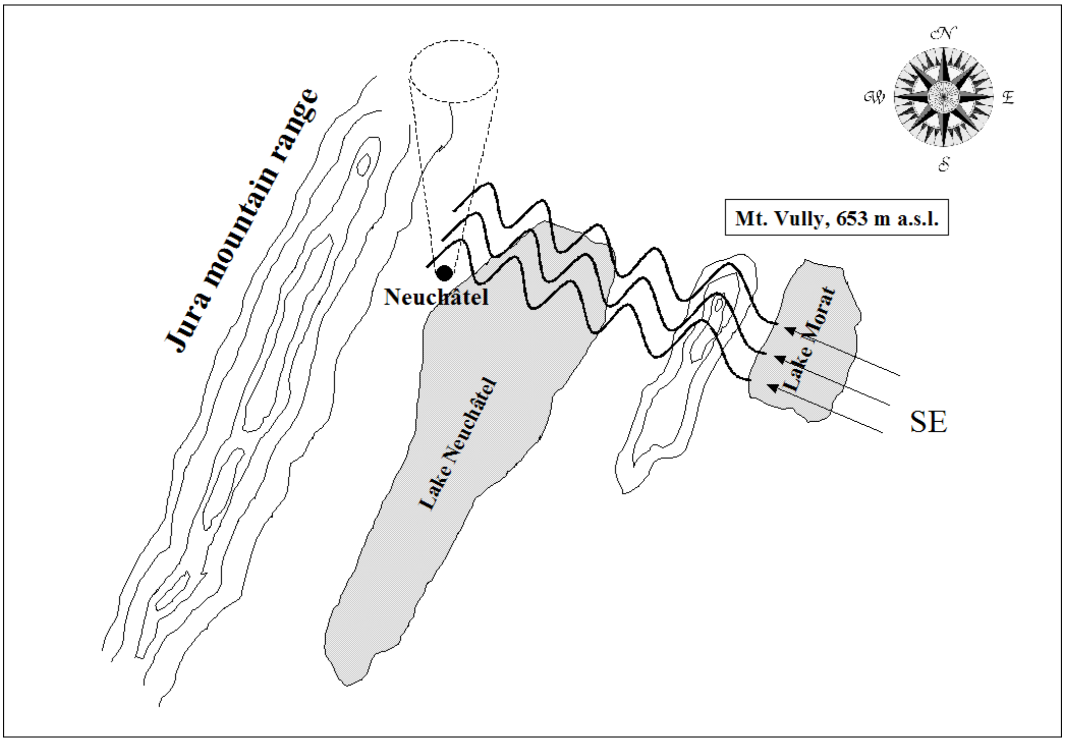

Fig. 3.5. The outline depicts the local system of trapped lee waves occurring within the CBL above Neuchâtel when the wind is from SE. The obstacle that generates this wave field is the low-elevation hill range between Lake Morat and Lake Neuchâtel. The highest peak is Mt. Vully (653 m a.s.l.). Changes in the upstream value of wind and Brunt-Väisälä frequency during the period of measurement modify the group velocity and the wavelength on the lee of Mt. Vully.

For a ground-based backscatter lidar, stationary trapped lee waves is a still system and does not contribute to CBL top temporal fluctuation. Exceptions to this steady wave-system occur for two principal reasons. Following recent studies (Caccia et al., 1996; Ralph et al., 1996; Nance et al., 1997), trapped lee waves may evolve over time as a non-stationary wave-system. Temporal variations of group velocity and wavelength may occur on the lee of the hill as the parameters in Eq. (3-4) change upstream. Another exception to the system stationarity is represented by the expected wave reflection at the Jura southern mountain side. Since the angle of incidence is not equal to 90º, there will be a superposition of prograde and retrograde waves resulting in a pattern of constructive and destructive interference. For these reasons, the wave field above Neuchâtel cannot be interpreted as a stationary one during the period of lidar observation. The peak of frequency f_{cross} in Fig. 3.4(f) may then be determined by the non stationary component of the wave field.

Another interpretation of f_{cross} comes from the CBL dynamics on the small scale. Kelvin-Helmholtz (KH) waves can exist in the EZ on different scales. On largest scale KH waves arise from shear between sub- and nearly-geostrophic wind, respectively, inside and above the CBL. On the smaller scale, KH waves may form along the top boundary of overshooting thermals and determine the periodical CBL top rise and fall (Rayment and Readings, 1974). Top of thermals are marked by a sharp interface with FT air. This rough gradient between two different air parcels can lead to very strong shears and statically stable lapse rate across a distance of few meters. The KH waves that may form in such a situation are of type short-wavelength and evolve rapidly over time during the ascent phase of thermals through the EZ (see the outline in Fig. 3.6). The whole process of wave formation, break and decay in turbulence takes few minutes, with a wave period comparable to the one determined by f_{cross}.

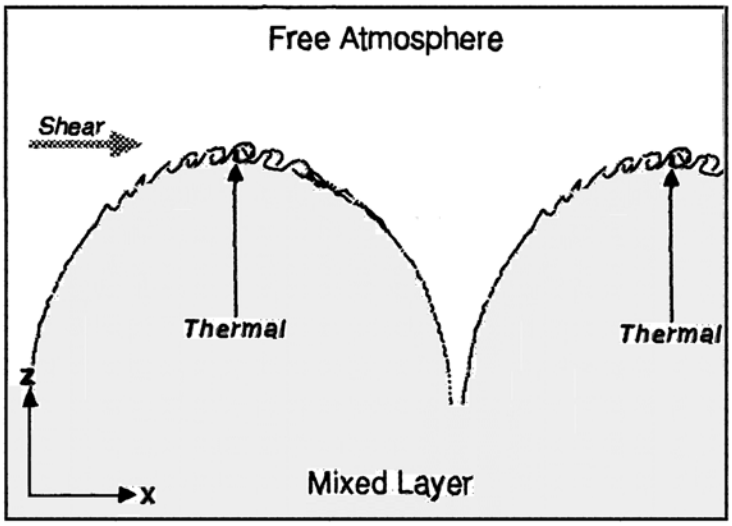

Fig. 3.6. Small-scale KH waves can form at the top of overshooting thermals due to height-increasing shears and stability (Stull, 1988; Rayment and Readings, 1974)

3.3.3. Observations: non-convective case

Temporal fluctuations of the actual BL top occur also in stable, non-convective conditions. During night, into the NBL, many factors can determine turbulence, like inertial oscillations or drainage flows. Generally, there is a superposition of these different factors determining a complicated, non-linear behaviour of the NBL. As during the day, also during night it is difficult to identify with sufficiently high precision which are the dominant processes determining the different peaks of frequency in a FFT spectrum. In this section I investigate the oscillations occurring at the NBL top and principally due to wind shear and buoyancy (gravity) waves.

3.3.3.1 case studies

Five winter, stable, nocturnal cases of BL temporal evolution are presented. Cases in Fig. 3.7(a)-(e) show the *RCS* time series and the temporal evolution of the BL height. Actually, the black/white line superimposed on the *RCS* time series indicates the height of the NBL top.

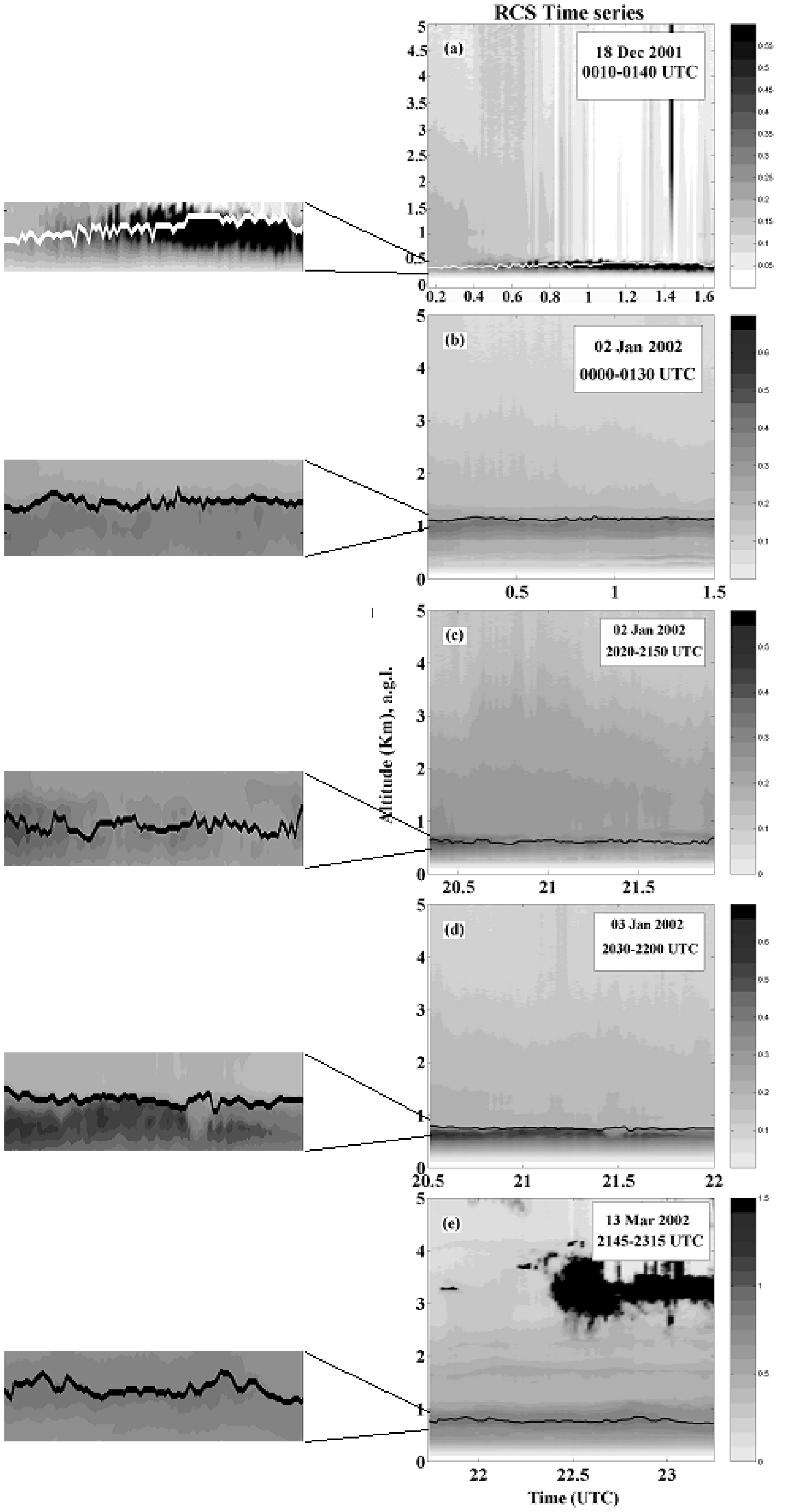

Fig. 3.7. From panel (a) to (e) are shown five stable, non-convective cases of time development of nocturnal stable BL height (white/black line) and *RCS* time series. The NBLH remains quite constant during the whole period of measurement in each case. Measurement duration is one-hour-and-a-half. Time intervals are shown in Table 3.2 as well as the mean NBLH values. On the left side of the figure enlarged parts of the CBLH temporal evolution are shown in rectangles.

The mean temperatures at 2 m observed at the MeteoSuisse Neuchâtel station during the period of measurement are reported in Table 3.2 as well as the values of the horizontal wind intensity at 30 m. The wind at the level of the mean NBL height (NBLH) is an extrapolated value from radiosoundings measured at the MeteoSuisse aerological station in Payerne. Inside the NBL the wind is calm with values between 0.5 and 3.5 m s^{-1}. The observed wind speed in the five cases is in good agreement with the expected range speed of the katabatic wind (Stull, 1988, p 535).

Table 3.2. Physical and thermodynamic parameters characterizing the NBL during five stable case studies

Date	Period of measurement (UTC)	T (ºC)	u_{30m} (m s^{-1})	$u_{\overline{CBLH}}$ (m s^{-1})	$\overline{CBLH}$ (m)
18 Dec 2001	0010-0140	-2.5	3.5	16	430
02 Jan 2002	0000-0130	-5	1.2	13	1130
02 Jan 2002	2020-2150	-3	1	9	612
03 Jan 2002	2030-2200	-2.7	2	9	747
13 Mar 2002	2145-2345	11	0.5	2	776

The wind direction in all the cases oscillates, during the period of measurement, between NE and NW. Katabatic flow from Jura slope is a north-westerly wind, then in a ambient mean north-easterly flow it is normal to observe a swinging between this two directions. At higher levels the wind intensity increases in all cases except for the case of 13 March 2002; for this case the wind remains almost constant through the NBL depth. All cases are measurements taken some hours after the sunset in order to reduce at the minimum the possibility of a residual convection due to a temperature gradient between ground (warmer) and the overlying air (cooler). The duration of measurements is one-hour-and-a-half as for the convective cases and the time intervals are shown in Table 3.2. In two cases the lidar measured during the first hours after midnight, i.e. 18 December 2001 and 02 January 2002. In Fig 3.7(a)-(e) the temporal evolutions of the NBLH are quite constant with small altitude variations always around the mean NBLH values. The case of 18 December 2001 presents the lowest NBL top with a mean height equal to 430 m.

In Fig. 3.8(a)-(e) are sketched the frequency spectra obtained by applying a FFT to the NBLH temporal evolutions in Fig. 3.7 (a)-(e). In panel (a), the FFT spectrum shows the temporal variations of a particularly shallow NBL.

During night, internal waves with frequency less than the Brunt-Väisälä value remain trapped within the NBL resulting in horizontally propagating waves also at the level of the NBL top. One type of waves can be generated by wind shear, as it happens during day on the top of thermals.

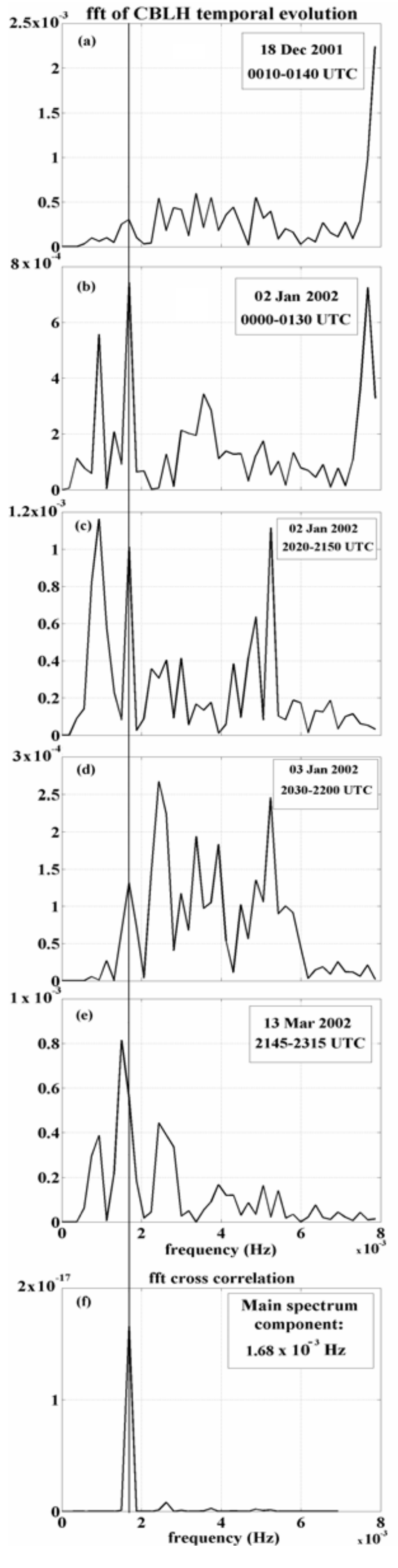

Fig. 3.8. From panel (a) to (e) are presented the spectra of frequency for five stable, non-convective cases. The five spectra have been obtained as for the convective cases, applying a FFT to the temporal evolution of the NBLH in fig. 3.7(a)-(e). Each spectrum counts 90 data points; the frequency of sampling is $f_s = 0.016$ Hz. The Nyquist frequency is then $f_{Nyq} = 0.5 \cdot f_s = 8 \cdot 10^{-3}$ Hz. In panel (f) is shown the cross correlation between the five spectra above, the common frequency is, $f_{cross} = 1.68 \cdot 10^{-3}$ Hz

Theory suggests that laminar flows become unstable under the action of wind shear leading to KH-wave formation at the levels where the (gradient) Richardson number (*Ri*) is negligible compared to the shear intensity (Stull, 1988, pp 527-529).

$$Ri = \frac{\dfrac{g}{\theta_v}\dfrac{\partial \theta_v}{\partial z}}{\left[\left(\dfrac{\partial U}{\partial z}\right)+\left(\dfrac{\partial V}{\partial z}\right)\right]^2} \tag{3-5}$$

Where θ_v is virtual potential temperature, T_v is virtual absolute temperature, z is height, g is gravitational acceleration, and (U, V) are the wind components toward the east and north. The nominator is a term of stability and the denominator provides the characteristic vertical shear of the wind. The levels at which KH waves may form are called the *critical levels*. At these levels the value of *Ri* is smaller than the critical Richardson number, R_c (it is generally accepted that turbulence appears when $Ri > R_c$, $R_c = 0.21$). Payerne radiosounding provides a spot measurement of the wind direction around 0000 UTC. The profile shows that at the altitude of the NBL top there is a strong shear. This local maximum in the wind shear supports the hypothesis of the presence of KH-waves at the level of NBLH. A qualitative analysis of each spectrum shows that in only one case there is an isolated, well pronounced peak of frequency, the 13 March 2002 in panel (e). In all the other cases there are always at least two peaks of frequency of comparable intensity.

3.3.3.2 Cross correlation between the individual spectra

In panel (f), in Fig. 3.8, it is shown the cross correlation between all the spectra. In this case the common frequency ($f_{cross} = 1.68 \cdot 10^{-3}$ Hz) is shifted back to a lower value compared to the convective case. Comparing the five spectra in panels (a) to (e) it emerges that f_{cross} is one of the principal frequency component in each case. In particular, for the 2 January 2002 (0000-0130) and the 13 March 2002, f_{cross} corresponds to the principal peak of frequency. Each spectrum contains the several, simultaneous frequencies of oscillations occurring at the NBL top. The process with frequency f_{cross} denotes the oscillation characterizing each of the five cases without being necessarily the dominant one. The KH-wave formation may occur during all the presented cases as induced by the strong shear at the level of NBL top. The passage of KH-waves through the lidar FOV during the period of measurement is then one reliable interpretation for the frequency f_{cross}.

3.4. Conclusion

This study is an investigation of the frequency characterizing the fluctuations occurring at the BL top during convective and stable cases. In the first part of the chapter, five summer, convective cases of BL height temporal evolution have been studied. In the second part, five stable, non-convective cases with the same procedure as for the convective cases are described. For both convective and stable cases the height-variations of the diurnal and nocturnal BL top during a period of 90 minutes was analyzed.

In the first part, attention was given to convective processes occurring through the depth of the CBL. Top fluctuations of the CBL with time period of about $t_* = CBLH_*/w_*$ are due to up- and downdraft processes (thermals formation and breakdown). For cases in which the horizontal wind is much stronger than the vertical buoyancy, thermals are moved downstream through the telescope FOV with time rate $t = (1.5 \cdot CBLH)/u$. Several processes contribute with different frequencies to the periodical fluctuation of the CBL top. To detect all the frequency components a FFT was applied to the CBLH time-evolution during the period of measurement.

The studied cases are similar, they have been selected for summer, clear convective and cloud-free conditions. Cross-correlating the FFT spectra, one peak of frequency (f_{cross}) arises as common component of the five cases. Interpretation of f_{cross} comes from the combined topography and wind direction and from the thermals dynamics. They can be summarized in two points:

i. A system of non-stationary trapped lee-waves, may form on the lee of Mt. Vully and propagate toward Neuchâtel when wind is blowing from SE. Variations in the lee waves wavelength and group velocity due to change of the parameters in Eq. (3-4) upstream of the hill may determine a fluctuation of the CBL top.

ii. Thermals rising through the EZ experiment a strong gradient of static stability and shears at their tops. A system of short-wavelength Kelvin-Helmholtz waves can form on the top surface of the penetrating thermal. This system fast evolves over time and makes the CBL top to rise and fall as the waves pass through the telescope FOV.

Analysis of the FFT spectra is then based on four different processes. The first two: thermals are moved through the telescope FOV by two different mechanisms, one purely convective and one due to the mean horizontal flow. The second two: the CBL top altitude changes over time due to the action of non-stationary lee-waves propagating in the lower atmospheric layers above Neuchâtel; Kelvin-Helmholtz waves with time period of few minutes induced by shear at the top of thermals determine periodical fluctuation of the CBL top.

All processes contribute to entrain air from the FT inside the CBL diluting the aerosol content inside it. Using the presented automated algorithm with high temporal and vertical resolution, it is possible to retrieve from lidar signal the fluctuation at the CBL top and to provide an estimation of the rate of air entrainment inside the CBL.

In the second part of the chapter, are studied processes leading to internal NBL gravity wave formation. As for the convective case, five cases with similar meteorological nighttime stable conditions were selected. The parameters characterizing the atmosphere up to the level of the NBL top are summarized in Table 3.2. In all cases, measurements were taken some hours after the sunset when was possible to assume the temperature of the ground not to be greater than that of that of the overlying air. In only one case (13 March 2002) some low clouds (~3 km) appeared during the period of measurement, but for the night cases the cloud presence is not critical as for diurnal ones. In fact, for convective cases the cloud shadow modifies the buoyancy flux at the surface, reducing also the energy of thermals and the time period of the whole up- and downdraft process. During night clouds reflect the infrared radiation back to the ground what prevents the temperature to drop, but do not necessarily affect the direction of wind, or the intensity of the shear.

For each case, the total duration of measurement is one-hour-and-a-half, implying a length of 90-points for each FFT spectrum. An analysis of the five FFT spectra showed that also for the stable case there are several frequency components of comparable intensity representing each an oscillation of equivalent importance. The two processes determining the NBL top variation I particularly focused on are the nocturnal gravity waves and the shear of the wind. The Kelvin-Helmholtz waves formation at the level where the wind shear is dominant compared to the buoyancy force provides a valid interpretation of the cross correlation peak, f_{cross}, in Fig. 3.8(f).

Finally, the aim of this study it is not to provide the only possible reason that determines a fluctuation, but to present a valid interpretation of the dynamics developing within the BL and that could engender this fluctuation. The objective was to interpret the results of the cross correlation shown in Fig. 3.4(f) and 3.8(f) investigating which of the numerous processes occurring in the CBL and NBL could produce the periodic rise and fall of their tops. The Kelvin-Helmholtz waves are a good interpretation to this peak of frequency in both the convective and the nocturnal, stable cases.

In summary, in the field of study of wave processes within and at the top of the BL, the elastic backscatter lidar with the described algorithm brings the possibility to carry out the investigation from the ground and on a routine basis. The ground-based lidar observations do not involve aircrafts and are more efficient than the satellite observations. Aircrafts observations are limited by the few number of passages over the studied atmospheric region. Satellites need the presence of cloud in order to observe waves. Lee-waves that give rise to a cloud pattern are visible to a satellite, but not a lee-wave system in cloud-less atmosphere as the one described in this chapter. In perspective, such lidar method makes it possible to investigate during long period of time and in cloud-free condition allowing an evaluation of the exchange processes (like the pollution) between BL and the FT. It shall be also noticed that it will be desirable to validate in representative cases this type of wave observation with a reference to the traditionally accepted methods (Alpers and Stilke, 1996; Gubser et al., 1999; Lane et al. 2000; Doyle and Smith, 2003)

Chapter 4

Daily cycle development of urban boundary-layer. BUBBLE field campaign

In a number of cases it is necessary to operate a lidar in remote sites with a minimum personnel attendance on the spot. This requires a stability of operation, automatic functioning and remote control of the instrument status, and data downloading. Such backscatter lidar is realised by Observatory of Neuchâtel and was operated for one year in Basel, Switzerland as part of the Basel UrBan Boundary Layer Experiment (BUBBLE project). Important tasks in such long-duration study are the signal processing and the results evaluation, requiring the elaboration of large amount of data. The experiment BUBBLE combined near-surface and remote sensing instrumentation to obtain a detailed synopsis of the urban boundary-layer. Our lidar continuously measured for one year between summer 2001 and summer 2002, collecting data in the form of time series of backscattered lidar signal.

Motivations of the study

The height of the boundary-layer is a parameter of critical necessity to evaluate the ecological status of the atmosphere above urban sites (Menut, 1997; Menut et. al., 1999; Dupont et al., 1999; Piringer and Joffre, 2005; Fisher et al., 2005). This parameter is needed to know the volume in which the pollutants are mixed (and then trapped), i.e., knowing the pollution fluxes, it may be possible to provide estimation of their concentration. The determination of BL top height in urban environment is still an unsolved problem, since the use of radiosondes and sodars is necessarily limited in time. In addition, radiosondes provide values integrated over short periods of time, i.e. over few minutes, while lidars can measure for long periods of time and in uninterrupted way.

As it is shown in Chapter 2 and 3, the lidar provides the height of the BL well validated with reference to the traditionally accepted measurements. This opens the possibility to employ lidar in routine measurements of this parameter, where continuous observations are needed. The international program, COST 715 (**CO**operation in the field of **S**cientific and **T**echnical Research), is the oldest and widest European intergovernmental network for cooperation in research. The BUBBLE project was part of COST 715and invited our lidar to participate to this experiment to provide a reference value of the BL height in urban environment throughout the whole campaign.

The motivation of this study is then to prove that the elastic backscatter lidar is the instrument capable to determine this reference parameter (i.e., the height of the UBL) over long periods of time and in continuous way. This has been realized participating to the field campaign of one year of duration and measuring the height of the urban BL top above the centre of the city of Basel, Switzerland.

Background

A good knowledge of the lower tropospheric dynamics over a urban site is based on the monitoring of the chemical and physical processes occurring in that area and allows to predict pollution development during specific events (i.e., intense emissions in shallow urban boundary-layer, undiluted PM10 and PM2.5 for long periods of time, etc…). One priority in air-quality studies is to have a sufficiently large database indicating the status of pollutants over cities and industrial sites. The possibility of continuous atmospheric lidar measurements for long periods allows to collect large amount of data. Processing of the collected data and computation of the lidar and atmospheric variables through the whole period of observation contribute to form a climatology of the principal urban boundary-layer (UBL) parameters Actually, lidar is a convenient instrument for uninterrupted monitoring of gases and aerosol diluted in the BL. Menut et al. (1999) studied the UBL height (UBLH) over Paris using combined lidar and radiosonde measurements. The results for four case studies showed that lidar instrument could provide continuous, unattended and accurate determination of the height of the BL. This aspect is important in the frame of the interaction between lidar measurements and models prediction. Other studies (Boers et al., 1984; Boers et al., 1987) of lidar BL height determination demonstrated that lidar data can be used for model predictions.

The operational wavelength of our lidar (532 nm) is optimal to probe also particles like fine dust and droplets. The obtained data can be processed as it has been shown in Chapter 2 and 3 taking advantage of different lidar methods, i.e. the gradient and the variance. For this study only the gradient method is used to retrieve the UBLH from lidar data.

The UBL presents a specific and much different structure, compared to the standard BL vertical structure and development over flat terrain. Over rough surface it develops a turbulent, non-homogeneous surface layer called *Urban Canopy Layer* (UCL) ranging from the ground up to approximately the average height of roughness elements (z_H) like buildings and trees. The UCL is part of the *roughness sublayer* (RS), a layer with height $z_* > z_H$. This height depends on the density of the roughness elements and it is generally expressed (Raupach et al., 1991) as $z_* = a{\cdot}z_H$ with a between 2 and 5. Above the RS there is an *inertial sublayer* (IS), a layer characterized by a sufficiently large Reynolds number and in which the vertical profile of the wind velocity is almost logarithmic. The Reynolds number,

$$\mathrm{Re} = \frac{UL}{\nu} \tag{4-1}$$

is the ratio of the inertial force ($\sim U^2/L$) to the viscous force ($\sim \nu U/L^2$) where U is a characteristic velocity, L is a characteristic length, and ν is the kinematic viscosity of the fluid. Turbulence occurs when the inertial term dominates the viscous term, that is, when the Reynolds number is large. Above the IS the urban boundary-layer is largely determined by advective processes. This outer part of the UBL is not clearly defined by either convective or stable processes and it is called outer urban boundary layer (Rotach et al., 2005) and extents up to the UBL top. In Fig. 4.1 is sketched the vertical urban boundary-layer structure with attention to the various sub-layers described above.

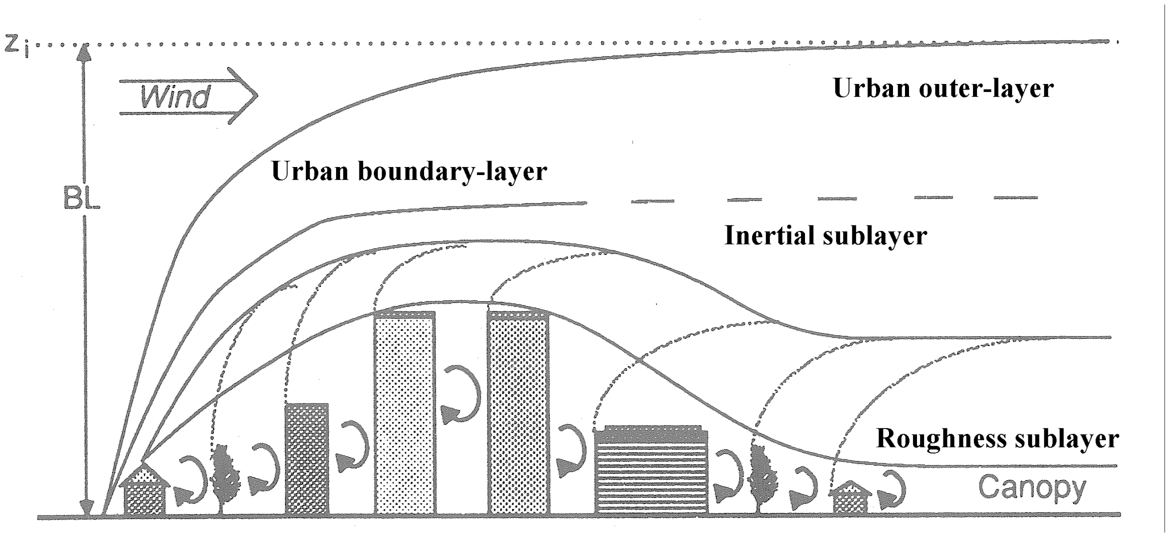

Fig. 4.1. Urban boundary layer vertical structure. (modified after Oke 1987)

This chapter presents the results obtained in monitoring the UBL in two different ways. In the first part of the chapter, two case studies are presented of UBL daily cycles above the city of Basel. The two cases represent two extremely different UBL developments: a hot summer day with sharp UBL growth during the central hours of the day and an extremely cold winter day with very smooth UBL development. For both case studies, five parameters are retrieved from the meteorological stations installed in Basel to support lidar data in describing the UBL dynamics. The meteorological parameters are: short-wave downward radiation and long-wave upward radiation, friction velocity, absolute humidity and air temperature. The objective of this first part is to show the consistency between lidar and surface meteorological measurements in describing the UBL development for both convective and stable conditions.

The second part of the chapter presents a statistic of UBL heights retrieved from the collected lidar data during one year of measurement. In this case, the objective is to show that an automated lidar is a convenient instrument to monitor the BL independent from other instrument measurements.

4.1. The lidar and the site

The lidar used for this study is described in Chapter 1, section 1.5.2. In addition to the information already given, I provide here further details about the acquisition system. A number of house-keeping parameters are registered: the power of the laser at 532 nm in relative units, temperatures of the separate lidar subsystems (laser, detectors, electronics), voltages and currents. The data acquisition and the house-keeping electronic systems are controlled by a micro-processor. A local PC is used to control the lidar measurements and to store the collected data. The operation of the local PC is controlled via Internet by a remotely installed computer for start/stop of the measurement, house-keeping and lidar data transfer. The lidar, without the local PC, is assembled as a single unit. This unit is put in a box with isolation and dumping of the mechanical shocks, where it is transported and from where it may also operate. During the lidar operation in Basel, the lidar was mounted in an environmental protection cabinet, having a window on its tilted roof (see Fig. 4.2).

Fig. 4.2. The lidar installed on the 5th floor balcony of the Institute of Meteorology, Climatology and Remote Sensing in Basel. The lidar is in the dark green box (for protection and transportation), referred as 'lidar unit' in Table 1.2 in Sect. 1.5.2. The white cabinet is an environmental protection for the lidar during the period of measurement.

The cabinet was positioned on the 5th floor balcony of the building of the Institute of Meteorology, Climatology and Remote Sensing at University of Basel (278 m a.s.l.). The cabinet was also equipped with autonomous temperature control by heating and air-conditioning.

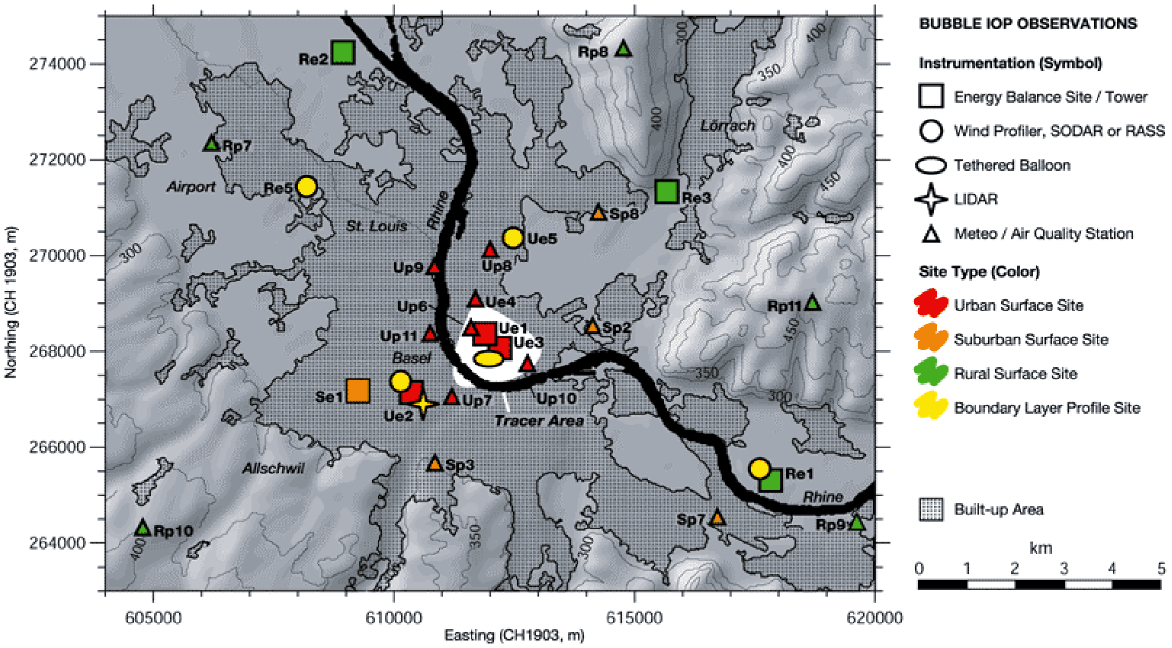

Fig. 4.3. Overview over the BUBBLE observations in the greater area of the city of Basel. The thick black line denotes the river Rhine. All other symbols are explained in the inlet. Note that site Ue2 (Spalenring) is where the lidar was installed for measurements.

In Fig. 4.3 it is shown the map of the measurement stations during BUBBLE with the tracer area (white). The tracer area was the area from which tracers were emitted during specific period of intense observation (IOP). Our lidar was positioned in the site Ue2 immediately out of the tracer area.

4.2. UBL monitoring by lidar and meteorological instruments. Two case studies

4.2.1. Meteorological variables

In BL dynamics the earth's surface mainly determines the intensity of the buoyancy flux as well as the structure of the surface layer. Surface receiving the incoming solar radiation transmits direct heating to the lower atmospheric layer over it. In Fig. 4.4 it is shown the net amount of incoming solar energy at different atmospheric layers.

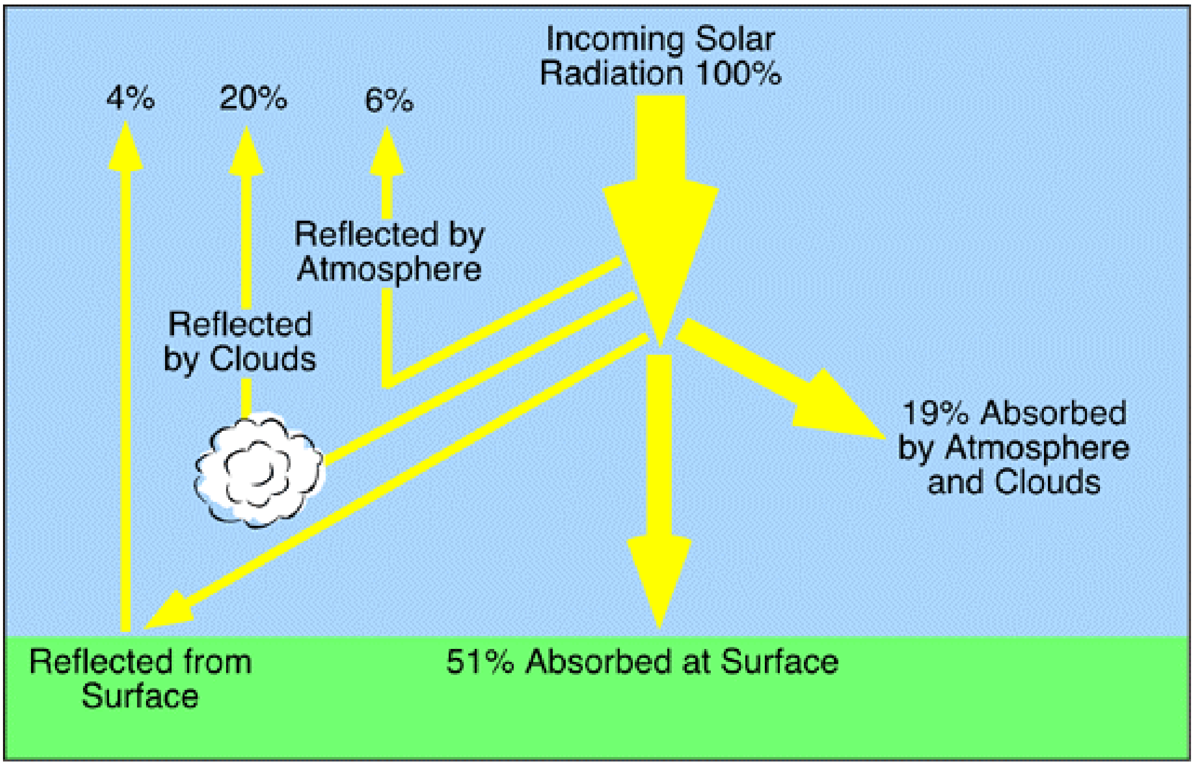

Fig. 4.4. Global modification of incoming solar radiation by atmospheric and surface processes.

Gradients in the surface albedo determine horizontal gradients in the absorbed solar energy, engendering *hot spots* where the albedo has local minima. As described in Chapter 3, when the ground is sufficiently *energetic*, air parcels above the hot spots become more buoyant than the surroundings and may rise through the different atmospheric layers. The contribution of the latent heat, released to the atmosphere by evaporation at the surface, is also important in activating and keeping on the up- and downdraft process. Daily cycle data of the shortwave incoming solar radiation and long-wave ground-emitted radiation provides a useful information when interpreting the UBL daily development.

Thermals rising from the surface are generally far to represent a linear system. Turbulence, naturally induced by convective motions, evolves in rings vortex of different diameters in the first few meters above the surface. The process of turbulence activation is often enhanced by wind shear and by rough terrain. Flows over uneven surfaces are characterized by a large value of the Reynolds number and a logarithmic velocity profile. Friction velocity, u_*, is a reference wind velocity defined by the relation:

$$u_* = \left|(\tau/\rho)\right|^{1/2}, \tag{4-2}$$

where τ is the *Reynolds stress* (directly proportional to ρ),and ρ is the air density. Eq. (4-2) can be rewritten also as,

$$u_* = \left[\left(\overline{u^{'}w^{'}}\right)^2 + \left(\overline{v^{'}w^{'}}\right)^2\right]^{1/4} \tag{4-3}$$

which exactly gives the relation between friction velocity and momentum flux. In this case the momentum flux is associated with turbulent velocity fluctuations ($u^{'}$ and $v^{'}$) of the mean horizontal flow in the vertical direction, where w' is the vertical component of the velocity fluctuation (Fernald, 1984). Eq. (4-3) is usually applied to motion near the ground where the shearing stress is often assumed to be independent of height and approximately proportional to the square of the mean velocity. The friction velocity is, therefore, exactly the velocity for which this square law would be valid. From eq. (4-2), a measure of the friction velocity is also a measure of the surface stress τ. In fact, surface stress is the momentum flux through the air-ground interface and its interpretation is the vertical transfer of horizontal momentum, per unit area. Stress is approximately constant with height near the surface; unlike wind speed there is no need to specify a reference height. Following Ting and Hay (1973), in free convection conditions near the ground, the friction velocity, u_*, and the heat flux, H, are related through the equation:

$$\overline{u} = 3Cu_*^2\left(Hgz/\rho c_p T_0\right)^{-\frac{1}{3}} \tag{4-4}$$

where ρ, c_p, g, C and T_0 are, respectively, density, specific heat, gravitational acceleration, a numerical constant and reference temperature and $\overline{u}$ is the wind speed. Ting and Hay showed measured values of H and u_*, confirming a direct proportionality between the two variables. In this study a full daily cycle of measured u_* values is related with the UBL daily development, specially for the convective case. The UBL growth in the hours after sunrise is actually connected to the increase in the heat flux at the ground and vice versa after sunset.

Two other variables provide information about the thermodynamic status of the atmosphere and can be related to the UBL temporal evolution, the *air temperature* and the *absolute humidity*. The temperature of the air measured near the surface is an indicator of the amount of heat at that level. High temperatures generally denote a deep BL. The absolute humidity or *vapour density* in a system of moist air, like the troposphere is, represents the ratio of the mass of water vapour present to the volume occupied by the mixture; that is, the density of the water vapour component. Thermals dynamics and formation have been discussed in Chapter 3; more buoyant air rises above humid surfaces reaching higher levels in the convective BL. In the while, evaporation increases the absolute humidity rate near the ground surface.

4.2.2. Convective and non-convective UBL development

From October 2001 till September 2002 the lidar operated measurements almost uninterruptedly. The lidar selected data presented in this Section are time series with duration of 24 hours (i.e., one daily cycle) of range corrected lidar signal, *RCS* (see Eq. (1-25)). The altitude gradient of *RCS* logarithm, *GS*, has the same expression as in Eq. (1-26) for altitudes $h > 180$ m, i.e., for $O(h) \equiv 1$. Data obtained with the BUBBLE lidar were more affected by solar background, electronic and shot noise compared to data obtained with the lidar used for studies in Chapter 2 and 3. The variance method is particularly sensitive to shot noise on the single profiles, more than the *GS* method. Then, for this study, only *GS* method was used to retrieve the UBLH from lidar data (Martucci et al., 2003; Martucci et al., 2004).

At the start of this chapter I wrote about two case studies of UBL daily cycles above the city of Basel, two different cases representing a summer and a winter UBL. In Chapter 3 are presented ten cases of BL temporal evolution over one-hour-and-a-half of measurement: five summer (convective) days and five winter (stable) nights. Differences between convective and stable BLs were found in the mean depth and in the spectra of frequency of the top fluctuation.

For the summer case described in the next section, I expect to observe the dynamics of thermal up- and downdraft discussed in Chapter 3. Convection cannot be totally avoided during winter days. In clear sky condition, the incoming solar radiation impinging onto the earth's surface, determines vertical mixing in the few hundred meters above the ground. The sensible heat flux is strongly reduced by the smoothed temperature gradient between air and surface and only small thermals can rise from the ground. When fog or clouds decrease the incoming solar radiation at the surface, the vertical mixing becomes a negligible process as much as the upward sensible heat flux. It is then expected that during winter the UBLH temporal evolution will not show sharp growth and decay, but rather an even UBL top temporal evolution through day and night.

An outline of two ideal daily developments is sketched in Fig. 4.5, in panel (a) and (b).

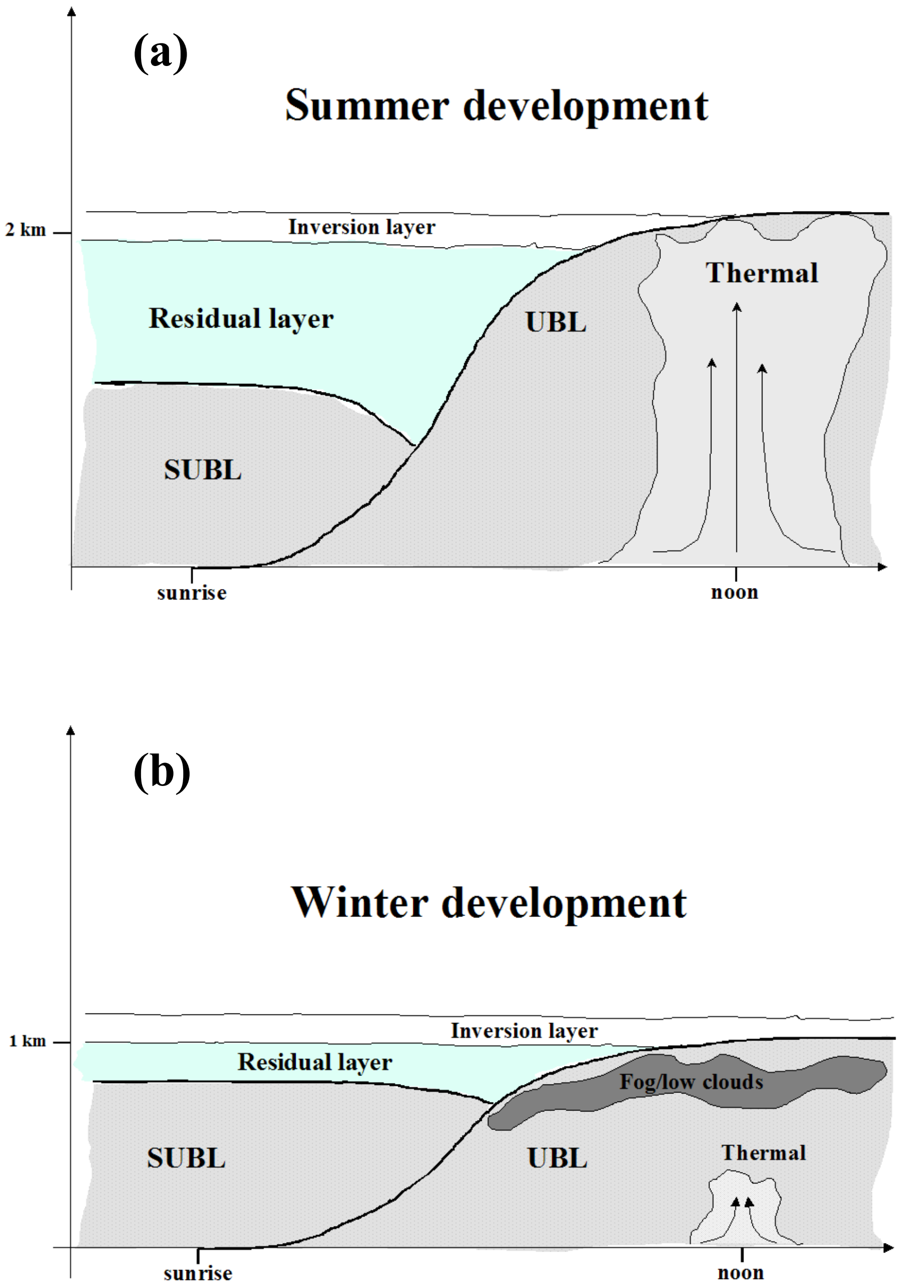

Fig. 4.5. BL daily cycle for a summer case, in panel (a), and a for a winter case, in panel (b). UBL growth in panel (a) is sharp during the first hours after the sunrise and generally erodes the capping inversion by convective processes at its top during the central hours of the day. The difference between the UBL and the stable UBL (SUBL) tops is large. In panel (b), the BL daily evolution is smooth due to low temperatures during both day and night. The nocturnal residual layer is shrunk compared to the summer case. In case of fog or low clouds the diurnal UBL is affected by very little convection restricted to the few meters above the ground.

4.2.3. *Lidar observations*

In Fig. 4.6 and in Fig. 4.7 the *RCS* time series show the daily cycle of the first 3 km of atmosphere above the ground level (a.g.l.). Measurements were performed at the Spalenring-Basel station (site Ue2 in Fig. 4.3). Both *RCS* time series are time-altitude cross sections, with superimposed the UBLH temporal evolution (black line). Time resolution of the computed UBLH line and *RCS* time series is, respectively, 30 minutes and about 1.5 minutes. Vertical resolution of *RCS* data is 40 m.

In both cases the BL *RCS*-development fits quite well the ideal cases shown in Fig. 4.5. The summer case shows a sharp UBL growth starting after the local sunrise up to a maximum altitude attained during the central hours of the day with consequent enhancing of the backscatter signal value. After sunset convection breaks down and the level of air mixing rapidly decays.

The winter case BL smoothly evolves over time. The difference between the UBL and the stable UBL (SUBL) tops is now reduced to 500 m when was about 1.8 km for the summer case. Also the Residual layer is more shallow than the summer one.

4.2.3.1 Summer case: 5th of July 2002

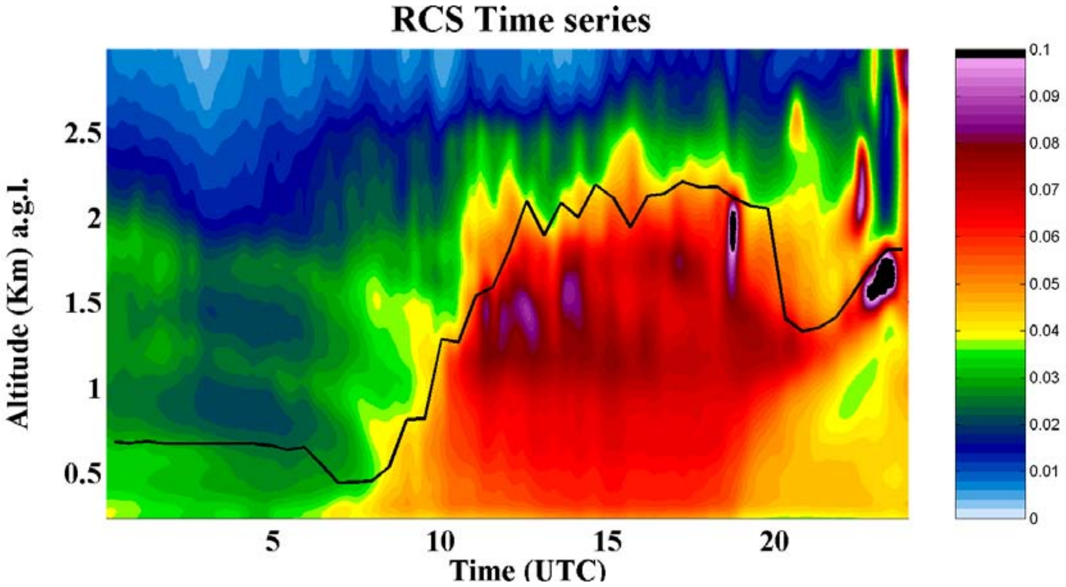

Fig. 4.6. *RCS* time series; start of measurements at 0000 UTC, end at 2359 UTC. The black line represents the computed UBLH temporal evolution computed using *GS* method. Red and dark-red colours indicate a large backscatter signal value, blue is for low backscatter and for free troposphere. Time resolution of the computed UBLH line and *RCS* time series is, respectively, 30 minutes and about 1.5 minutes. Vertical resolution of *RCS* data is 40 m.

4.2.3.2 Winter case: 15th of December 2001

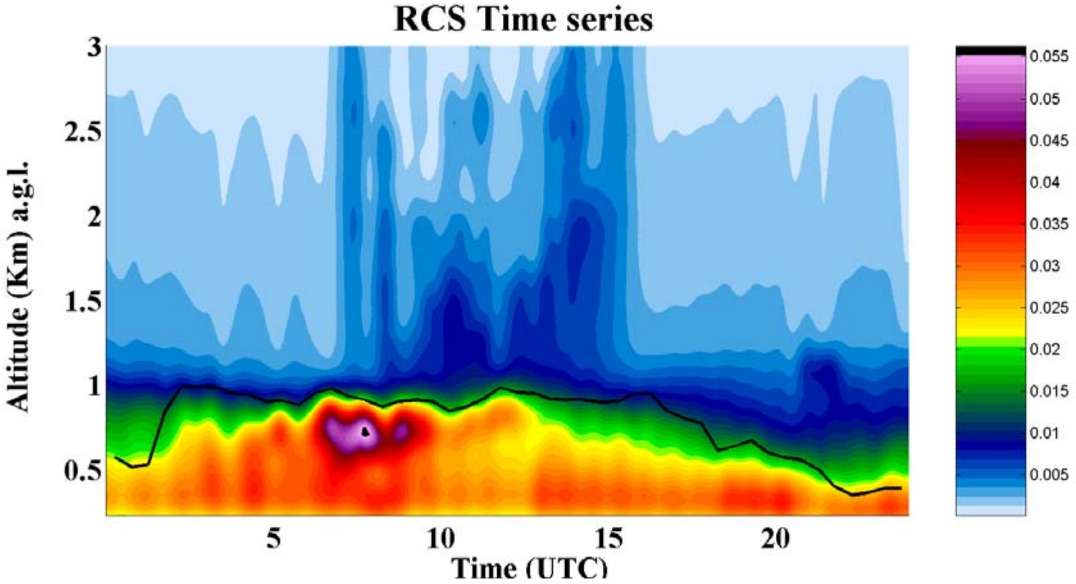

Fig. 4.7. *RCS* time series; start at 0000 UTC, end at 2359 UTC. The black line shows the computed UBLH temporal evolution computed using *GS* method. Red and violet colours indicate a large backscatter signal value, blue is for low backscatter and for free troposphere. Time resolution of the computed UBLH line and *RCS* time series is, respectively, 30 minutes and about 1.5 minutes. Vertical resolution of *RCS* data is 40 m. Between 0600 and 1000 UTC an elevated layer of fog (~800 m) covered Basel (violet spot). After 1100 UTC followed a typical winter UBLH development

4.2.4. Meteorological observations and discussion

In Fig. 4.8a-c and Fig. 4.9a-c are shown the temporal evolutions of the *in situ* measurements of the meteorological variables. All the variables were measured at the permanent station at Spalenring above the roof level of the Institute of Meteorology, Climatology and Remote Sensing. Sensor measuring variables were installed on a tower reaching from street level up to about 2 times the mean building height z_H (i.e., in the *roughness sublayer*). The precise surface characteristic are $z_H = 12.5$ m, altitude a.s.l. equal to 278 m and a surface shortwave albedo of 11.2 %.

The two cases are presented as *extreme cases* with respect to the extremely different meteorological conditions characterizing the summer and winter daily cycles. In particular, in panel (a) of Fig. 4.8 and Fig. 4.9, the air temperature evolution over the 24 hours (time resolution is 10 minutes), shows large differences between the two cases. The maximum temperature value achieved during the 15th of December 2001 was –5.53ºC (at 1700 UTC), conversely, for the summer case was 23.46ºC (at 1750 UTC).

4.2.4.1 Summer case

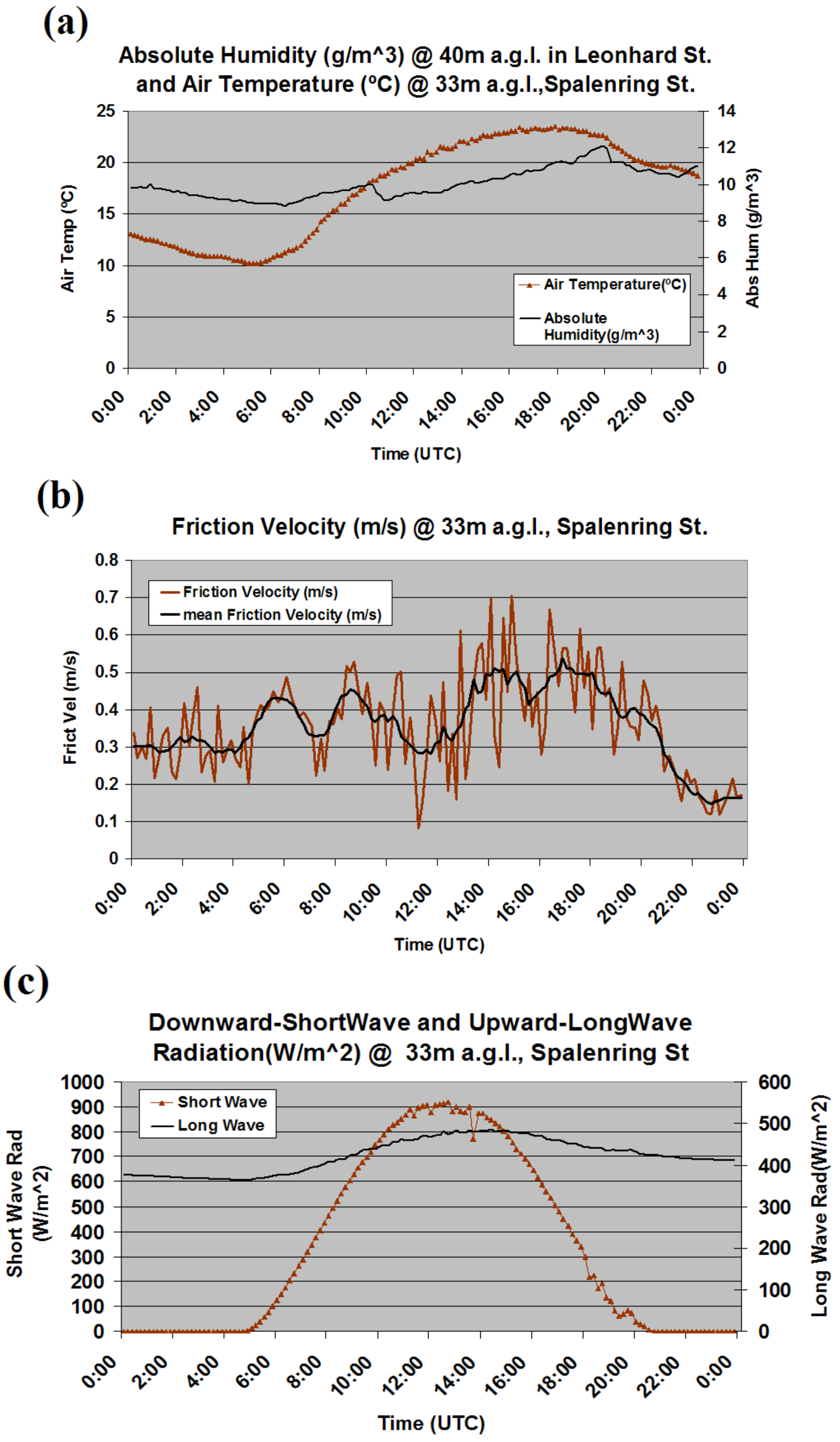

Fig.4.8. (a) The red curve is the air temperature, the black line is the abs. hum. The peak of temperature coincides in time with the UBL top maximum in Fig. 4.6. (b) Mean value of u_*, is significantly higher when convection is supposed to be stronger (1200-1900 UTC). (c) Short (red) and long (black) radiation, respectively, absorbed and reemitted by the surface. Because of radiative cooling the long radiation value gently decreases during night. Actually its value is higher during 2200-2400 than in 0000-0400 UTC.

Absolute humidity correlates with the atmospheric aerosol backscatter (Dupont et al., 1994). The humidity sensor was installed on the meteorological tower station at the height of 38 m a.g.l., *in situ* values depicted in panel (a) of Fig. 4.8 represent the daily cycle of the air parcels advected past the sensor. Absolute humidity clearly shows a positive trend between 1000 and 1900 UTC. During afternoon, air becomes more moist near the surface due to evaporation from trees and grass around the tower. The main increase in absolute humidity during afternoon is nevertheless due to advected humidity from rural area around the city. Actually, Basel, as an urban heat island, represents on the mesoscale a centre of air-convergence during the central hours of the day. In this time interval, air from the surroundings converges toward the city. In the same plot, the temperature time-evolution follows the profile of an ideal summer daily cycle, as it is expected for a clear sky, warm day. Correlations between temperature and BL temporal evolution in Fig. 4.6 are easily detected. The maximum of temperature coincides in time with the maximum of UBL top, both around 1800 UTC.

In panel (b), the average value of the friction velocity (black line) is fairly stable in the first hours after midnight and up to about 0430 UTC. Two local maxima are present around 0600 and 0900 UTC. In the early morning the heat flux is still not enough large to induce a so sharp increase in u_*. An interpretation of this increased value is the turbulent effect that a morning wind may have flowing over the buildings surface. Friction velocity then increases during the convective hours between 1200 and 1800 UTC as it is expected following theory in Section 4.2. After sunset, turbulence rapidly decays matching the drop of the UBLH in Fig. 4.6. Because of the reduced value of u_* during the first hours of the night, it is expected a well stratified atmosphere within the SUBL.

In panel (c) are shown the daily developments of the shortwave incoming solar radiation (red) and the longwave ground-emitted radiation (black). On 5th of July 2002 the sunrise and sunset were, respectively, at 0438 UTC and 2029 UTC. This is shown also by the rough increase in shortwave energy impinging onto the sensor starting from 0430 and by the drop to zero around 2030 UTC. The longwave emission has a maximum during day when the ground is absorbing the incoming shortwave radiation, but affects the BL dynamics specially during night. At night, the upper levels of the Earth cool through long-wave radiation to space (this effect is much stronger under clear skies, as clouds give an enhanced greenhouse effect, acting to reduce the cooling). Air slightly higher in the BL also cools by radiation and by conduction downwards. Since the low levels become very cold, a very stable layer develops near the surface (the SUBL), often with temperature increasing with height. Longwave upward emission decreases during night as the surface continues to cool.

4.2.4.2 *Winter case*

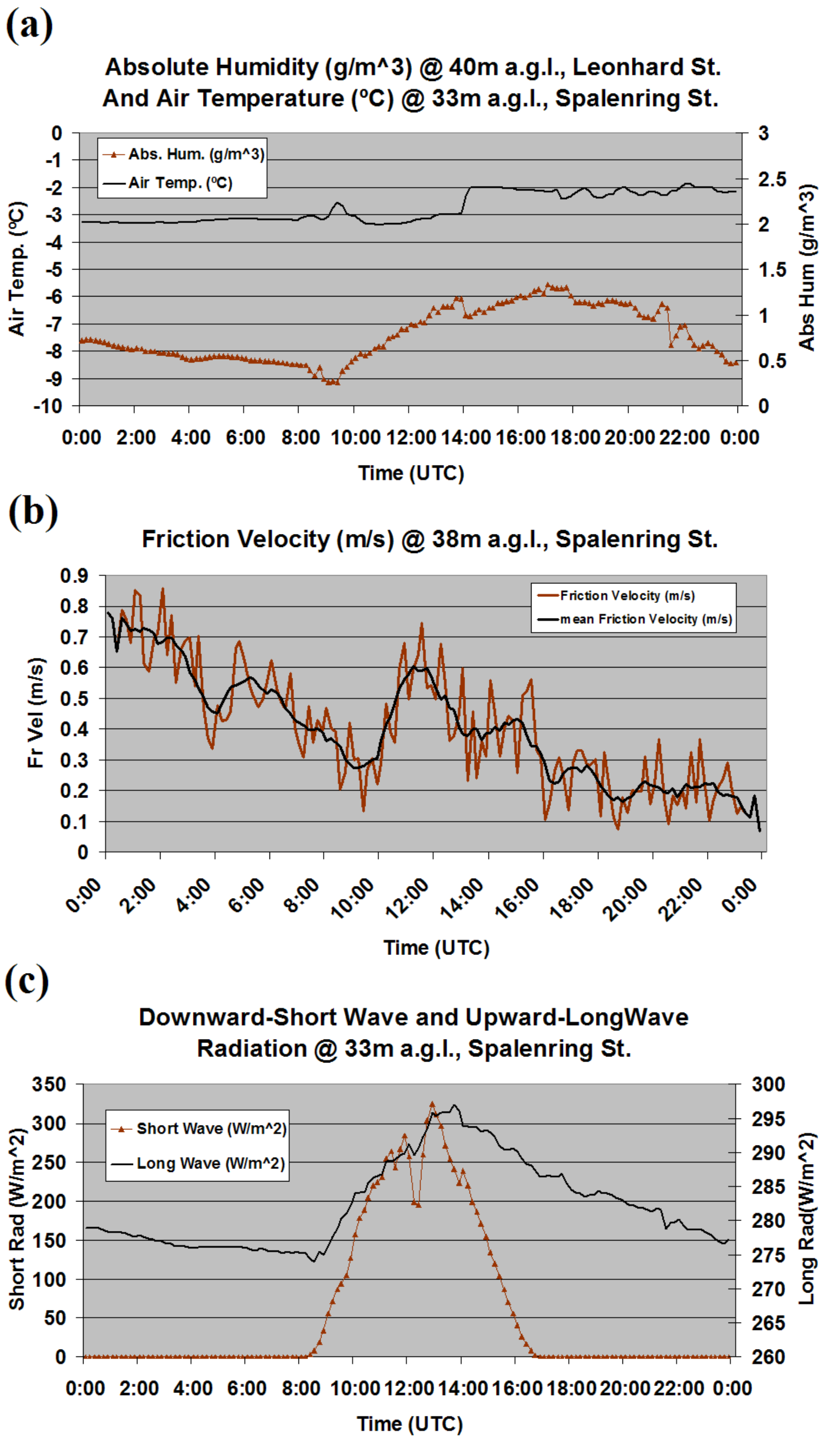

Fig.4.9. Lines symbols as in Fig.4.8. Panel (a): an elevated layer of fog overlaying the station is shown by the little step of absolute humidity between 0600 and 1000 UTC. When the layer of fog lowered, just before to dissolve, absolute humidity and air temperature had, respectively, a positive and negative peak. Air temperature, never rose more than -5ºC. (b) After fog dissolved friction velocity kept a normal development with increasing values during the central hours. (c) Depletion in short radiation contribution at around 1200 UTC is due to a cloud cover.

In Fig. 4.9, in the *RCS* time series, at about 800 m a.g.l. appears an elevated layer of high backscatter probably due to fog or to a thin scattered cloud-cover overlaying Basel between 0600 and 1000 UTC. Up to about 0800 UTC, the absolute humidity, in panel (a), remains almost constant. This suggests that the humidity sensor was not dipped in the humid layer and then that the fog layer was not touching the ground. From 0900 to 0930 UTC the layer considerably lowered and this is shown by the sudden increase in absolute humidity content. There is, in fact, an increase equal to the 10 % of its value, i.e. from 2 to 2.2 g m^{-3} in 30 min. Correspondingly, air temperature decreased of the 7 % of its vale during the same lapse of time. The temporal evolution of the temperature during this extremely cold day has a maximum value of –5.5ºC at 1700 UTC and a minimum of –9.2ºC at 0930 UTC.

Friction velocity, in panel (b), is decreasing in average (black line) during the first hours of the day up to a local minimum coinciding with the temperature minimum at 0930 UTC. Nocturnal turbulence was likely due to the northerly wind blowing over Basel from all the previous days and gradually decaying in the same time interval, from 0000 to 0930 UTC. In general, enhanced urban turbulence at night is observed during both winter and summer cases. Balling and Cerveny (1987) noticed an increase in wind speed over the city at night. They suggested that this effect was due to local urban horizontal temperature gradients and enhanced vertical mixing with the faster flow aloft. After 1030 UTC the sky was almost clear and the UBLH increased until 1200 UTC remaining almost constant up to 1700 UTC. In the same lapse of time, the temperature and the friction velocity reached also a maximum value.

After sunset occurred, at 1638 UTC, temperature of the air began to fall again because of radiative cooling. As for the summer case the longwave emission, in panel (c), diminishes in value during the night accordingly to the temperature.

4.3. Statistic of boundary-layer height

Table 4.1 shows the mean values obtained by averaging the UBLH values during 24 hours of lidar observation. The data collection contains 89 cases, each case is a full daily cycle selected among days with no precipitation (rain or snow). Data are grouped in the four seasons; winter data represent the *meteorological* winter, different from the astronomical one by about 20 days. Actually, at the latitude of Basel, where measurements were performed, the winter starts at the beginning of December when temperatures are already around zero during both day and night.

Table 4.1. Mean daily UBLH values during the BUBBLE measurement campaign from October 2001 to August 2002. Data are grouped in the four seasons: Fall (20), Winter (19), Spring (27) and summer (24) for a total of 89 cases.

Fall		**Winter**		**Spring**		**Summer**	
Date (yymmdd)	$\overline{UBLH}$ (m)	Date (yymmdd)	$\overline{UBLH}$ (m)	Date (yymmdd)	$\overline{UBLH}$ (m)	Date (yymmdd)	$\overline{UBLH}$ (m)
011013	480	011203	400	020326	670	020626	1500
011014	440	011210	860	020327	1070	020627	1400
011016	525	011211	530	020328	1125	020628	1020
011017	800	011214	715	020329	1080	020629	1210
011018	660	011215	790	020401	700	020630	1200
011020	570	011217	415	020402	835	020704	1000
011026	495	020207	770	020403	820	020705	1340
011027	430	020217	600	020404	790	020707	1230
011029	410	020218	720	020405	820	020708	980
011030	470	020221	500	020406	1380	020711	1100
011101	430	020303	640	020409	2170	020712	760
011103	550	020304	765	020410	1780	020727	1185
011104	630	020305	680	020411	860	020728	835
011105	560	020306	630	020418	670	020729	677
011110	470	020308	1080	020422	965	020802	1140
011114	500	020309	1130	020423	760	020805	1200
011115	440	020311	500	020425	630	020808	1210
011116	750	020312	580	020427	1150	020813	790
011117	760	020313	550	020430	1200	020814	1120
011121	460			020506	980	020815	990
				020507	545	020816	930
				020510	800	020817	960
				020513	1000	020818	980
				020530	1920	020819	1145
				020531	785		
				020601	853		
				020602	660		

The 89 cases are mean values of the temporal evolution of the UBLH calculated from the *RCS* time series using the *GS* method (as shown for the two case studies in the previous sections).

From Fig. 4.10 to Fig. 4.12 are presented, in form of data distribution, the mean UBLH values collected and shown in Table 4.1. Starting from Fig. 4.10 to Fig. 4.12 the time of average increases from a time interval of 24 hours to the entire season. In Fig. 4.10 all the data are plotted representing the mean daily UBLH values through the year, from October 2001 to August 2002. The UBLH values have been linearly fitted to highlight the increasing averaged values through the year.

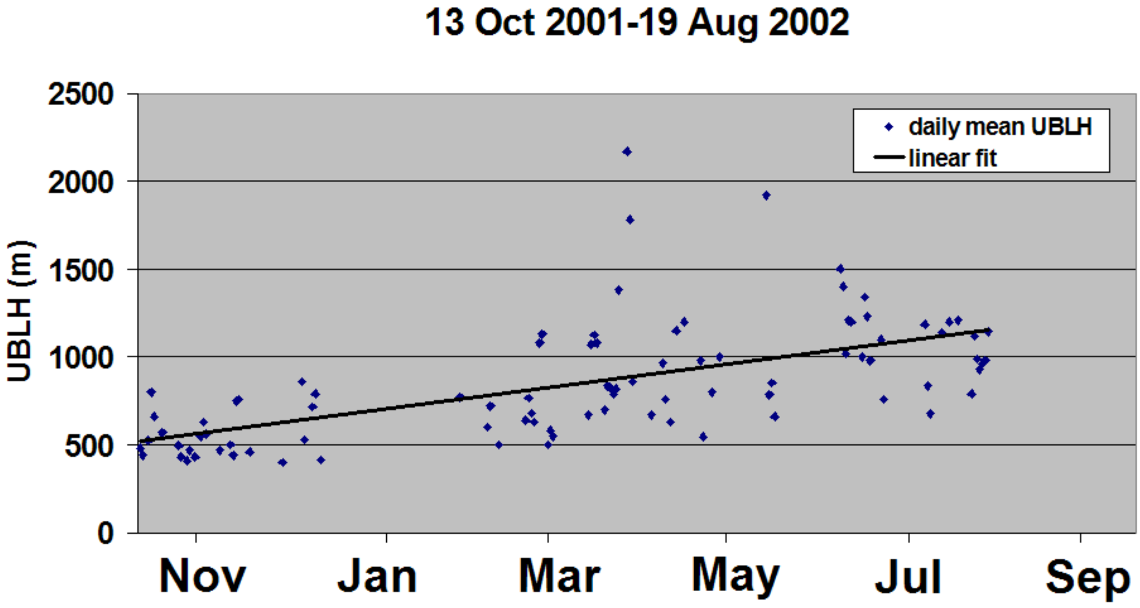

Fig. 4.10. Daily averaged UBLH values from October 2001 to August 2002. The linear fit highlight the increasing averaged values through the year.

In Fig 4.11 are depicted the four seasonal evolutions of the data shown in Table 4.1. Panel (a) shows the mean UBLH values presented in the second column of the table, i.e. the Fall cases. Panel (b) shows the mean UBLH values presented in fourth column of the table, i.e. the Winter cases. Panel (c) shows the mean UBLH values presented in the sixth column of the table, i.e. the Spring cases. Panel (d) shows the mean UBLH values presented in the eighth column of the table, i.e. the summer cases. As it could be expected, in panels (b)-(d), the UBLH values fluctuate around a mean value increasing from Winter to Summer. An unexpected result is the mean UBLH value during the Fall season. In fact, this value is the lowest through the four seasons, while Winter was expected to be the one with lowest temperature and shallowest UBLH.

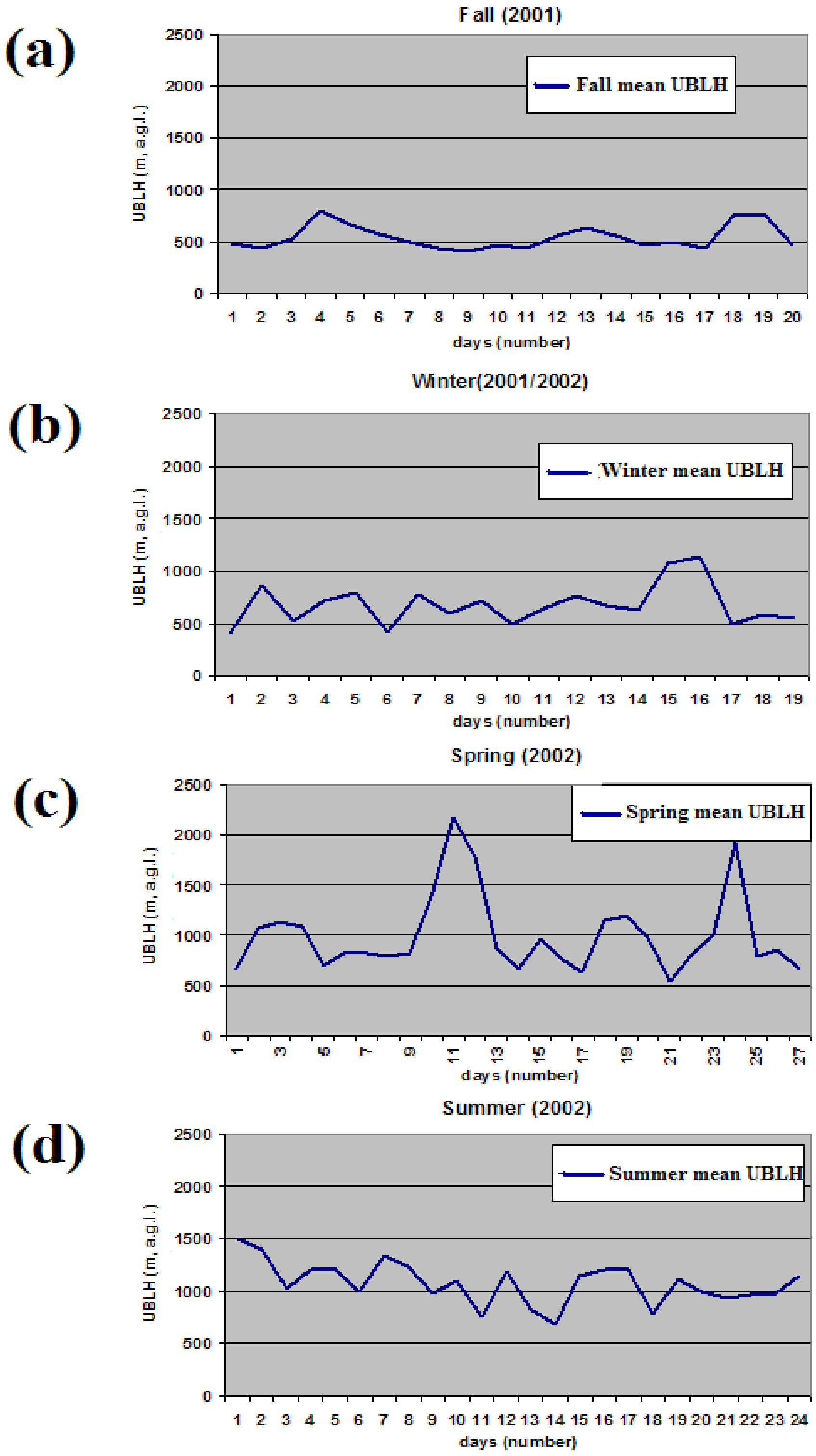

Fig. 4.10. The seasonal evolutions of the data shown in Table 4.1. Panel (a) shows the mean UBLH values collected during Fall season. Panel (b)-(c) and (d) present , respectively, the winter, spring and summer cases. The period of measurement of the selected cases goes from October 2001 to August 2002.

The reason why this happens is due to intense fog events occurring during Fall season in the few hundreds meters above the ground and often enduring through all the day. This is clear also from Fig 4.12 where the seasonal averaged values are shown, respectively, for Fall, Winter, Spring and Summer. The standard deviation of Fall data is very small compared to the others, implying a very constant UBLH value during all the season. Values of UBLH increase almost linearly through the year. Vertical error bars in Fig. 4.12 provide the amplitude of the error committed computing the UBLH value averaged over the entire season. The half-amplitude of the errors bars (i.e., the absolute value of the standard deviation ±σ) ranges between 17 % for Fall cases up to 29 % for Spring cases. Spring error is the largest among the four, this is reasonable because, in general, Spring has the largest temperature variations compared to the other seasons.

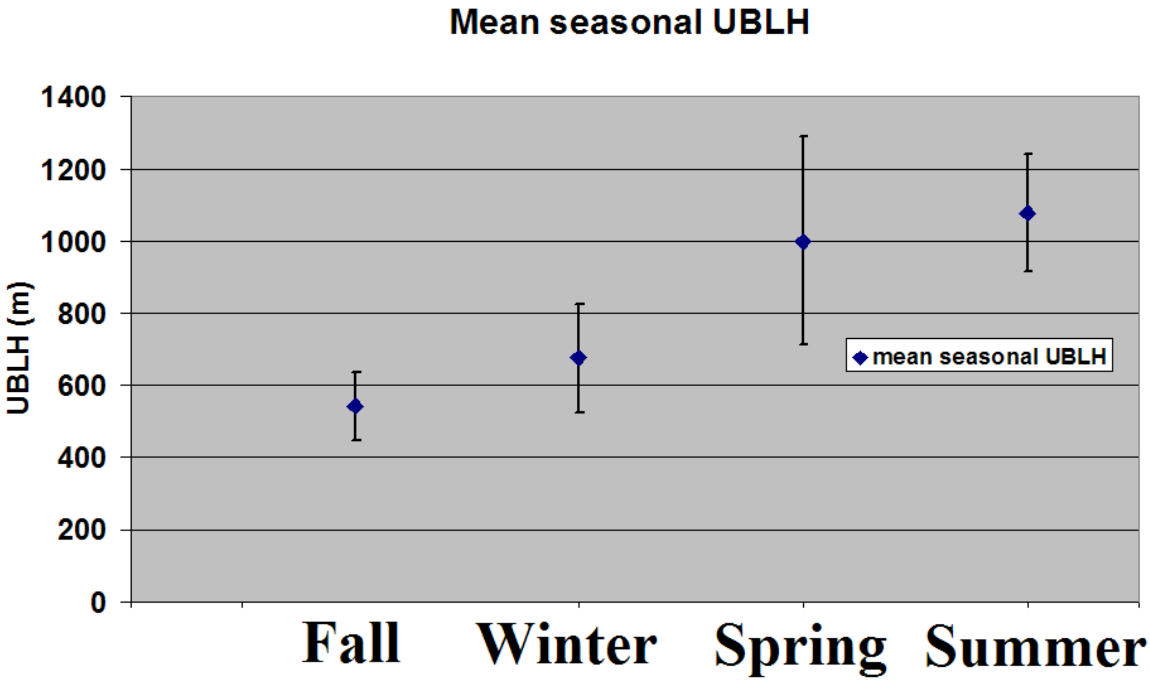

Fig. 4.12. The seasonal average values are shown for Fall, Winter, Spring and Summer. Values increase almost linearly through the year. Vertical error bars half amplitude is for Fall, Winter, Spring and Summer, respectively, 95 m, 150 m, 286 m and 162 m.

Each single UBLH value in Table 4.1 represents an average over the diurnal and nocturnal UBLH values. During Fall and Winter, as mentioned before, the first hours of the day between midnight and 1000 UTC are often characterized by the presence of fog in the few hundreds meters above the city. When lidar probes the layer of fog, the signal rapidly extinguishes depending on the optical thickness of the layer. When the layer is particularly (optically) thick, the laser cannot achieve the higher atmospheric levels. When the fog layer is at the top of UBL it does not modify the measure of the UBLH. On the other hand, when the layer forms at a level somewhere in the middle of the UBL, the lidar estimation of the UBLH is practically halved. Finally, when fog is present inside the UBL the lidar measurement results in a very thin nocturnal and morning UBL. Averaging over the 24 hours, the resulting mean UBLH value is lower than what it could be expected if the laser was not extinguished by the fog layer. Fall, Winter (and partially Spring) data have then to be interpreted taking in account this aspect.

4.4. Conclusion

The first part of this study shows that the information about UBL dynamics derived from lidar backscatter signal is in good agreement with that arising from daily development of selected meteorological in situ measurements. The comparison between lidar and meteorological measurements for two case studies (a summer and a winter case), suggests that enlarging the dataset and processing the data collected during one year of measurements can provide optimal information about the diurnal and nocturnal status of the BL above Basel. This study also aims to be a breach in the investigation and monitoring of the UBL proposing the remote controlled lidar with the automatic data transfer as ideal for the description and analysis of the UBL dynamics.

The second part of the chapter focuses on the lidar observation of the UBL during long, continuous period. The accumulated data provided a statistic of UBL height values as retrieved from one-year of lidar operation. In fact, a large dataset allows to employ data as a source of statistical information also for future atmospheric studies. Models need climatology to forecast the development of one or several atmospheric variables. Measuring these variables a lidar continuously operating provides the inputs for model assessments. The observation of UBL dynamics also contribute to evaluate the amount of pollutants aloft in the urban atmospheric layers and sub-layers (i.e. particulate matter as PM10 and PM2.5). Also for this reason, the monitoring of the UBL becomes more and more important for present and future environmental studies.

The international COST 715 program (final reports: Piringer and Joffre, 2005; Fisher et al., 2005) that promoted BUBBLE, in which the elastic backscatter lidar was involved, has primary relevance with respect to the experimental state-of-the-art in Europe, actually no other projects before succeeded in so long period of measurements in urban sites. The conclusion from this chapter is that the backscatter lidar is a practical instrument to carry out long-term observations of the height of the BL top in urban conditions. This result opens the possibility to include the UBLH in the atmospheric pollution model studies in a routine basis.

Chapter 5

Cloud detection with airborne lidar in the upper troposphere and lower stratosphere.

This chapter presents measurements of backscatter and depolarization ratio of upper tropospheric and lower stratospheric clouds. Data were collected during four field campaigns held in polar and tropical regions. The investigation of the upper troposphere and lower stratosphere was realized by two automated backscatter-depolarization lidars. The lidars were installed on the high-altitude research aircraft Myasishchev M55 'Geophysica' (Russia). From 2003 to 2005 the miniature aerosol backscatter lidars, MAL1 and MAL2, participated in total of four campaigns with this research aircraft. The polar campaigns were in the frame of the EC campaign EUPLEX in Kiruna (Sweden) in January-February 2003 and the ENVISAT validation campaign also in Kiruna in February-March 2003. The tropical campaigns were TROCCINOX and SCOUT-O3 held, respectively, in January-February 2005 in Araçatuba (Brazil) and in November-December 2005 in Darwin (Australia).

Motivations of the study

The processes of ozone depletion and transport of chemicals from tropical to polar latitudes take place in the upper troposphere and lower stratosphere (UTLS). Here, I provide a brief description of this atmospheric region with an outline showing the clouds and the mechanisms of transport playing a key-role in the ozone balance.

The UTLS is a highly coupled region: dynamics, chemistry, microphysics and radiation are fundamentally interconnected. Water vapour and ozone, perhaps the two most important greenhouse gases in the UTLS, are controlled by both transport processes, such as stratosphere-troposphere exchange, and chemical processes including multiphase chemistry, and cloud microphysics, which in turn are influenced by the temperature and aerosol distributions.

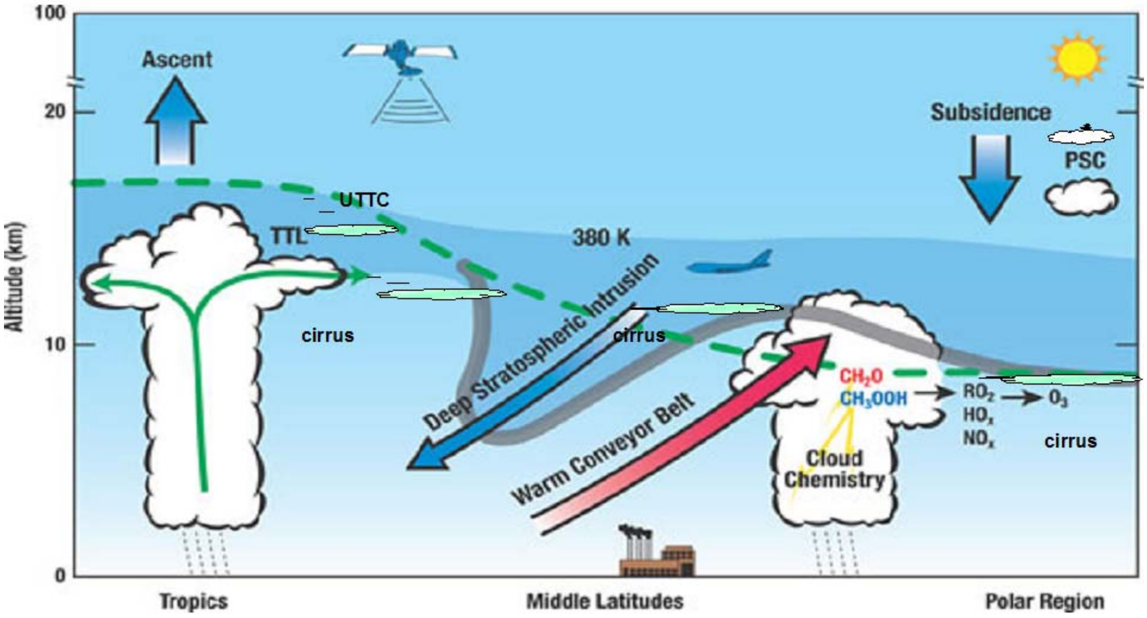

Figure: Synopsis of principal processes coupling dynamics, chemistry and cloud microphysics in the UTLS region at different latitudes.

This schematic figure (adapted from Stohl et al. 2003) highlights the important processes coupling dynamics, chemistry and cloud microphysics in the UTLS. The dashed green line denotes the time-averaged tropopause. In the tropics, maximum outflow from deep convection occurs near ~12-16 km, while the cold point tropopause occurs near 17 km. The intervening region has characteristics intermediate between the troposphere and stratosphere, and is termed the tropical transition layer (TTL). Extratropical stratosphere-troposphere exchange occurs in tropopause folds and intrusions linked with synoptic weather systems; these events transport stratospheric ozone into the troposphere. In addition, strong convections in the tropics (shown by the so called anvil) bring near-surface pollutants (from biomass burning or anthropogenic emissions) into the upper troposphere, strongly influencing global-scale chemistry. Especially two kinds of clouds play a critical role in the process of ozone depletion within the polar stratosphere. The polar stratospheric clouds (PSCs) are high-altitude clouds on which surfaces occurs a chemical reaction directly involved in the destruction of the ozone during the polar Spring (WMO, 1999). The ultra-thin tropical cirrus are the *evidence* that water vapour (and CFCs also) are injected by deep convective processes in the tropical lower stratosphere (Corti et al., 2006). The presence of these clouds indicates the possibility for the transport of chemicals towards the polar latitudes where CFCs can deplete the ozone layer.

The motivation of this study is to prove that the backscatter lidar is the proper and, presently, the only (together with the one installed on ER-2) airborne remote sensing instrument, able to detect the exact position and extent of the PSCs in the polar UTLS as well as those of the ultra-thin tropical tropopause clouds in the tropical UTLS.

Background

As soon as the sun disappears behind the horizon for several months in late autumn, an intensive westerly flow of air forms around the pole which is called the polar vortex. This polar vortex forms an annular stream of air obstructing the exchange of air with the rest of the atmosphere. This is the reason why the stratospheric temperatures in this area can drop so much. The polar vortex is especially well-defined in Antarctica because of the great mass of land around the South Pole. The vortex over the Arctic and the processes connected are in general not so well defined. Polar stratospheric clouds, also known as *nacreous clouds*, are clouds in the winter polar stratosphere at altitudes between 15 and 30 km. They are implicated in the formation of ozone holes. The stratosphere is very dry and clouds, as commonly seen in the troposphere, rarely form. In the extreme cold of the polar winter, PSCs of different types may form, which are classified according to their physical state and chemical composition.

i. Type I clouds contain nitric and water

ii. Type Ia clouds consist of crystals formed from nitric and water

iii. Type Ib cloud droplets additionally contain sulfuric acid and are present in the form of supercooled ternary solution.

iv. Type II clouds consist of water ice only.

PSCs form at very low temperatures (below -78°C). These temperatures occur in the lower stratosphere inside the polar vortex. In the Antarctic, temperatures below -88°C frequently cause PSCs type II. Such low temperatures are rarer in the Arctic. In the Northern hemisphere, PSCs also form in the cold lee of mountain barriers such as the Scandinavian mountain ridge or Greenland and are frequently observed, e.g. by lidars. Recently, single cloud events (liquid and solid) have been characterized by balloon-borne measurements for microphysical properties and composition (Schreiner et al., 1999; Voigt et al., 2000).

In PSCs of type I PSC particles with sufficient mass will sediment out, removing the nitric acid (HNO3) contained within them and thus denitrifying the air masses. The process of dehydration occurs principally for PSCs II, but also in the case of first type. Active chlorine inside the polar vortex causes the chemical ozone loss. Under normal conditions the chloride coming from FCCH set free by man, is bound in the so-called chloride reservoirs. These are chemicals which contain chloride atoms but do not contribute to ozone decomposition. The most important chloride reservoirs are chloric acid (HCI) and chloride nitrate (ClONO2). According to nowadays knowledge, the ozone hole forms because under the special conditions of the polar areas in winter chloride is set free from the reservoirs. The chemical reactions happening on the surfaces of the ice crystal s of the clouds are very different from those in the air. Here the two reservoir substances chloric acid and chloride nitrate can react with each other and set free chloride atoms and nitric acid. In winter, the chloride molecules stay in the air without any modification and still do not contribute to ozone decomposition. The nitric acid is bound in the ice crystals of the clouds and that way forms the Nitric Acid Trihydrate clouds (NAT) clouds described above.

As long as the chloride exists as molecules, there is no ozone decomposition. But as soon as the sun rises in the arctic spring, the chloride molecules are dissociated by the ultraviolet radiation (Lambda less than 450 nm), that means that they are split up into chloride atoms of great reactivity. This sets free large amounts of chloride atoms within a short time and starts an avalanche-like decomposition of ozone which finally leads to the formation of the ozone hole. In fact, the chlorine activation may be identified as a large chloric acid reduction in the lower stratosphere during the polar winter with respect to normal values. The inactive chlorine reservoir species are converted into active, ozone destroying, form by heterogeneous reactions on the PSCs surface (Tilmes et al., 2004).

The polar campaign EUPLEX (EUropean Polar stratospheric clouds and Lee waves Experiment), occurred in Kiruna (Sweden) between January and February 2003, addressed some key questions of Arctic stratospheric ozone depletion that are not yet answered to a satisfactory extent: how do PSCs form and are observed PSC growth and properties (in both synoptically cold regions and in regions of lee-wave activity) in accord with microphysical theory? How the observed denitrification and dehydration processes can be explained? What is the relative importance of synoptic and lee-wave PSCs for chlorine activation and Arctic ozone loss? EUPLEX also investigates the formation and evaporation processes of lee wave clouds by measuring in the upwind region, within the cloud and in its tail downwind.

Two backscatter airborne lidars developed at the Observatory of Neuchâtel were deployed for measurement in the frame of the EUPLEX project with principal objectives the study of the polar stratospheric clouds (PSCs) and their role in the ozone depletion. Backscatter lidars installed on the high-altitude research aircraft can determine backscatter and depolarization ratios of thin clouds above and below the aircraft. In-situ instruments, installed on the aircraft, measure the chemical composition and the thermodynamic status of the atmosphere. Chemical and thermodynamic measurements can be related to the aerosol and cloud backscatter profiles of the probed air-volumes close to the aircraft.

During the second part of the Arctic campaign in Kiruna (February-March 2003), instruments on the aircraft were deployed for the validation of the ENVISAT satellite (http://envisat.esa.int/). The detection of cloud and aerosol layer is one target of the numerous ENVISAT measurements. A reason for the attention to cloud measurements in ENVISAT validation program is that the cloud top limits the measurements of trace gases by limb-scanning instruments. In this respect, the determination of cloud top altitude and in particular for sub-visible clouds is critical for the data evaluation of the limb-scanning sensors installed on a high-altitude aircraft.

This determines the interest for ENVISAT validation in lidar measurements of the cloud top altitude and of the backscatter ratio for sub-visible clouds. Measurements of earth surface and atmosphere were the objective for lidar operations on the M55 aircraft (Matthey et al., 2004).

In 2005, from January to February, the **TRO**pical **C**onvection, **CI**rrus and **N**itrogen **OX**ides (TROCCINOX) experiment was held in Araçatuba, Brazil. The composition of the atmosphere, the stratospheric ozone layer, and the state of the global climate depend crucially on processes in the tropical regions, in particular at the tropical tropopause. The research project TROCCINOX investigates the impact of tropical deep convection on the distribution and the sources of trace gases, cloud and aerosol particles focusing on processes in the UTLS.

One objective of TROCCINOX campaign in which lidar operations are not directly involved is:

- to improve the knowledge about lightning-produced NO_x (LNO_x) in tropical thunderstorms by quantifying the produced amounts, by comparing it to other major sources of NO_x and by assessing its global impact.

The other objective of TROCCINOX is the one for which lidar instrument has a key role:

- to improve the current knowledge on the occurrence of other trace gases (including water vapour) and particles (ice crystal and aerosols) in the upper troposphere and lower stratosphere in connection with tropical deep convection as well as large scale upwelling motions.

The fourth field campaign described in this chapter is the "Stratospheric-Climate Links with Emphasis on the Upper Troposphere and Lower Stratosphere" (SCOUT-O3) campaign, held in Darwin, Australia, from November to December 2005. As a third step of a detailed survey on the causes of ozone depletion in polar regions, SCOUT-O3, as TROCCINOX, tries to set out the origin of transport of chemicals from tropical regions. Tropics are one of the most important regions in this regard. One way the air enters the stratosphere is likely to be through transport in massive tropical thunderstorm which are prominent over Indonesia, Micronesia and northern territories of Australia. The chemical composition of the air entering the stratosphere depends on how quickly it travels from the ground and on the temperatures along the way. Changes in emission of chemicals at the ground or in how quickly they are carried aloft could cause the chemistry of the stratosphere and ozone itself to change.

The aim of SCOUT-O3 campaign is to observe how water and chemical species are lifted by strong storms and to understand how they can reach the stratosphere in this way. One particular storm system that has been studied in detail is called *Hector* and occurs practically daily during November and December in the region where the campaign was held.

Cloud targets for lidar observations during both TROCCINOX and SCOUT-O3 tropical campaigns are: the ultra-thin tropical tropopause cirrus (UTTCs) and cirrus clouds as well as the aerosol layers appearing above the top of continental tropical convection.

This chapter provides an overview of the obtained lidar results in terms of lidar backscatter and depolarization ratio during some selected flight survey through the four field campaigns. The aim is as well to empirically test how the temporal and vertical resolutions may affect the lidar backscatter signal and which is the natural limit for a fine atmospheric feature to be discriminated from the signal noise.

5.1. Airborne instruments and lidar equations in the UTLS

In many interesting cases the PSCs, the UTTCs and the elevated convective anvils appear above regions without the necessary infrastructure to install measurement instruments and in particular lidars. This require organising measurement missions to such areas, where the airborne platform gives a number of advantages:

i. It may cover large and remote atmospheric regions.

ii. It gives the possibility to install on the same platform a number of measurement instruments, arranging both complementary and cross-check measurements.

On the other hand the installation of the lidar on an aircraft is always within constraints of mass, complexity and consumption, apart from the availability of the convenient aircraft. That is why such installation is still on unique occasions.

There are lower flying aircrafts equipped with lidars (Svendsen et al., 2005; Dörnbrack et al., 2002). This solution makes it possible to assess with lidars the UTLS, but does not allow to install in situ instruments measuring the same part of atmosphere. In case a lidar is installed on a stratospheric aircraft, then its measurements can be analysed with respect to the measurements retrieved from the in situ instruments (for trace gases) installed on the same platform.

There are two stratospheric aircrafts in the world, both of which are equipped with lidars and a number of in situ instruments. One is ER-2, operated by NASA (McGill et al., 2002). The other is M55 "Geophysica" (Matthey et al., 2004; Martucci et al, 2005), operated by a consortium of research institutes from Europe and from Russia. On this aircraft the Observatory of Neuchâtel installed two lidars – Miniature Aerosol Lidar Mark1 (MAL1) and Miniature aerosol lidar Mark2 (MAL2) which already participated in total of ten field campaigns in Arctic, Antarctic, Tropics and mid-latitudes regions from 1996 to 2005 (Stein et al., 1999; Borrmann et al., 2000; Matthey, 2000; Matthey et al., 2003; Peter et al., 2003; Luo et al., 2003; Calheiros et al., 2005).

5.1.1. *Airborne lidars: MAL1 and MAL2*

Instruments, MAL1 (probing upward) and MAL2 (probing downward) are described in Section 1.5.3. Fig. 5.1 presents a picture of the lidars in their pressurized vessels before installation on the aircraft. Since the lidars are in non-pressurized compartments of the aircraft, they need such vessels for environmental protection. When installed on the aircraft Myasishchev M55 'Geophysica' (in the lower panel of Fig. 5.1), shutters close the output windows of the vessels. This is necessary for protection from contamination and for eye-safety. The pilot opens the shutters when the aircraft is at a safe distance from the airport. The lidars operate automatically after switching-on. The measurements during the flight and the housekeeping parameters are stored in an embedded PC 386.

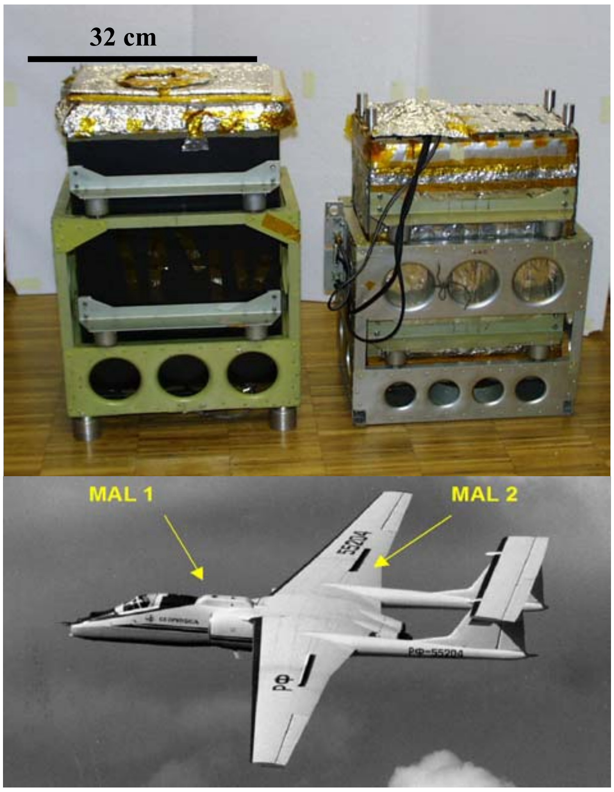

Fig. 5.1. Backscatter lidars MAL1 and MAL2 (upper panel) ready for installation on the aircraft Myasishchev M55 'Geophysica' (lower panel).

5.1.2. *Lidar equations in the UTLS*

The clouds values to be determined are directly the values of the backscatter ratio (and the depolarisation ratio) which will be defined further. The data processing algorithm for a lidar operating from an aircraft in the UTLS is different from the one used in determining the stratification in the BL. Actually, within the UTLS, the atmospheric region where the M55 flies, it is possible to consider the square Beer-Lambert transmission factor T^2 to be around 1 (see terms in lidar equation, Eq. (1-25)). In the region of full overlap ($O(h) \equiv 1$), the lidar equation may be expressed by the signal $S_c(h)$, that, after corrections for the electronic and solar background noises and for laser power and range, appears as:

$$S_c(h) = C \cdot (\beta_{mol}(h) + \beta_{aer}(h)). \tag{5-1}$$

The parameters β_{mol} and β_{aer} are, respectively, the molecular and aerosol volume backscatter coefficients. The constant C contains the terms appearing in Eq. (1-28) and is then a measure of the overall optical efficiency of the lidar.

The "backscatter ratio", introduced in Eq. (1-29) has the expression:

$$BR(h) = \frac{(\beta_{mol}(h) + \beta_{aer}(h))}{\beta_{mol}(h)} \tag{5-2}$$

Combining Eq. (5-1) and Eq. (5-2) we obtain:

$$S_c(h) = C \cdot \beta_{mol} \cdot BR(h). \tag{5-3}$$

In a region of only molecular atmosphere, the backscatter ratio has value equal to 1 ($\beta_{aer} \equiv 0 \rightarrow BR \equiv 1$) and the molecular volume backscatter coefficient, β_{mol}, is given by the values of pressure and temperature (Measures, 1984, p 42) as measured by the in-situ instruments onboard the M55 aircraft. In this way, the value of C from Eq. (5-2) can be retrieved. Such procedure to calculate C is called *calibration* and it is described further in this section. Once the value of C is known, measuring the lidar signal $S_c(h)$ and the value of β_{mol} from the in-situ instruments, the backscatter ratio at any h can be obtained.

Values for the aerosol depolarisation ratio are also determined from the lidar measurements. This value indicates if the particle is spherical or not. In the first case (spherical particle) the polarisation of the backscatter light is not rotated with respect to the polarisation of the transmitted laser beam. If the particle is non-spherical, then the polarisation of the backscattered light contains component which is perpendicular to the polarisation of the transmitted beam (Browell et al. 1990; Chen et al., 2002). The use of a linearly polarised probing beam and polarisation analyser in the receiver to distinguish the spherical particles from non-spherical ones allows to say if the studied cloud particles are droplets or ice-crystals. This information is essential to discriminate the PSC from the high-altitude cirrus that may be composed by both water and ice particles.

Eq. (5-1) may be written separately for the parallel and perpendicular polarizations of the backscatter signal. Then, the depolarization ratio $DR(h)$ may be expressed in the following way,

$$DR(h) = \frac{\beta_s(h)}{\beta_s(h) + \beta_p(h)} = \frac{S_{c,s}(h)}{S_{c,s}(h) + R \cdot S_{c,p}(h)}. \tag{5-4}$$

Where subscripts p and s refer to the parallel and perpendicular polarization components of the backscatter signal, respectively. The constant R is the ratio of the quantum efficiencies of the chain "receiver-detector" for s and p polarizations, i.e., $R = \eta_s/\eta_p$. The value of R is known by the same process of calibration used to compute C. Here I explain this process: when lidar signal passes through an optically-thick cloud, I can assume that the signal is extinguished almost immediately inside the cloud. The backscatter signal on the receiver (coming from altitudes beyond the cloud) is then equal to the solar radiation at very high altitudes ($h \rightarrow \infty$). The expression in Eq. (5-3), not corrected for the solar background and for altitudes where $T^2 \neq 1$, for parallel and perpendicular components is:

$$S_{c,s}(h) = C_s \cdot \beta_{mol,s}(h) \cdot BR_s(h) \cdot T_s^{\,2}(h) + A\Delta\lambda T\theta\eta_s B_s \tag{5-5}$$

and,

$$S_{c,p}(h) = C_p \cdot \beta_{mol,p}(h) \cdot BR_p(h) \cdot T_p^{\,2}(h) + A\Delta\lambda T\theta\eta_p B_p . \tag{5-6}$$

Where A, $\Delta\lambda$, T, θ and η are, respectively, the area, the bandwidth, the transmission of the receiver, the telescope field of view and η is the quantum efficiency of PMTs. Since the square $T_{s,p}$ Beer-Lambert factor can be considered zero starting from few meters inside the cloud, the parallel and perpendicular lidar signal terms in the right-hand side of equations (5-5) and (5-6) go to zero. The remaining terms are then the incoming solar radiation, $B_{s,\,p}$, impinging onto the receiver. Solar radiation, B, above the cloud, is Rayleigh polarized; passing through the cloud, the multiple scattering makes B to be randomly polarized. Consequence of multiple scattering is that the perpendicular and the parallel components of B become equal, $B_s \equiv B_p$. Then, measuring the ratio of the perpendicular to the parallel signal, I directly obtain R,

$$\frac{S_{c,s}}{S_{c,p}} = \frac{\eta_s B_s}{\eta_p B_p} = R \tag{5-7}$$

In Fig. 5.2 is sketched an example of the conditions in which calibration is possible. The figure shows the *RCS* received by the lidar telescope from altitudes through an optically thick cloud and beyond it:

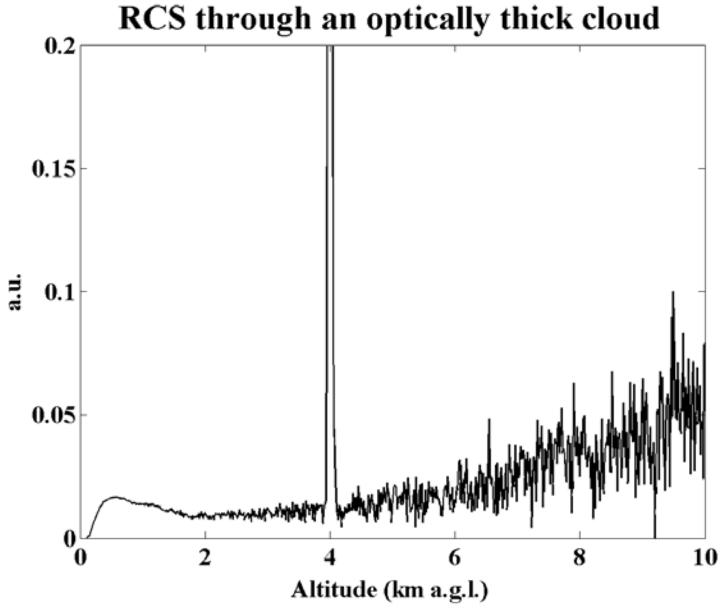

Fig. 5.2. Range corrected signal (parallel) measured during a cloud event on 1st October 2001. The region between 0 and 2 km represents the BL. The cloud at 4 km is a very (optically) thick cloud. The backscattered signal from altitudes beyond the cloud is represented only by the solar background component.

5.2. Signal processing: influence of the SNR threshold and resolution on the data information.

In this Section are introduced and explained the basis and the mechanisms of the signal processing used to present the data in the next sections of this chapter. One of the most difficult tasks, after collecting, is to process and to present the data allowing to retrieve from them the most comprehensive information. Noise components and false signal peaks represent the most complex aspect of signal interpretation when working at high resolutions. On the other hand, it is mandatory to increase the resolution (both temporal and vertical) when I want to observe very fine features as the horizontal and vertical structures of cirrus clouds on the scale of few tens of meters. The mean horizontal speed of the M55 aircraft is 200 m s^{-1}, it means that a temporal resolution of 60 s corresponds to about 12 km of horizontal resolution. The normal extent of the probed clouds ranges between few tens of kilometres, when the cloud system is local, up to hundreds of kilometres, when the cloudiness is part of a synoptic system. A temporal resolution of one minute (or more) is then enough for most of the cloud targets, but may be not sufficient when I want to study a restricted area of few kilometres of horizontal extent.

A compromise between high resolutions and increasing signal noise is to apply one or more filters to the data. The filters used for this study are simple and very efficient and are based on the value of the signal-to-noise-ratio (SNR) of the signal itself. Data with less SNR value than a fixed threshold are filtered out of dataset and plotted as white pixels. In this section I selected an example of lidar data processing from the flight survey occurred during the TROCCINOX tropical campaign on 4 February 2005. The flight had as target to "chase" a tropical thunderstorm passing through and around a cloud anvil. The aircraft flew above large cloud structures and fine cirrus filaments outgoing from the anvil. Three different examples of combined resolutions and SNR thresholds provide in the next sub-section good information about the possibility to discriminate fine features from noise without losing real data.

5.2.1. Case description

From Fig. 5.3 to Fig.5.8 the results are presented in the following way: the horizontal axis gives the time in UTC. The vertical axis is the altitude above sea level (a.s.l.). The black line shows the position of the aircraft in time and altitude. The lidar determined values for backscatter and depolarization ratios are presented in colours. Distance from the lidar telescope increases with decreasing altitudes, then clouds below the aircraft are the closest features probed by the laser.

Are shown hereafter three different examples of combined resolutions and SNR threshold setting. Each examples includes two figures, the first showing the backscatter ratio, $BR(h)$, value and the second the depolarization ratio, $DR(h)$, value. Each figure is divided in Panel (a) and Panel (b). As I do not aim to present the entire lidar profile, but only the part showing the sub-visible cloud layer, the adjustments of resolution and SNR threshold are done in the figures only for this part and are performed in several iterations.

Fig. 5.3 and 5.4 show, respectively, the $BR(h)$ and $DR(h)$ with low temporal and vertical resolutions. The difference between Panels (a) and (b) is the value of the SNR threshold, set to zero (no filter) in Panel (a) and to 1.8 in Panel (b). The vertical resolution is about 85 m and the temporal resolution is 180 s (i.e., about 36 km). In the region below the cloud layer ($h < 14$ km) the noise is increasing also because of the signal extinction, as it can be seen in Fig. 5.3(a). In panel (b) this region is removed by the filter. As mentioned above, white pixels in the plot correspond to data points with not sufficient SNR value with respect to the threshold. This example shows that no data bringing real information about the cloud structure is lost by applying the filter. Real depolarizing features in clouds, in Fig. 5.4, are also not removed from the plot by the filter. The difference between Panel (a) and (b) is that a more clear information can be retrieved from the data in Panel (b). In fact, in Panel (a) the signal is somehow drowned in the noise, making difficult the data interpretation.

Fig. 5.5 and 5.6 show, respectively, the $BR(h)$ and $DR(h)$ with high temporal and vertical resolutions. The difference between Panels (a) and (b) is the value of the SNR threshold, set to 1 in Panel (a) and to 1.5 in Panel (b). First, it is useful to remark the differences occurring between the Panels (b) in Fig 5.5. and 5.6 and Panels (b) in previous Fig. 5.3 and 5.4. Increasing both resolutions, a larger number of fine structures arises from data in Fig 5.5 and 5.6. Clouds that looked like single clouds are now shown as separated cloud parts. Working at high resolutions implies a reduction of the signal integration over time (and space) and then a reduction of the SNR (the shot noise component is reduced by averaging as described in Sections 2.3.2 and 3.3.1). It is then a bad solution to increase the resolution and to filter the data with large SNR thresholds. Actually, differences between Panel (a) and Panel (b) in Fig. 5.5 stay in the loss of some small cloud features (see black circles) in the plot with higher SNR threshold (SNR = 1.5). On the other hand, Panel (a) clearly shows more noisy data and it asks more work for the interpretation. The loss of real data is even more clear in Fig. 5.6, looking at differences between Panel (a) and (b). In several regions the value of $DR(h)$ does not reach the threshold set at SNR = 1.5 and is automatically filtered out from the plot.

Fig. 5.7 and 5.8 show, respectively, the $BR(h)$ and $DR(h)$ with same SNR threshold (1.5) and same temporal resolution (6 s). The difference between Panels (a) and (b) is the value of the vertical resolution, (42 m in Panels (a) and 85 m in Panels (b)). For the same reasons as for the previous case, some data is lost in Panel (a) with respect to Panel (b). Nevertheless, the loss of data is not so important as in the previous case. Lost cloud features (highlighted by the black circles) are especially evident in Fig. 5.8, in Panel (a). Another difference between Panel (a) and (b), in Fig. 5.7 is the overall value of $BR(h)$, higher in Panel (a). Actually, decreasing the resolution the mean value of $BR(h)$ also decreases. A consequence of the overall decreased value is a deficit of information about tiny (but real) features with small $BR(h)$ value. An example is the thin cirrus capping a cloud anvil highlighted by the red circle in Panel (b) of fig. 5.7. Then, decreasing too much the temporal or the vertical resolutions it more difficult to interpret isolated, tiny data features with small average $BR(h)$ value.

In conclusion, the filter SNR should be set to a value between 1 and 2. The temporal and vertical resolutions have to be increased or decreased accordingly to the type of information I want to retrieve from the data, but they should not be too high when the SNR value is low.

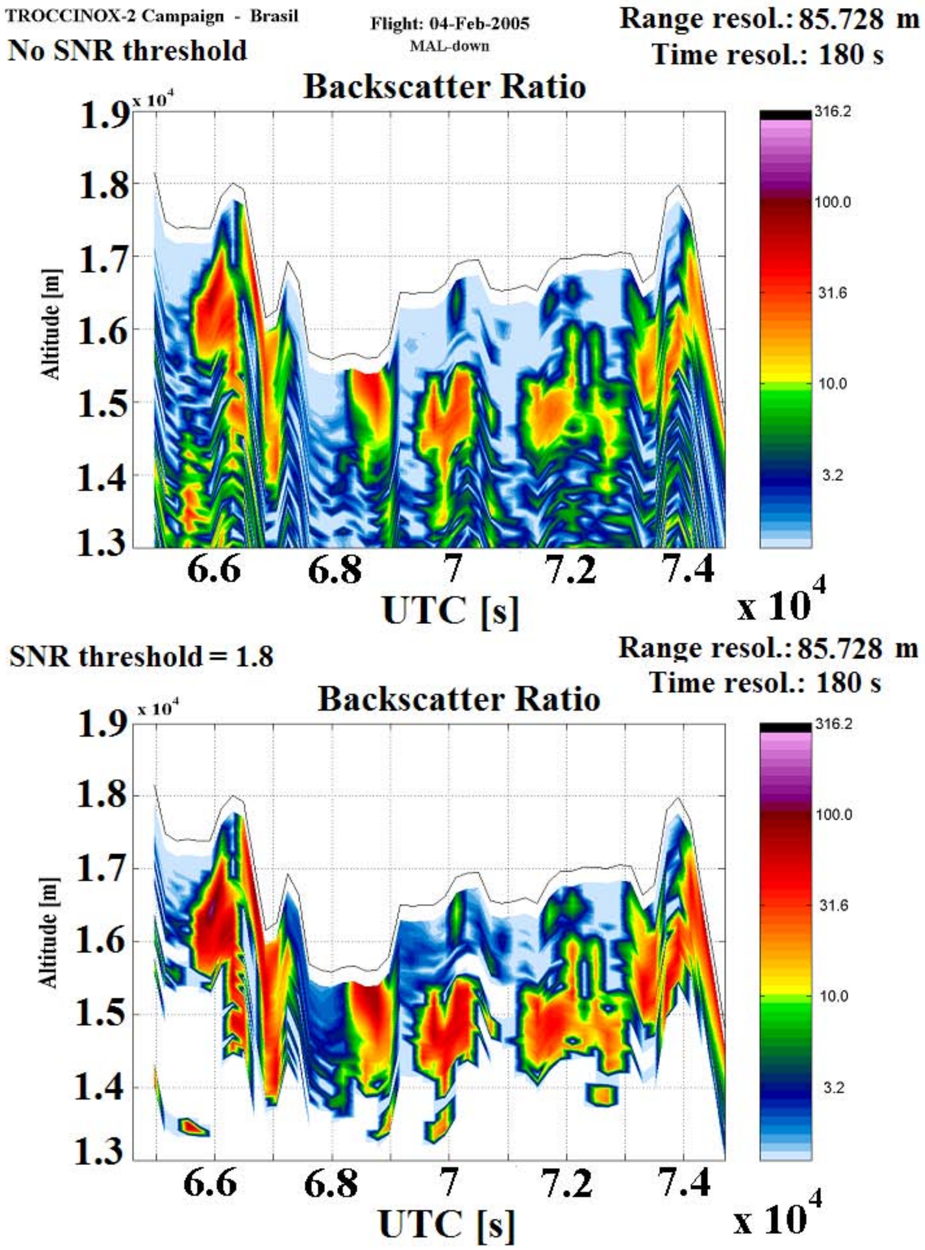

Fig. 5.3. Flight survey of 4 February 2005 in the frame of the tropical TROCCINOX campaign (Araçatuba, Brazil). Panel (a) shows the backscatter ratio, *BR*(*h*), value with no applied SNR filter on the data. Panel (b) shows the same data as in Panel (a) but with the SNR filter applied to data with a threshold equal to 1.8. White pixels in Panel (b) correspond to the removed data points. Temporal and vertical resolutions are, respectively, 180 s ad 85 m.

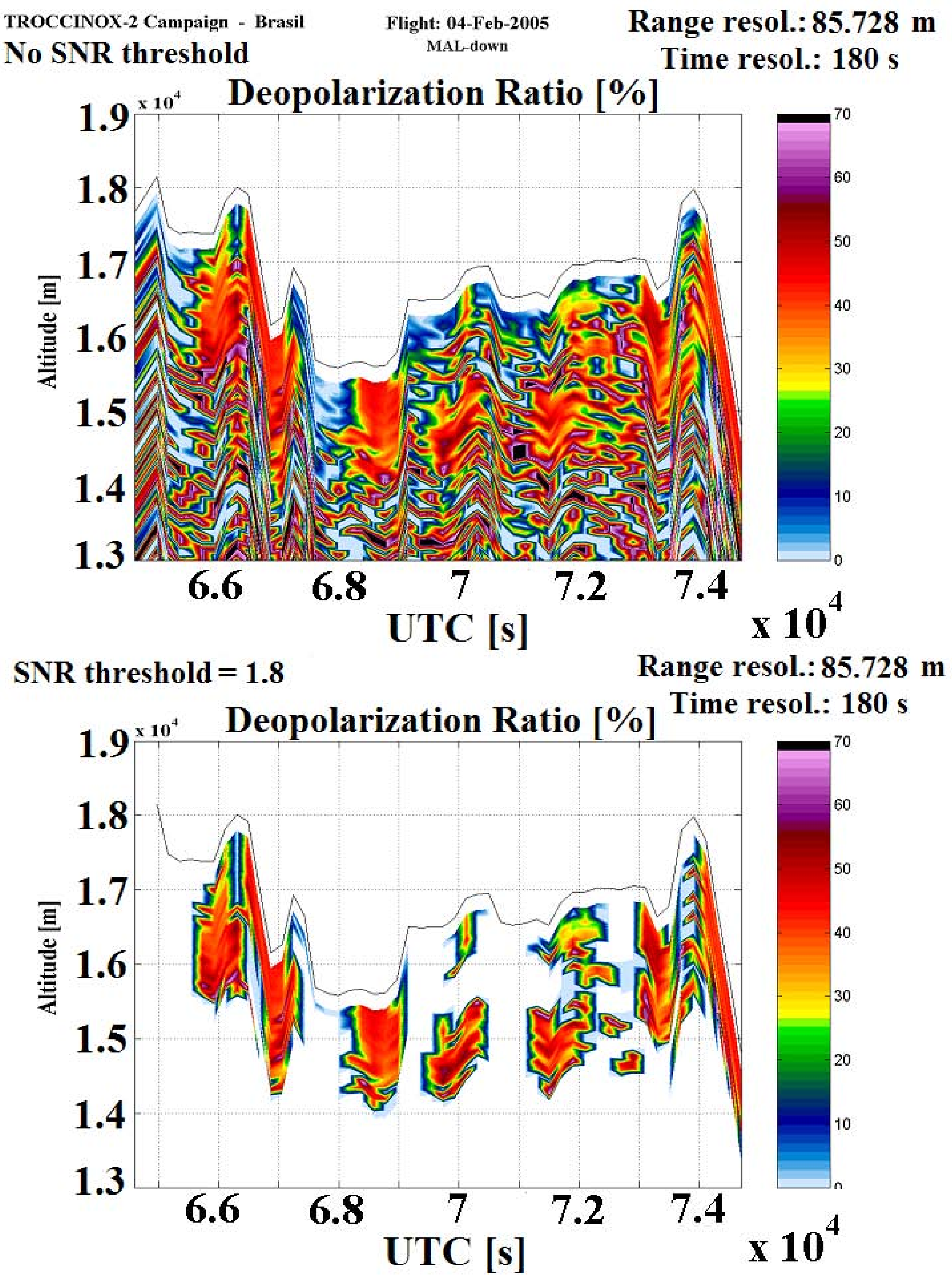

Fig. 5.4. Flight survey of 4 February 2005 in the frame of the tropical TROCCINOX campaign (Araçatuba, Brazil). Panel (a) shows the depolarization ratio, *DR(h)*, value with no applied SNR filter on the data. Panel (b) shows the same data as in Panel (a) but with the SNR filter applied to data with a threshold equal to 1.8. White pixels in Panel (b) correspond to the removed data points. Temporal and vertical resolutions are, respectively, 180 s ad 85 m.

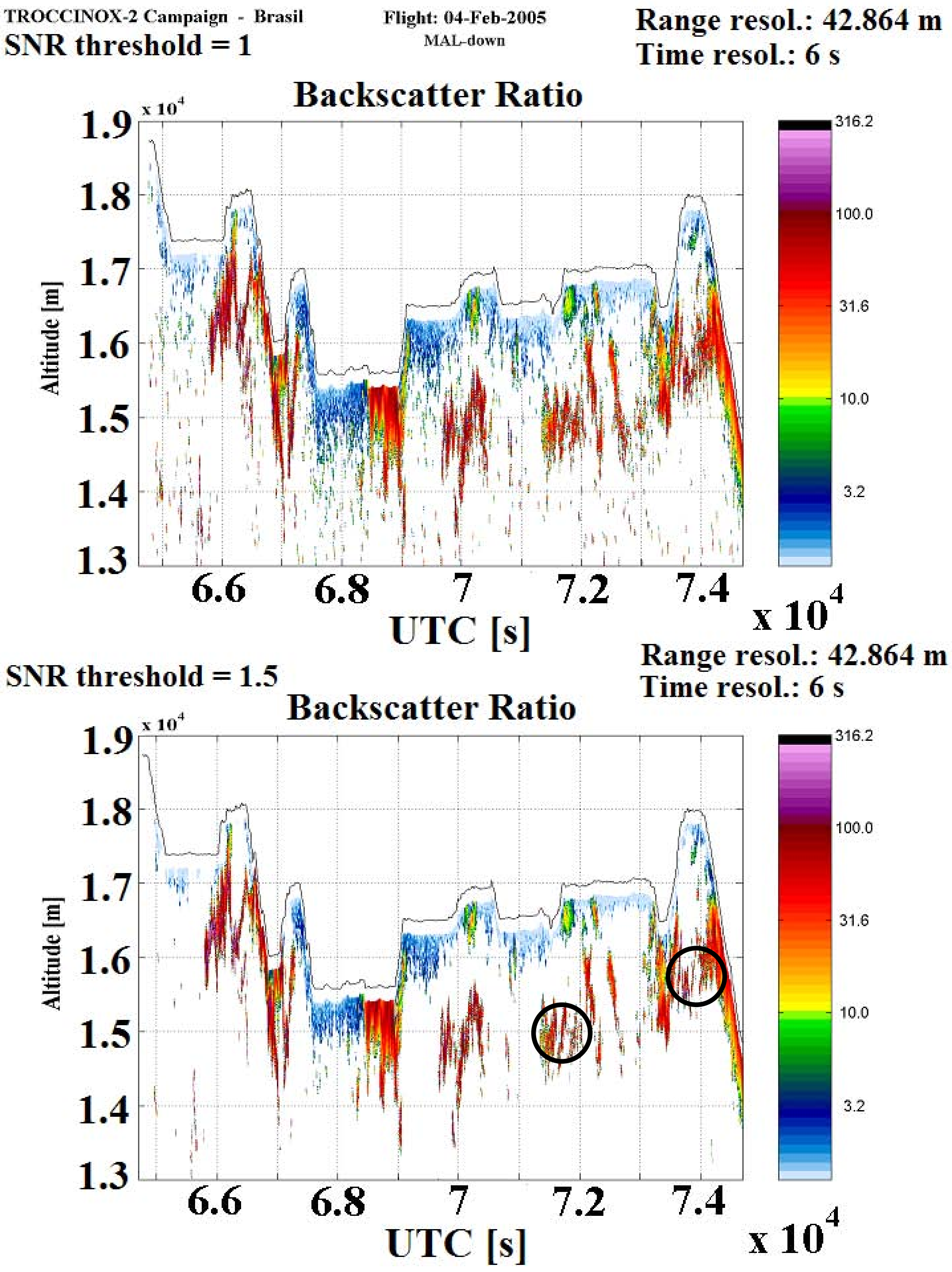

Fig. 5.5. Flight survey of 4 February 2005 in the frame of the tropical TROCCINOX campaign (Araçatuba, Brazil). Panel (a) shows the backscatter ratio, *BR(h)*, value with SNR filter threshold to 1. Panel (b) shows the same data as in Panel (a) but with the SNR filter threshold set to 1.5. White pixels in Panels (a) and (b) correspond to the removed data points. Temporal and vertical resolutions are, respectively, 6 s and 42 m.

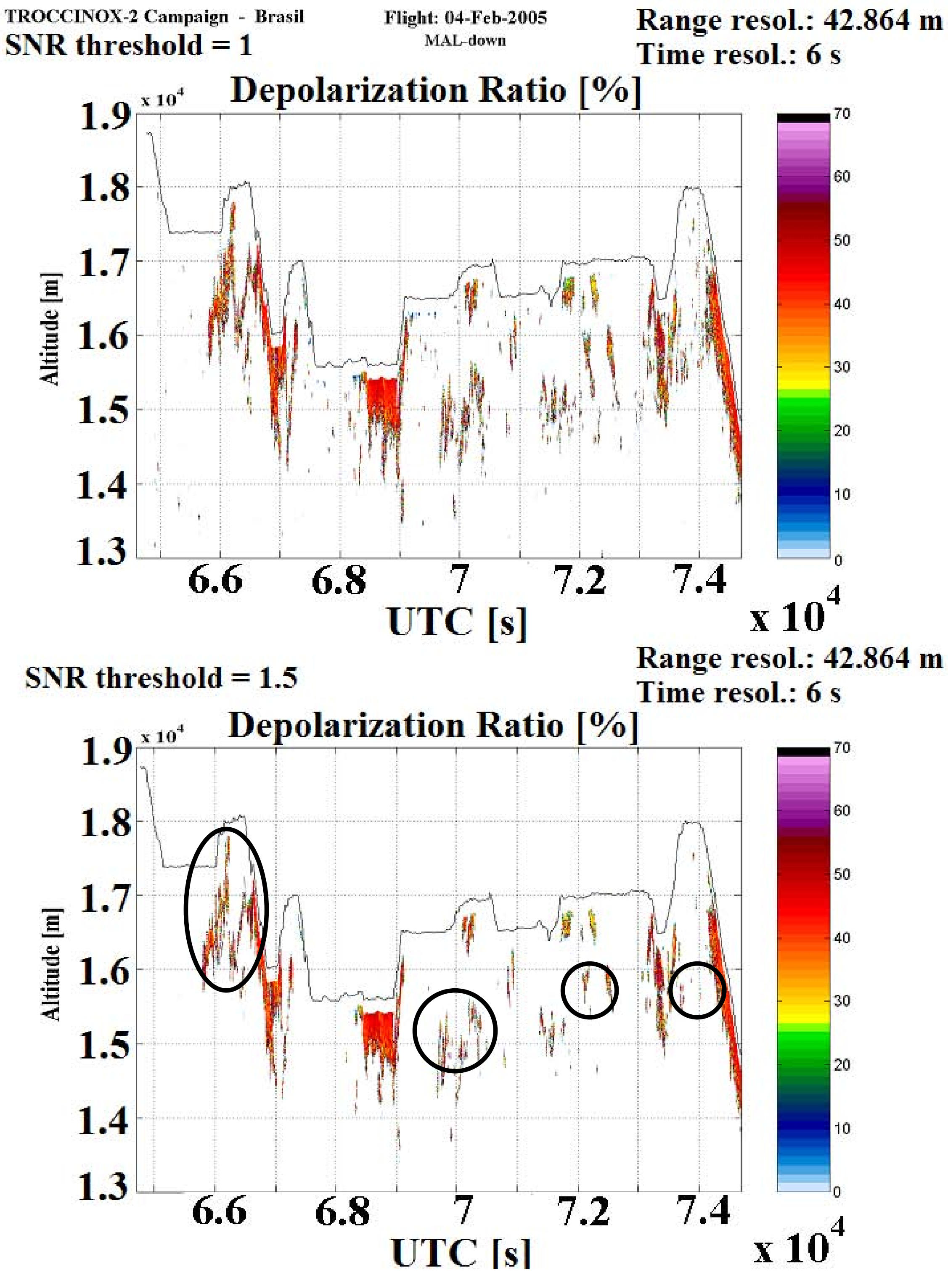

Fig. 5.6. Flight survey of 4 February 2005 in the frame of the tropical TROCCINOX campaign (Araçatuba, Brazil). Panel (a) shows the depolarization ratio, *DR(h)*, value with SNR filter threshold set to 1. Panel (b) shows the same data as in Panel (a) but with the SNR filter threshold set to 1.5. White pixels in Panels (a) and (b) correspond to the removed data points. Temporal and vertical resolutions are, respectively, 6 s and 42 m.

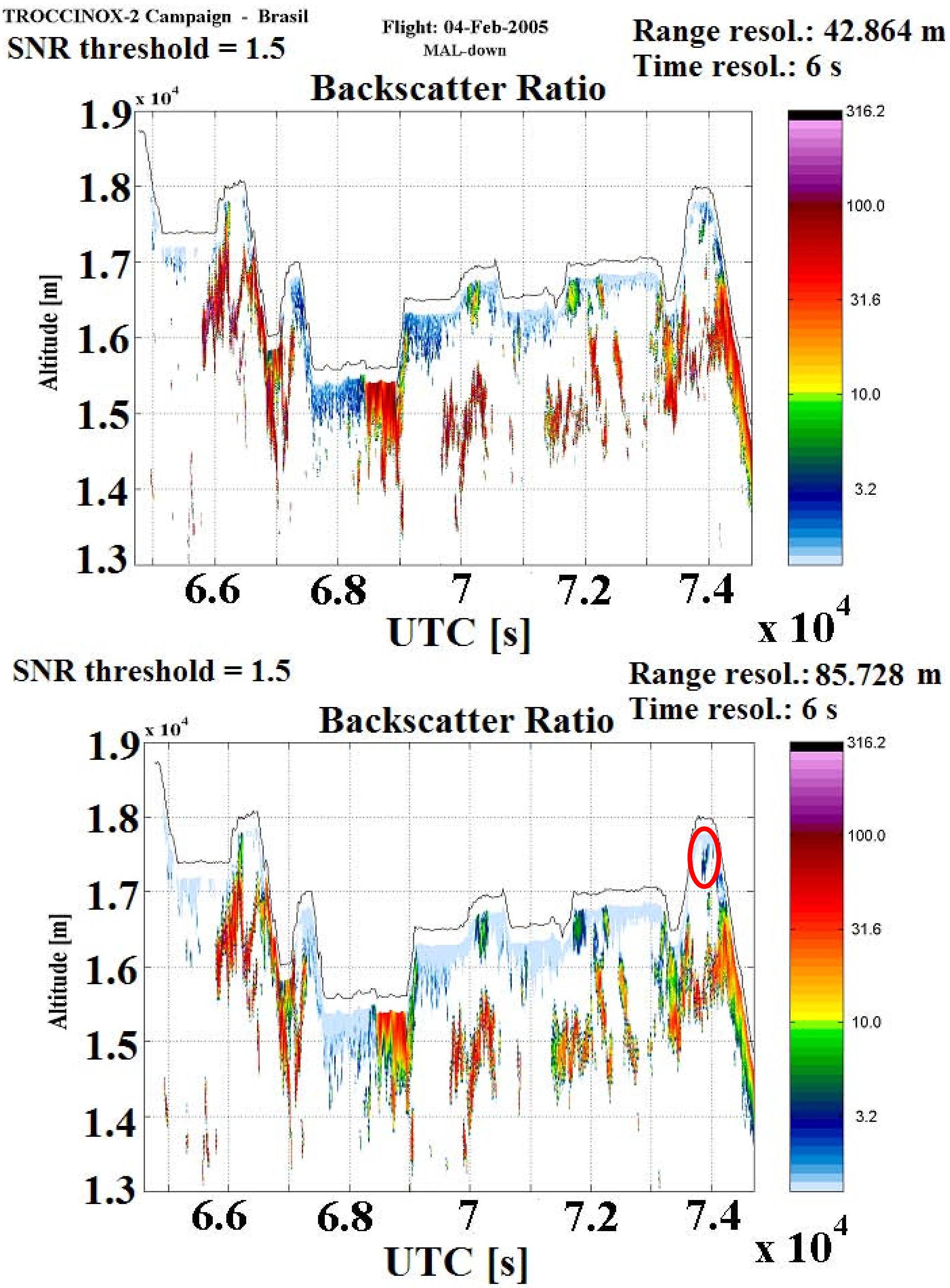

Fig. 5.7. Flight survey of 4 February 2005 in the frame of the tropical TROCCINOX campaign (Araçatuba, Brazil). Panel (a) shows the backscatter ratio, *BR(h)*, value with temporal and vertical resolutions, respectively, 6 s and 42 m. Panel (b) shows the same data as in Panel (a) but with temporal and vertical resolutions, respectively, 6 s and 85 m. White pixels in Panels (a) and (b) correspond to the removed data points. The SNR filter threshold is set to 1.5 for both data distributions in the panels.

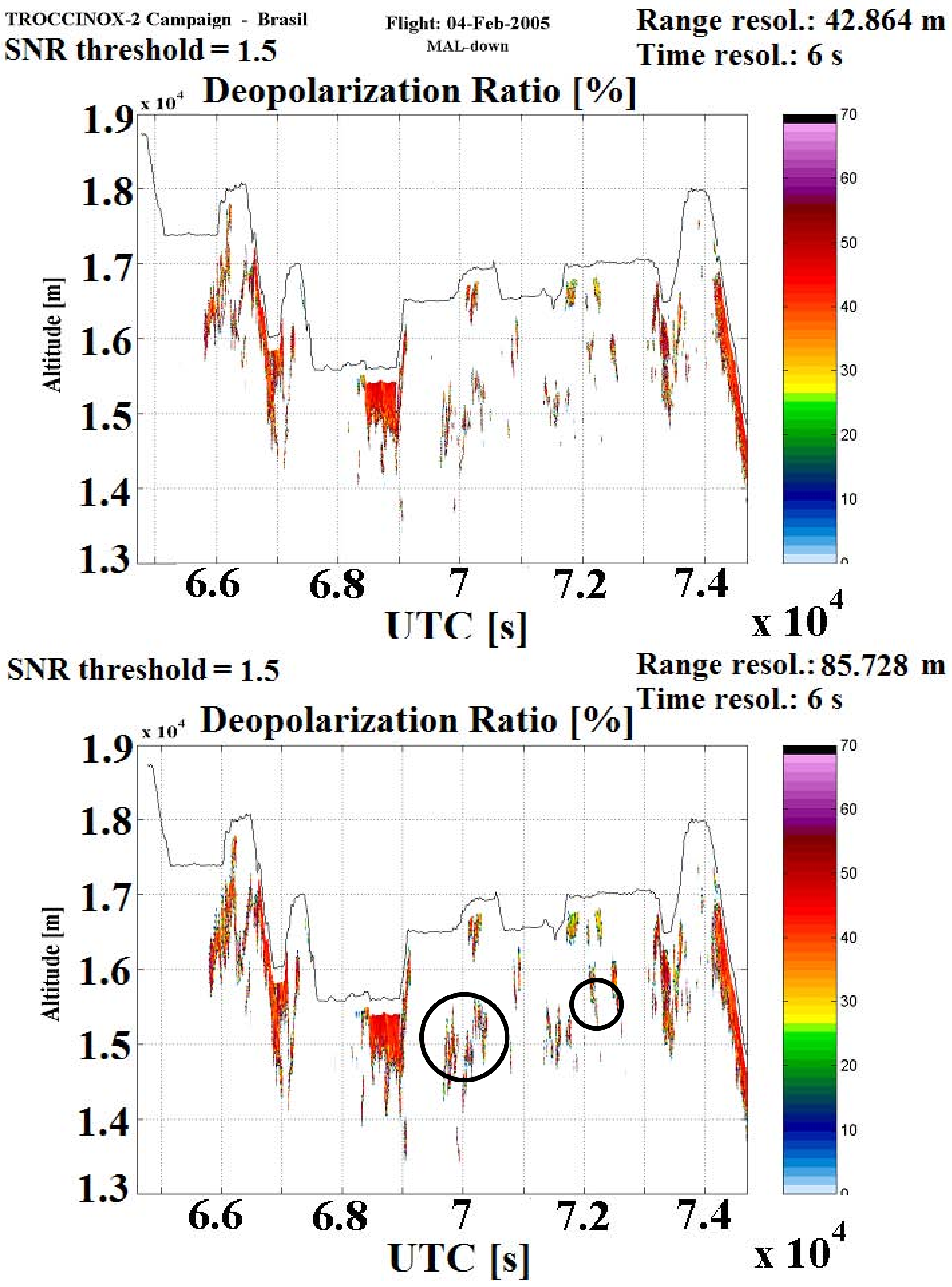

Fig. 5.8. Flight survey of 4 February 2005 in the frame of the tropical TROCCINOX campaign (Araçatuba, Brazil). Panel (a) shows the depolarization ratio, *DR(h)*, value with temporal and vertical resolutions, respectively, 6 s and 42 m. Panel (b) shows the same data as in Panel (a) but with temporal and vertical resolutions, respectively, 6 s and 85 m. White pixels in Panels (a) and (b) correspond to the removed data points. The SNR filter threshold is set to 1.5 for both data distributions in the panels.

5.3. Observations

In Section 5.1.2 I showed how *BR*(*h*) and *DR*(*h*), are computed starting from equations (5-2) and (5-4). In all the next plots these two variables will be representative for the processed lidar backscatter signal as measured during selected flights.

The total number of flights through the four field campaigns is summarized hereafter:

- ENVISAT: 4 flights
- EUPLEX: 8 flights
- TROCCINOX: 8 flights + 4 transfer flights from Europe to Brazil + 4 transfer flights from Brazil to Europe.
- SCOUT: 8 flights + 6 transfer flights from Europe to Australia + 6 transfer flights from Australia to Europe.

Data have been processed using values of temporal and vertical resolution and SNR threshold based on the knowledge acquired from the examples in Section 5.2.

5.3.1. Arctic campaign – clouds detection and validation

In Fig. 5.9 it is shown the flight trajectory of the ENVISAT/EUPLEX flight occurred on 02 March 2003. The values of *BR*(*h*) and *DR*(*h*), determined by MAL2 (downward probing) are shown in Fig. 5.10, respectively, in Panel (a) and (b). The horizontal and vertical axis show, respectively, the UTC time in [s] and the altitude in [m a.s.l.]. Data with not sufficient SNR are in white. The SNR threshold is set to a value of 1.5. The black line is the flight altitude, the initial and final points in the plot geographically coincide.

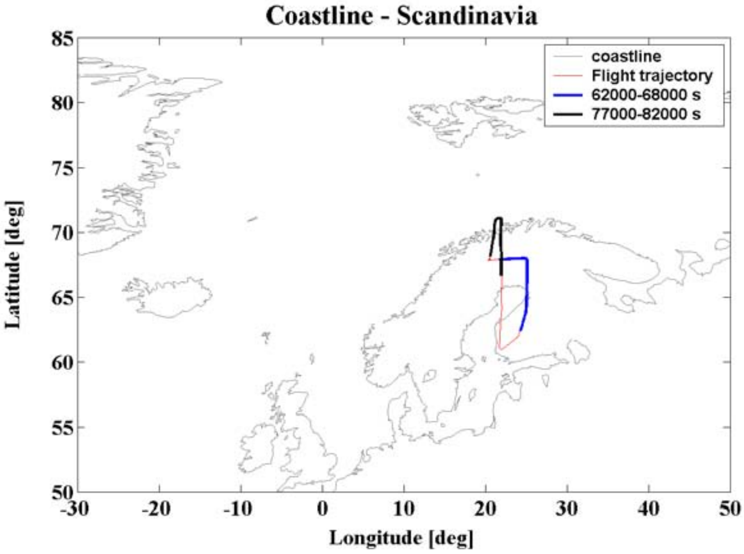

Fig. 5.9. Flight trajectory of the ENVISAT/EUPLEX flight held on 02 March 2003. Two cloud systems, part of the same warm front on the north of Scandinavia, are highlighted in blue and black colours.

A synoptic warm front, coming from southwest, established since the early morning above the north of Sweden and Finland and stayed up to the night and during the flight (from 1845 to 2255 UTC). From 68'000 s till 72'000 s the lidar probed an optically and geometrically thick cloud. After 74'000 s a thin cloud appears, going again into a thicker one at about 78'000 s. This second cloud system is almost symmetric with respect to the point at 80'000 s. In Fig. 5.9, the black, thick line indicates the part of the flight between 77'000 s and 82'000 s, symmetric with respect to the most northern point of the flight leg. The first (blue line) and the second (black line) observed cloud systems are part of the same warm front. Thickness of the clouds and cloud top altitudes are actually similar in the two flight legs. The front is composed by cirrus and cirrus-cumulus clouds. The thin cloud-branch between 64'000 s and 77'000 s represents the southern border of the front.

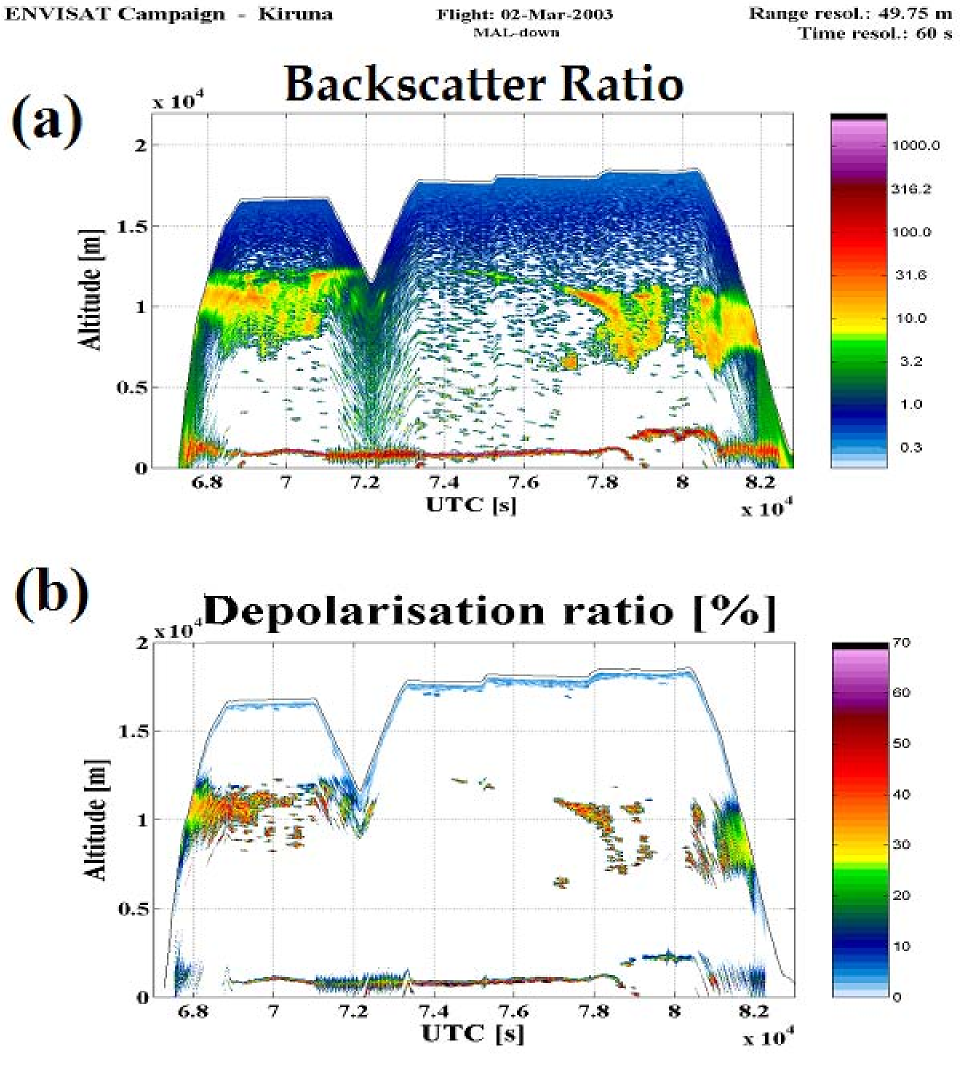

Fig. 5. 10. Backscatter ratio, in panel (a), and depolarization ratio, in panel (b), of cirrus clouds obtained during the flight on 02 March 2003 (Kiruna, Sweden). Temporal and vertical resolutions are 60 s and 50 m, respectively. The SNR threshold is set to 1.5.

An example of individual lidar *RCS* profiles respectively for *p* and *s* polarization signals are shown in Fig. 5.10b.

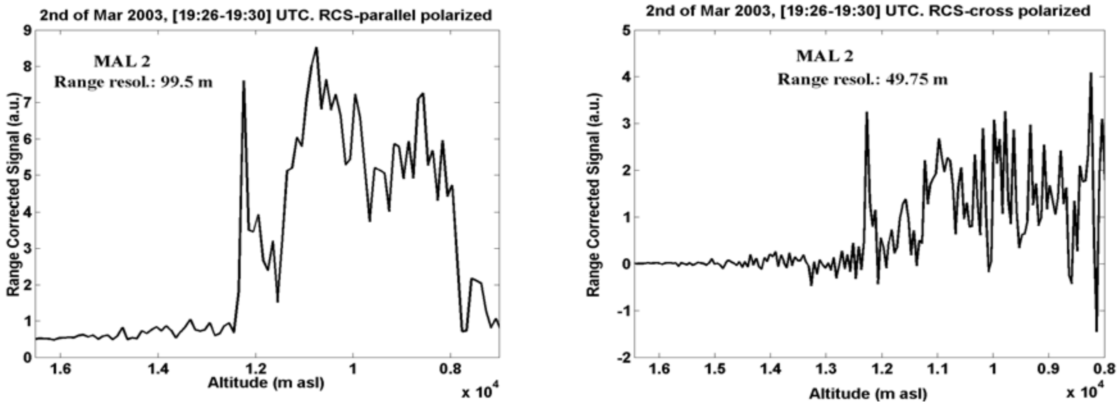

Fig. 5. 10b: Individual RCS profiles for MAL1 during the flight on 2 March 2003. The signals are from the cloud shown in Fig 5.10. The left panel shows the *RCS* for *p*-polarization, while the right panel shows the *RCS* for *s*-signal. The time of signal detection is from 69960 s till 70200 s UTC.

Due to the nadir probing direction, the cloud base is more distant from the lidar telescope than the cloud top. The signal backscattered from lower altitudes has then to pass through the entire cloud in order to reach the lidar telescope where it arrives extremely attenuated. Intensity of the received parallel component is generally larger than the perpendicular one and this is even more accentuated as the distance from the telescope increases trhough the cloud. Since both cloud systems in Fig. 5.10 are optically and geometrically thick, due to insufficient SNR of *DR*(*h*), the lower part of the clouds, in Panel (b), are limited in depth. Panel (a), shows that during all the flight the lidar detected both surface and lower altitude clouds echoes, what is a proof for the high sensitivity and dynamic range of the lidar.

Another example of cloud detection is the EUPLEX/ENVISAT flight of 11 February 2003. The flight trajectory is shown below, in Fig. 5.11.

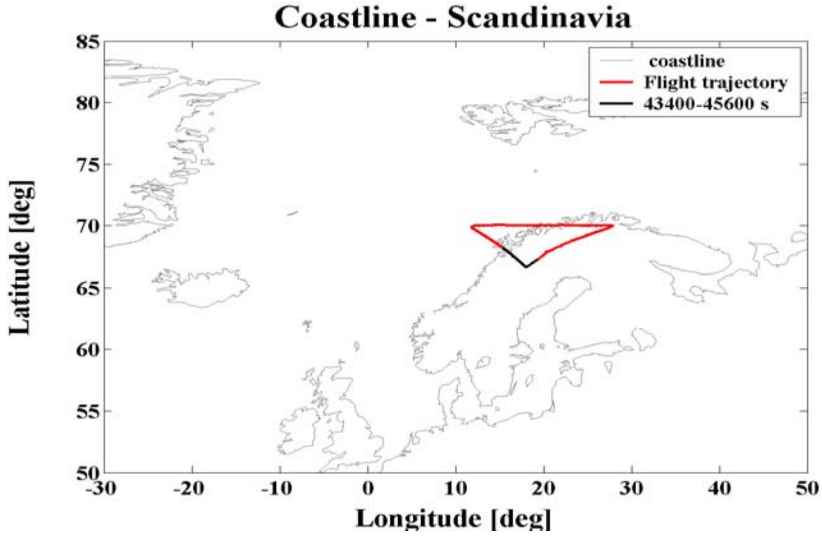

Fig. 5.11. Flight trajectory (red line) of the ENVISAT/EUPLEX flight held on 11 February 2003. The black line corresponds to the flight leg between 43400 s and 45600 s (~1200-1240 UTC).

The flight trajectory, shows with a black line the leg between 43'400 s and 45'600 s, i.e. the part of the flight in which the aircraft crossed the clouds. The vertical profiles of *BR*(*h*) and *DR*(*h*) this time measured by MAL1 (zenith probing), are presented in Fig. 5.12.

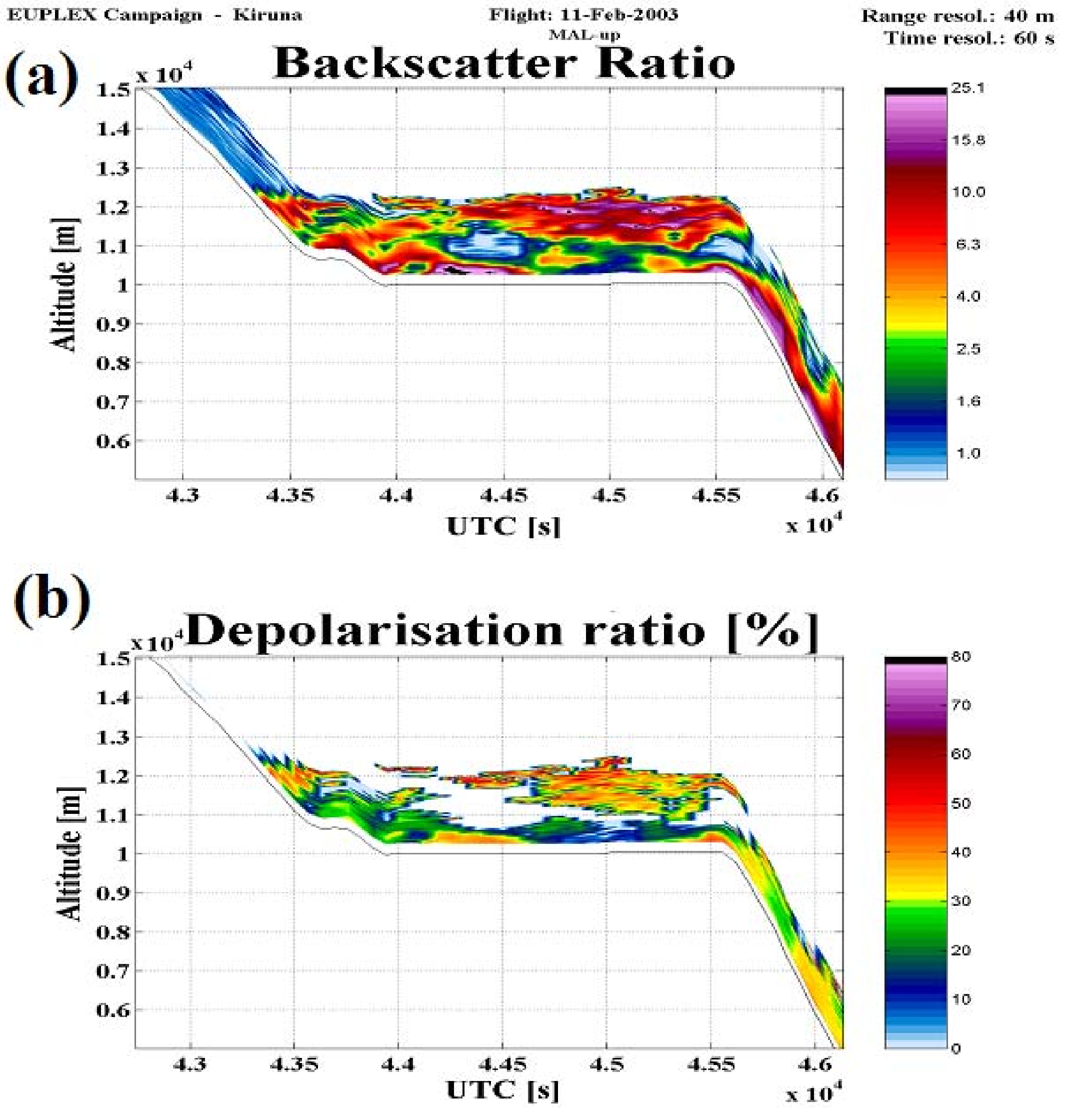

Fig. 5.12. Backscatter ratio, in panel (a) and depolarization ratio, in panel (b), of cirrus clouds observed during the EUPLEX flight on February 11, 2003 (Kiruna, Sweden). Temporal and vertical resolutions are 60 s and 40 m, respectively. The SNR threshold is set to 1.5.

In this case also, a warm front moved from south west to the north of Scandinavia in the first hours of 11 February 2003. The flight survey began at around 0930 UTC and ended at around 1300 UTC. A cloud system developed inside the front with highest clouds presumably at the level of the presented flight leg, i.e. 12-13 km. The temporal and vertical resolutions in Fig 5.12 are, respectively, 60 s and 40 m. Cloudiness is detected during a horizontal flight leg at 10 km altitude between 43'500 s and 45'500 s. Basing on the arguments and conclusions discussed in the previous section, I investigate here the possibility to retrieve a better information from the data increasing the resolution with the same SNR threshold. In Fig. 5.13, the same case is shown, but with higher temporal and vertical resolutions: 15 s, the temporal, and 10 m, the vertical. Differences between Fig. 5.12 and Fig. 5.13 specially arise from features in *BR*(*h*) value. Clouds between 44'600 s and 45'500 s, in Panels (a), are thin and stratified. At the levels of 11'200 m and 12'000 m two very thin (few hundreds meters) cloud layers appear one above the other and they both are depolarizing (see Panels (b)).

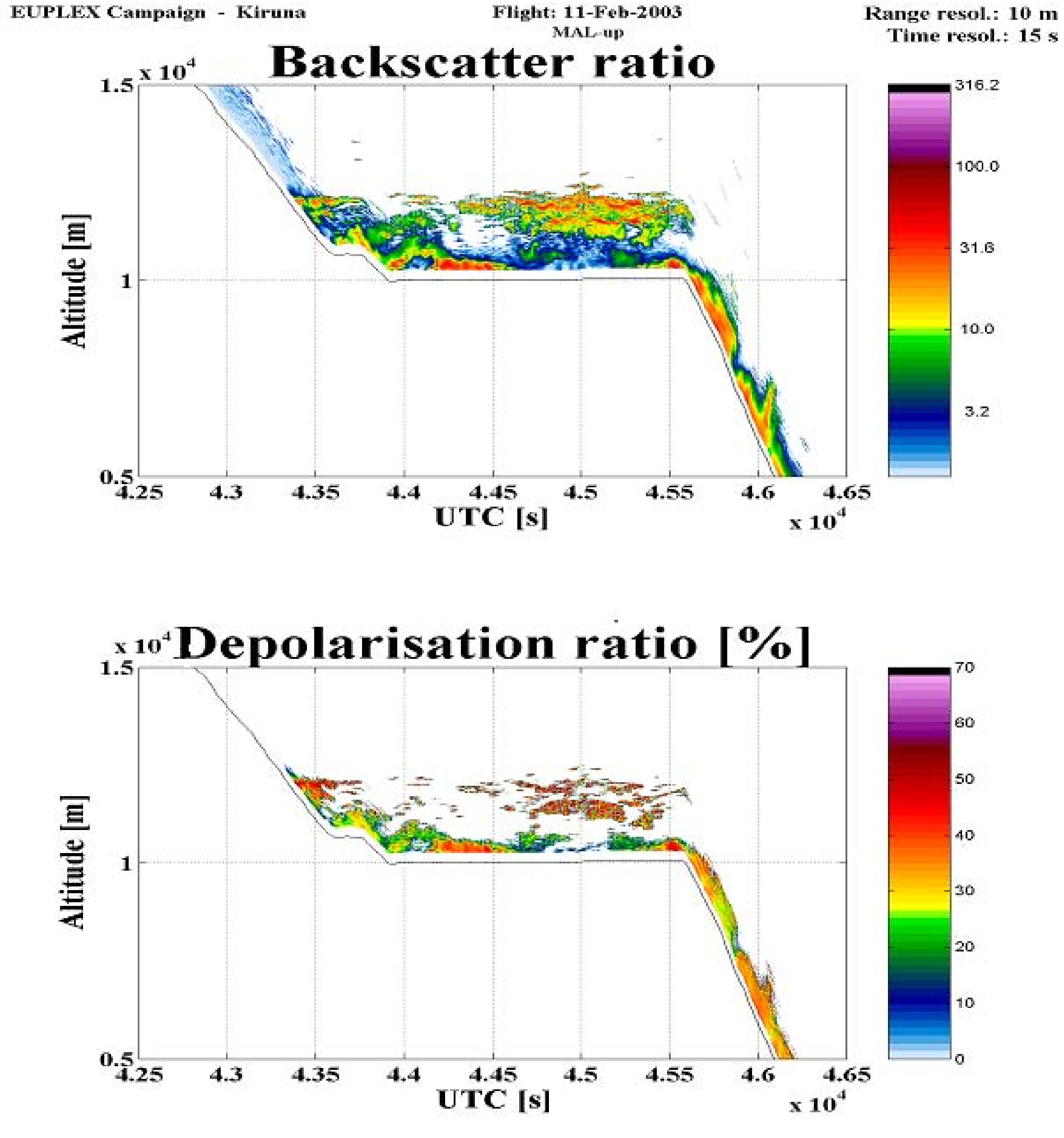

Fig. 5.13. Backscatter ratio, in panel (a) and depolarization ratio, in panel (b), of cirrus clouds observed during the EUPLEX flight on February 11, 2003 (Kiruna, Sweden). Temporal and vertical resolutions are 15 s and 10 m, respectively. The SNR threshold is set to 1.5.

5.3.1.1 Cross-comparison of cloud detection with two lidars for ENVISAT validation

The airborne lidars ABLE and MALs (up and down) participated both in the ENVISAT validation campaign. As MAL, also ABLE was installed on the high-altitude research aircraft M-55. From M-55 ABLE provides vertical profiles of the backscattering ratio at three wavelengths (1064, 532 and 355 nm) and of the aerosol depolarization ratio at 532 nm. The lidars, ABLE and MAL, provide the cloud top altitude and, for optically thin clouds, the optical and geometrical depths. During the validation flights, cloud and aerosol layers have been detected under night- and day-time conditions. Hereafter measurements acquired during one flight on 02 February 2003 by the ABLE and MAL instruments are presented and compared.

Fig. 5.14 presents a comparison during a daytime flight, with a varying range from the aircraft to the cloud top. For high-altitude optically thin clouds, cirrus, good comparison occurs only within a range from the aircraft less than 3 km. When the range between the aircraft and the cloud top starts to exceeds 3 km, i.e. to be well above the day-time detection range of MALs, the comparison is good only for low-altitude optically thick clouds.

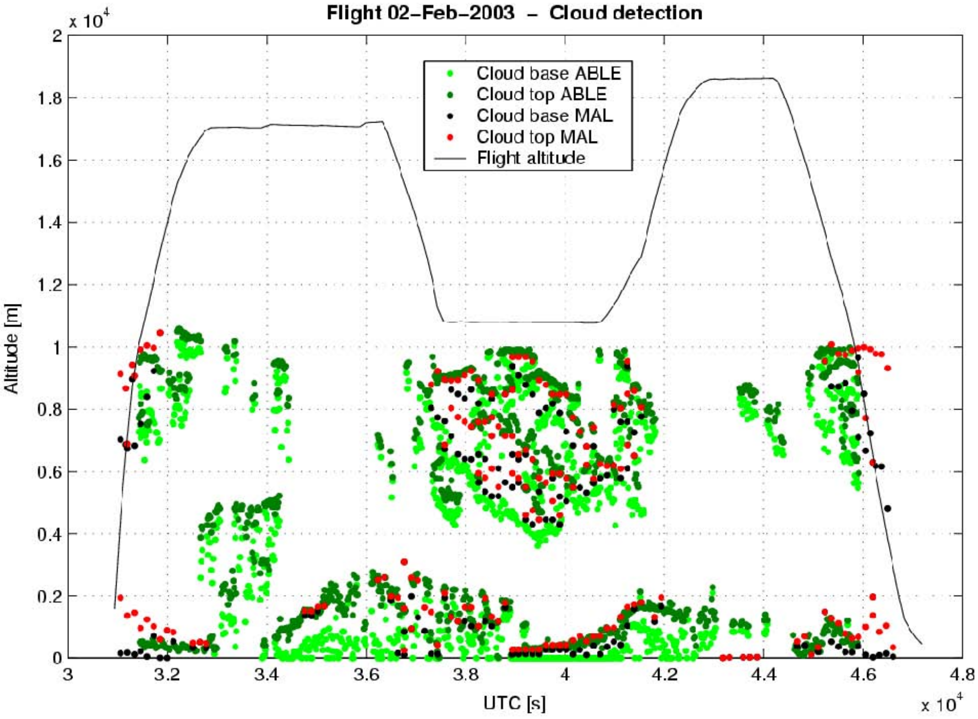

Fig. 5.14. Cloud boundary obtained by ABLE and MALs during the flight on 02 Feb. 2003 (Kiruna, Sweden).

5.3.1.2 PSC detection

Two examples of polar stratospheric clouds detection are given in this section. One case is a clear observation of PSC, presumably of type II, occurred above the Swedish-Norwegian Alps at an altitude of 23 km. The second case it is not a clear PSC event, but the backscatter ratio clearly increased in a region close to the aircraft. The correspondence with a sensible decrease of the air temperature in the same region makes reasonable the hypothesis of a very thin PSC.

During the EUPLEX flight on January 15, 2003, MAL1 detected a PSC extending between 22 and 24 km. Fig. 5.15 shows the position of the PSC along the flight trajectory on the map of Scandinavia.

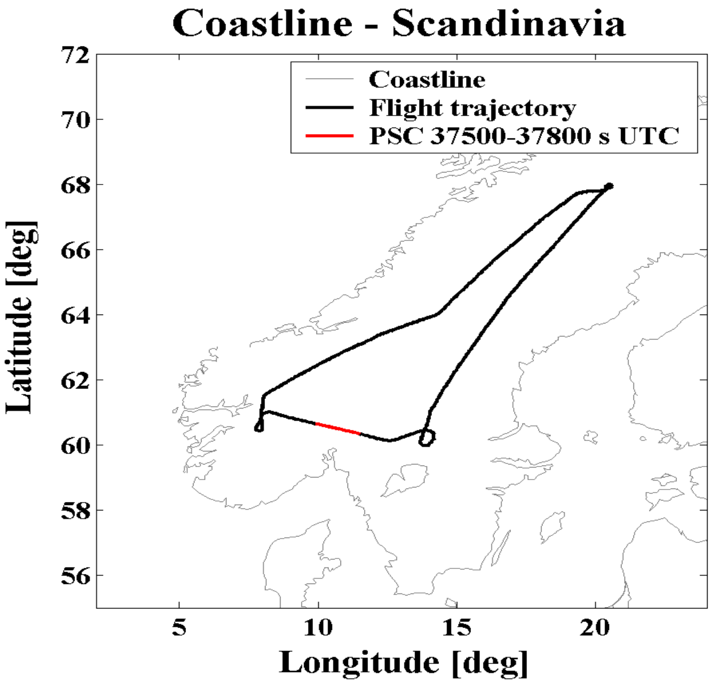

Fig. 5.15: Flight trajectory of the EUPLEX flight survey held on January 15, 2003. The red line along the flight trajectory indicates the position and the extent of the observed PSC.

Fig. 5.16 presents the backscatter and depolarization ratios as in the cases above. In panel (a) it is shown also the cross-section of the orography below the aircraft. From Fig. 5.15 and Fig. 5.16 it can be observed that the cloud is shifted to the southeast with respect to the most elevated part of the mountain range in that area. During 15 January 2003 the wind was blowing from W/NW over the Jotunheimen mountain range, in southern Norway. Over Oslo (approximately where the PSC was observed), at the surface level, the direction of the wind was different, coming from S/SW. The wind across the Jotunheimen mountain barrier engendered the lee-waves system on the lee of the mountain where the PSC was observed. The high values of the backscatter and depolarization ratios, as well as the elevated area above which the cloud is detected, are consistent with lee-waves PSC type II.

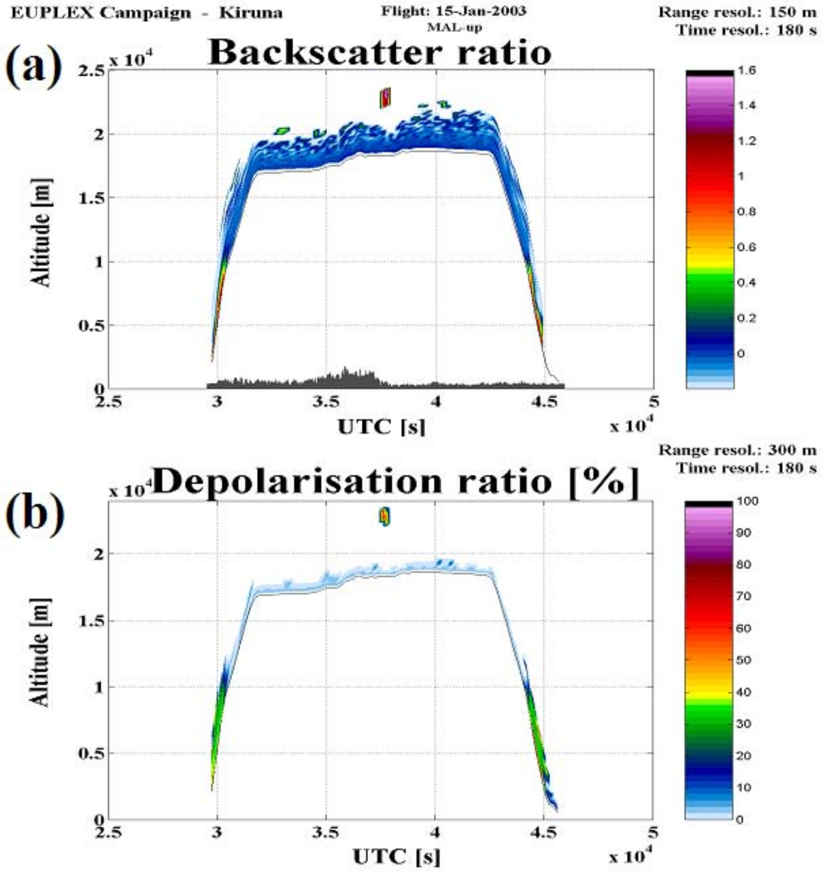

Fig. 5.16: Backscatter ratio (upper panel) and depolarization ratio of PSC observed during the EUPLEX flight on January 15, 2003 (Kiruna, Sweden). Temporal and vertical resolutions are 180 s and 300 m, respectively. The SNR threshold is set to 1.5.

Below, Fig. 5.16b presents individual *RCS* profiles, showing the response from the observed PSC respectively for *p* and *s* polarizations.

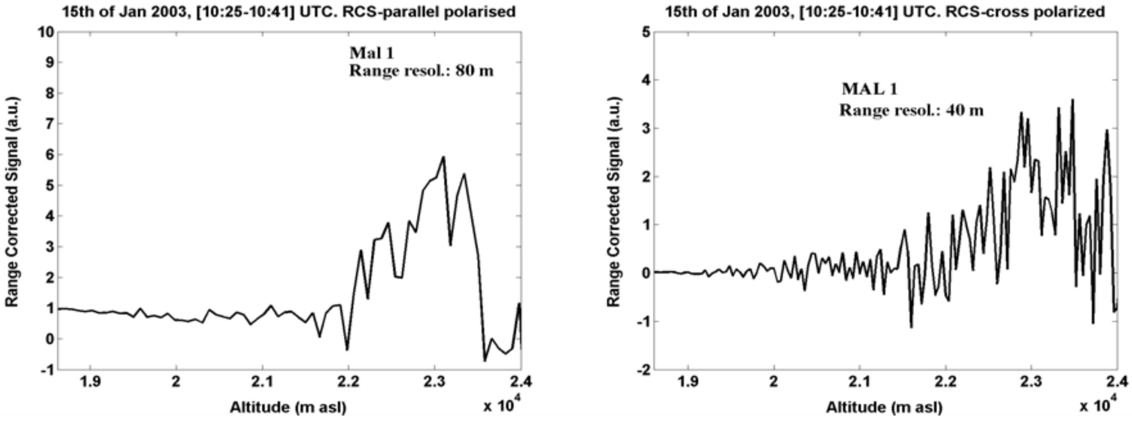

Fig 5.16b. Single *RCS* profiles detected by MAL1 during the flight on 15 January 2003. The signals are from the PSC cloud shown also in Fig. 5.16. The left panel shows the *RCS* for polarization *p*, while the right panel shows the *RCS* for signal *s*. The time of signal detection is from 37000s till 38460s UTC.

Fig. 5.17 presents two extremely thin and faint PSCs during the flight survey on February 8, 2003. Temporal and vertical resolution, in the plot, have been reduced by the signal processing in order to decrease the noise on the single *BR* profiles and to reduce at maximum the false peaks in the signal. The PSCs are detected above the northern Norwegian mountain range (see in Fig. 5.18). During the UTC time intervals 62'300-62'600 s and 65'880-66'660 s were observed sensible local increases of the backscatter ratio value. In the same periods of time, the temperature of the air around the aircraft reached, respectively, a local and an absolute minimum of about -82ºC and -84ºC. The value of temperature and those of the *BR*(*h*) and *DR*(*h*) are not consistent with PSC type II.

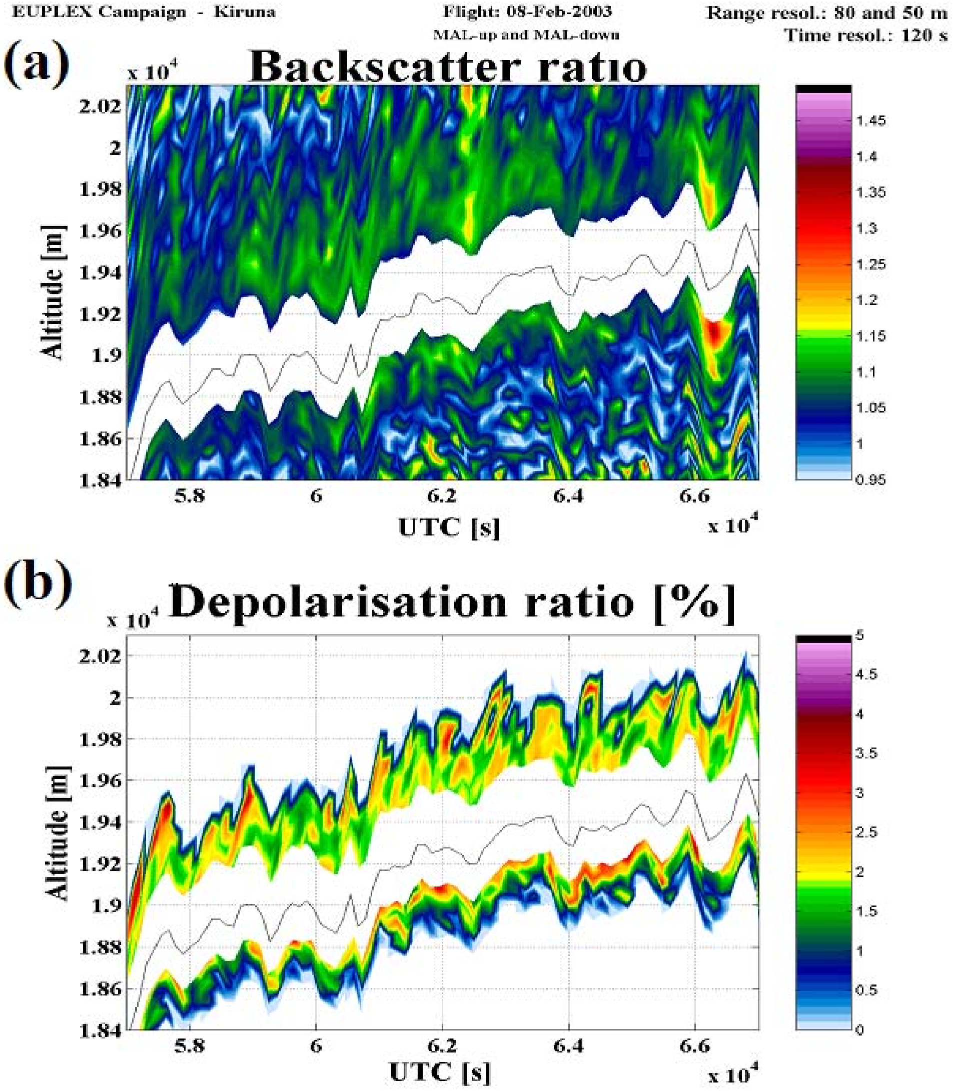

Fig. 5.17: Backscatter ratio (upper panel) and depolarization ratio of PSC detected during the flight on February 8, 2003 (Kiruna, Sweden). Temporal resolution is 120 s. The vertical resolutions are for MAL1 and MAL2 80 m and 50 m, respectively. The SNR threshold is set to 1.5.

The image from satellite AVHRR (not shown here) taken at 1922 UTC on the 8 February 2003, reveals a clear lee-wave pattern above the northern part of Norway. The wind over this region was blowing from NE, i.e., perpendicularly to several valleys and mountain segments. In Fig. 5.18 the silver-coloured traces represent the cloud pattern as it was seen by the satellite at approximately 68'500 s UTC. It is in this region that the two faint PSCs were observed. The two PSCs are although independent from the main cloud system that formed during the early afternoon at lower levels inside a synoptic front. During all the flight MAL2 measured the presence of clouds with increasing and decreasing levels in the range of altitudes between 7 km and 12 km. The whole flight, as measured by MAL2, is shown in the thumbnail in the lower-right corner of Fig. 5.18.

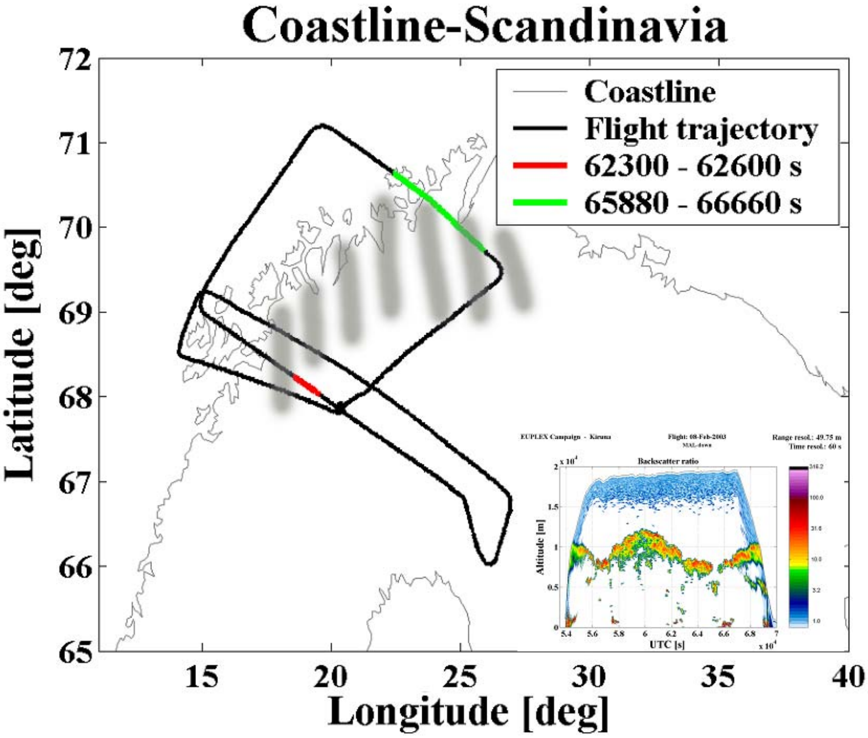

Fig. 5.18: Flight trajectory of the EUPLEX flight survey occurred on February 8, 2003 (Kiruna, Sweden). Colours of line sections are explained in the legend. The silver traces show the cloud pattern of a lee-wave system as it was observed by the satellite AVHRR at 1922 UTC (~ 68'500 s UTC). In the lower-right corner, in the thumbnail, is depicted the entire flight as measured by MAL2. The total flight duration is from 54'000 s to 70'000 s UTC.

5.3.2. Selected results from the tropical campaign TROCCINOX

One objective of lidar MAL2 in the frame of TROCCINOX was to study the occurrence of trace gases and particles in the UTLS in connection with tropical deep convection events. In particular, upwelling motions of significant amounts of water vapour bringing H_2O in the lower stratosphere. Another target of our research was the study of the ultra-thin tropical cirrus clouds (UTTCs). These are clouds that impact the radiative balance and play an important role in the water vapour budget in the stratosphere (McFarquahar G. M. et al, 2000; Jensen E. and L. Pfister, 2004). The campaign TROCCINOX took place in Araçatuba, Brazil, more than 10'000 km far from the airport in Oberpfaffenhofen where the Geophysica left. The transfer flights from Europe to Brazil and back over the Atlantic Ocean and the South America equatorial regions provided the opportunity to observe UTTC above the ocean and the continent. In Fig. 5.19 are shown the results from the oceanic leg of 23 January 2005 during the transfer flight.

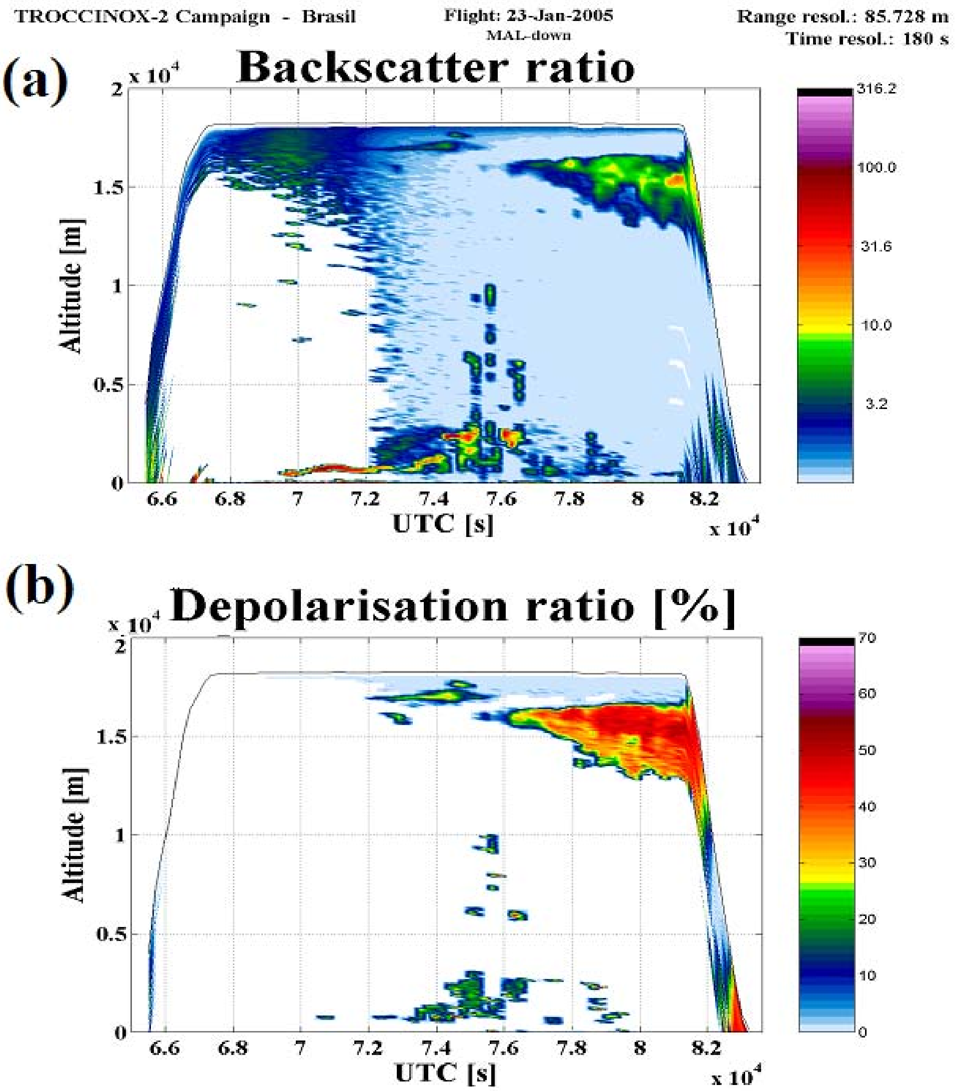

Fig. 5.19: Backscatter ratio, in panel (a), and depolarization ratio, in panel (b). UTTCs and cirrus anvil structures have been detected during the Atlantic transfer flight on January 23, 2005 (Capo Verde-Recife). Temporal and vertical resolutions are 180 s and 85 m, respectively. The SNR threshold is set to 1.5.

During the flight different sort of clouds were observed with diverse value of altitude, scattering and depolarization ratios. The measurements provided also inputs to evaluate the detection limit of MAL2, the only on-board lidar on the M55 "Geophysica" for this transfer. The flight occurred during dusk and night. Due to this, the signal is with a high SNR, which enables the detection of low altitude clouds and the sea surface. The large thick cloud close to the coast of South America is an extended cirrus anvil. The observation of the high ultra-thin cirrus took place between 72'000s and 76'000s above the central part of the Atlantic Ocean.

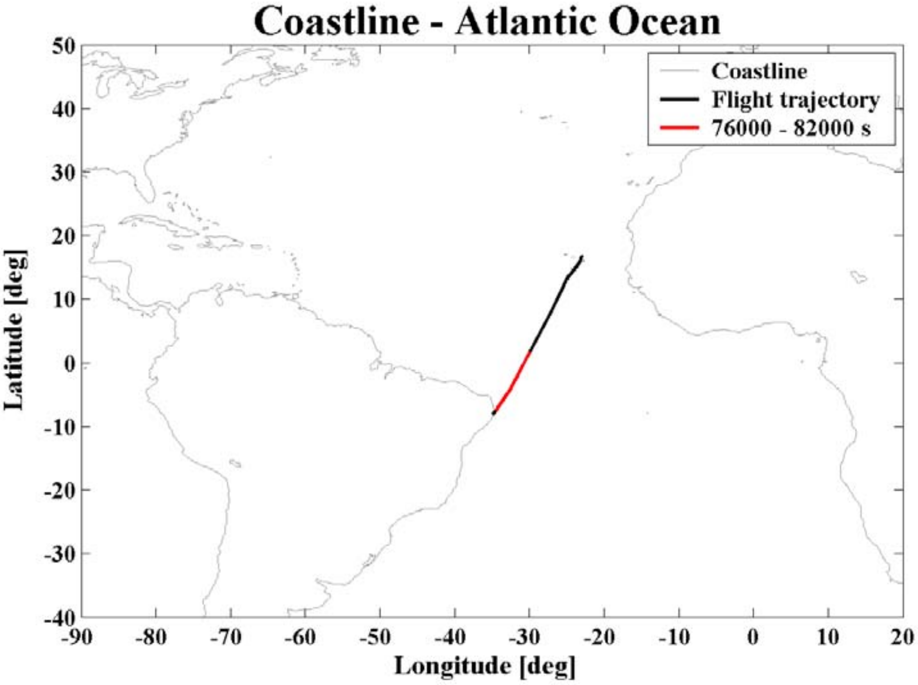

Fig. 5.20: Flight trajectory for the TROCCINOX transfer flight above the Atlantic Ocean, from Capo Verde (Sal) to Recife (Brazil) on 23 January 2005.

5.3.3. Selected results from the tropical campaign SCOUT-O3

SCOUT-O3, as TROCCINOX, aims to observe how water and chemical species are lifted by strong storms and to understand how they can reach the stratosphere in this way. An important part of each field campaign are the transfer flights. These represent a possibility to probe the UTLS over very long paths. Also for SCOUT-O3, the M55 aircraft started from Oberpfaffenhofen, in the south of Germany. The arrival was in Darwin, in the north of Australia, after flying 15'000 km from northern to southern hemisphere. One important region for tropical convection, flown over by the M55, is the Intertropical Convergence Zone (ITCZ). This is an area of low pressure that forms where the northeast trade winds meet the southeast trade winds near the earth's equator. As these winds converge, moist air is forced upward. This causes water vapour to condense, or to be "squeezed" out, as the air cools and rises, resulting in a band of heavy precipitation around the globe. This band moves seasonally, always being drawn toward the area of most intense solar heating, or warmest surface temperatures. It moves toward the southern hemisphere from September through February and reverses direction in preparation for northern hemisphere summer that occurs in the middle of the calendar year.

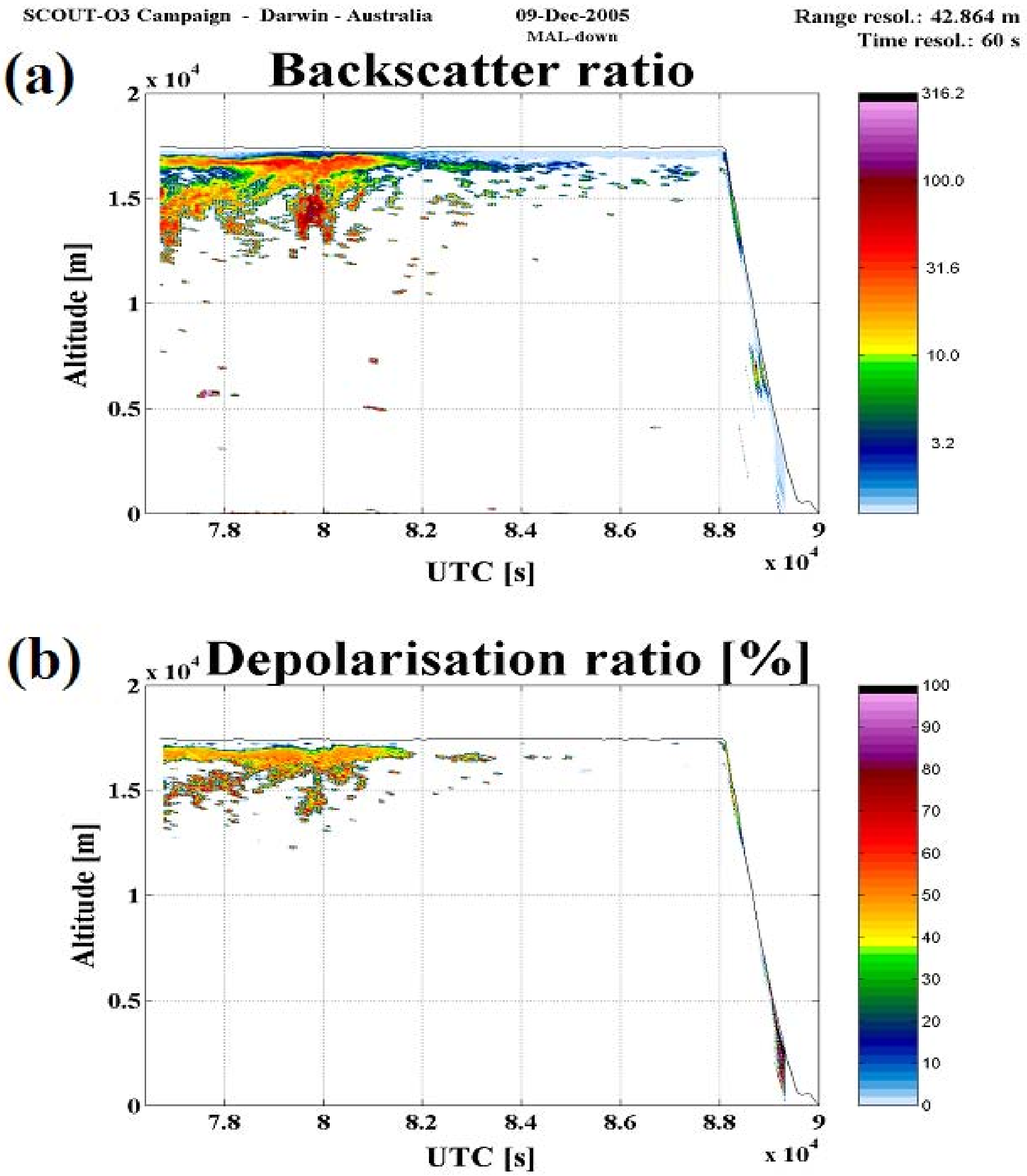

Fig. 5.21: Backscatter ratio, in panel (a), and depolarization ratio, in panel (b). UTTCs and cirrus anvil structures were observed during the transfer flight from Darwin (Australia) to Brunei, on December 09, 2005. The whole detected cloudiness at 17 km lies in the southern hemisphere. Temporal and vertical resolutions are 60 s and 42 m, respectively. The SNR threshold is set to 1.5.

In the region of Indonesia-Micronesia-north of Australia, the ITCZ reaches its maximum intensity between November and February. In Fig. 5.21 are shown the backscatter and the depolarization ratios as measured by MAL2 during the transfer flight, coming back to Europe, on December 09, 2005. The flight survey started in Darwin and arrived at Brunei, passing through the Equator and flying over the region of maximum ITCZ activity. The M55 passed over a cirrus anvil between 76'700 s and 85'400 s UTC. The aircraft moved toward the outer part of the anvil, since the cloud thickness diminishes with increasing time. The northern part of the cloudiness almost reaches the Latitude 0° and with few hundreds meters thickness can be regarded as an UTTC. The flight altitude was always around 18 km. The clouds below were observed at approximately 17 km, i.e. exactly the altitude of the tropopause as measured by the temperature profile shown in Fig. 5.23.

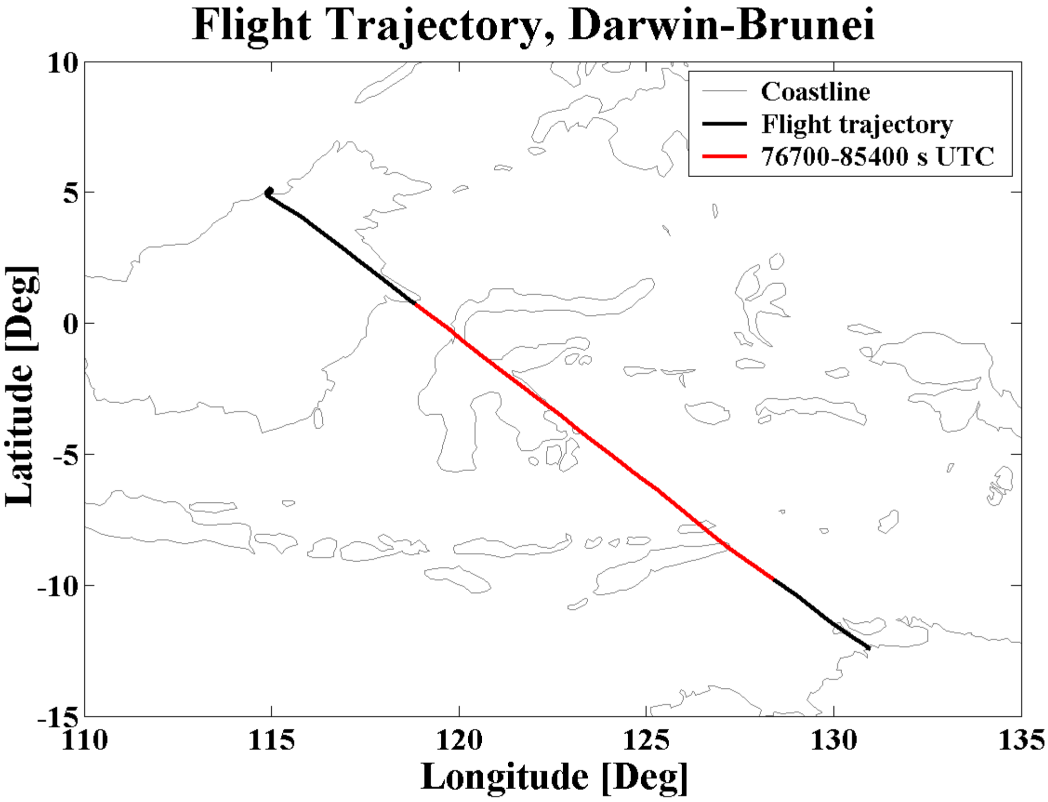

Fig. 5.22: Flight trajectory for the SCOUT-O3 transfer flight above Indonesia-Micronesia, from Darwin (Australia) to Brunei, on December 09, 2005.

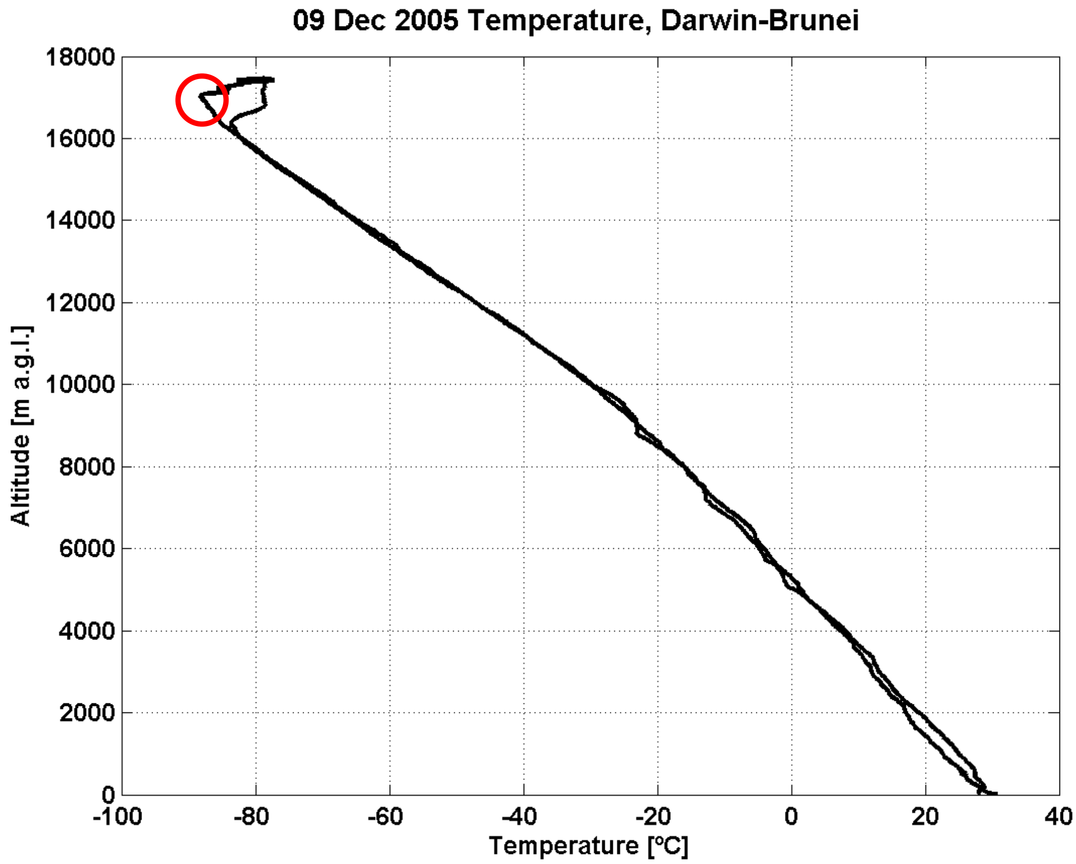

Fig 5.23: Vertical profile of the air temperature as measured by the onboard temperature sensor. The profile refers to the whole flight: the ascent after take off, the horizontal flight-leg and the descent before landing. The red circle indicates the lowest temperature value as a measure of the tropopause altitude (cold point).

5.4. Conclusion

Differently from the previous chapters, this last chapter presents a study not of the BL, but of the upper troposphere and lower stratosphere, i.e., the UTLS. The UTLS survey is overviewed by selected case studies collected during four field campaigns from 2003 to 2005. A first objective was to show the capabilities of lidar measurements presented here as vertical $BR(h)$ and $DR(h)$ profiles. The best compromise between high resolutions (temporal and vertical) and limited noise component has been investigated in Section 5.2. To optimize the quality of the information that can be retrieved from the data I also used a filter based on the value of the SNR. Working within the convenient range of resolutions and SNR threshold I computed the $BR(h)$ and $DR(h)$ values for representative flights through the four field campaigns.

The lidars employed for measurements are compact and automated instruments thought to be installed onboard an aircraft. Lidar airborne measurements are useful in atmospheric science not only for the possibility of extended observations of the atmosphere over large geographical areas, but also because allow to reach a specific target even at hundreds of kilometres distance. The common objective of the four campaigns was to improve the knowledge about the principal mechanisms that lead to the ozone depletion in the polar regions. To acquire this knowledge it was necessary to understand and realize the role of some trace gases transported by strong convection into the tropical stratosphere and then to polar stratospheric regions. The presented case studies show the observations of PSCs and polar cirrus clouds during the Arctic campaign as well as those of cirrus anvil in the frame of the two tropical campaigns.

The lidar contribution to the scientific campaigns of M55 "Geophysica" can be summarised as follows:

i. A number of cloud measurements used for validation of the cloud top detection performed by ENVISAT sensors. The three lidars (the Italian ABLE and the Swiss MAL1/2) installed on the Geophysica stratospheric aircraft mutually validated their measurements proving this way the full correlation between the two observations (Matthey et al., 2003).

ii. Detection of PSCs in situation of lee-waves during the EUPLEX campaign. The PSC detected on 15th December 2003 above the Scandinavian Alps was the only clear PSC event observed during the EUPLEX campaign, this was a confirmation of the PSC formation due to lee-waves in Arctic regions.

iii. A data base of UTTCs events during TROCCINOX and SCOUT O3. A comparison of UTTC detection (Martucci et al., 2006) above the Atlantic Ocean with the data provided by the DLR (Institut für Physik der Atmosphäre, Oberfaffenhofen) demonstrated the optimal agreement between the two airborne lidars: one on stratospheric aircraft, one on low-flying aircraft.

iv. Observation of aerosol layers above the anvil of strong tropical convections. A radar-vs-lidar comparison of anvil cloud top altitude (Calheiros et al., 2005) during the TROCCINOX campaign validated the employed airborne lidar technique with respect to the traditionally adopted radar method.

The conclusion is that the backscatter lidar is a necessary instrument in the payload of a scientific aircraft. As a perspective, this potentially assures the aerosol and cloud inputs to the model studies of the critical processes in the ozone balance.

Conclusion, relevance and perspectives

There have been years of atmospheric lidar developments, resulting in realizations of instruments and algorithms for determination of a number of atmospheric parameters. Presently, one primary objective of the international community active in the area of instrument development is to demonstrate that the lidar is useful and in some cases necessary for the user communities. Particularly, for the elastic backscatter lidar, those are the communities in the atmospheric science and the ecological monitoring.

One efficient way to contribute to this objective is to demonstrate in valuable measurement cases the following: (i) that the information delivered by the lidar is critical to understand the studied phenomena; (ii) that the lidar may be realized as an instrument which is easy to install and to operate; (iii) that the information delivered by the lidar is interpreted without ambiguity; (iv) that this information is both relevant and complementary to the knowledge acquired with the already employed measurements and models.

The objective of my thesis follows the above understanding.

To contribute such objective I needed to select problems actual in the atmospheric studies. To analyse these cases I have used the instrumentation realized already in the team where I did my PhD work. My selection was for problems in the BL and in the UTLS, where the aerosol effect is of importance, namely: the continuous variation of the BL height over short and long periods and the consequences it has on the pollution balance within the BL. The key role that thin clouds and aerosol layers have in characterizing the ozone depletion process in the polar stratosphere starting from convective transport in the tropical regions.

To solve these problems I needed to develop algorithms and procedures for data processing in each studied case, where the results shall be values having straightforward interpretation.

Through the five chapters of this thesis there are presented several approaches and examples of backscatter lidar applications in determination of the aerosol stratification. Here I provide a summary of the significance of the obtained results in the context of the backscatter lidar application. Hereafter are also outlined trends of the perspective backscatter lidar developments in the studied field.

In Chapter 1 I gave an overview of the lidar theory as well as an introduction to the principal lidar methods used to process the data in Chapters 2 to 5. Each lidar method is used in the next chapters, modified with respect to the standard expression presented in Chapter 1. The modifications depend on the context of measurements, their specifics and the objective of the study.

Chapter 2 presented a database of lidar MLD evaluations through two years of measurements adding the information about the nocturnal atmospheric stratification, i.e. RL top and NAL height. Several studies already done, concern diurnal ML top altitude measurements, but very few investigations about the nocturnal cases exist. For this reason, the reported collection of diurnal and nocturnal cases represents a significant validation of the process to investigate the BL dynamics with a lidar. In this chapter, lidar data were compared to radiosonde data. It is widely accepted that the height of the BL corresponds to the height of the first temperature inversion as measured by radiosonde measurements. The presented lidar data showed an optimal agreement with the radiosonde potential temperature BL top detection. They demonstrate the reliability of lidar method to detect the top altitude of the day and night BL from a statistical point of view and not by considering a few well selected cases only. Another important point is the contribution that this statistic provides to the information about the air mixing at the BL top, not only during day when the process is enhanced by convection, but also in stable conditions. Actually, it is during the night when the BL is more shallow that aerosols sediment into the lower atmospheric levels resulting in higher concentration above the ground. To my opinion, this last aspect justifies the interest in studying and monitoring the BL and motivated my investigation.

The relevance of the achieved results is that I proved the good correlation between the lidar and the radiosonde temperature both in convective (day) and stable (night) conditions. The requirements for a larger database and the necessity for automated processing procedure are also very well understood in the scientific community active in the field of the presented study. Previous lidar studies have not fulfilled this, demonstrating the feasibility of this lidar technique only in convective conditions, on fewer cases and never with the nocturnal aerosol stratification (Sicard et al., 2006; Wiegner et al, 2006).

The perspective of the presented validation of the lidar measurement of the BL stratification is that the determination of the BL development may be performed by lidar in long continuous measurements, where the results are fully compatible with the traditional occasional measurements.

Chapter 3 investigates the frequency (and then the rate of air entrainment) of the BL top fluctuation in convective and stable cases. Actually, fluctuations of the BL top do not represent only a variation in the BL thickness, but also a way the air above is entrained into the BL, particularly during convective processes. Using a fast Fourier transform (FFT) of the temporal variation of the BL top, it is possible to determine the frequencies of the wave processes acting at these altitudes. One objective of this chapter is to give a robust interpretation of the obtained frequency spectra based on the different processes occurring within and at the top of the BL. The investigation of the most probable oscillation, responsible for a specific frequency in the FFT spectrum is based on the knowledge of the actual meteorological conditions and the local topography. For both convective and stable cases, the "best fit" interpretation of the common frequency occurred in all FFT spectra is the presence of Kelvin-Helmhotz waves induced by the wind shear at the level of the BL top.

The relevance of the result in this chapter is in the verification that a backscatter lidar can retrieve not only averaged features in the BL (shown in the Chapter 2) but also fastevolving dynamics, like waves with period larger than few minutes at the top of the BL. The wave processes within the BL and at the interface between BL and the FT have considerable impact on the local meteorology and possibly on the exchange of pollution involving processes in the EZ (Neu et al., 1994; Beyrich and Gryning, 1997; Young et al., 1999). The study of the wave processes presently is limited by the necessity to involve aircrafts (Smith et al, 2002) or frequent balloons launching.

The achieved results are interesting not only for the new established possibility to retrieve a larger information from backscatter lidar measurements, but also for the perspective to quantify with prediction models the rate of the air-entrainment inside/outside the BL using backscatter lidar data for their assessment (Werne, 1994). Another important standpoint of the lidar method is in the possibility to enlarge substantially the number of the studied cases of wave presence and influence on the pollution exchange.

Chapter 4 concerns one of the most actual topics of the BL study, i.e., the urban BL (UBL). The inner structure of the UBL is complex and multi-layered due to the extremely irregular surface. The problem of the urban BL is not only of scientific significance; actually, it is of primary importance to improve the knowledge about its dynamics because cities are the environment where a large number of people live and work. Trapping of pollutants and micro-scale circulation are part of the effects following the urban BL development. That is why the UBL above the city have to be monitored, together with the pollution gases and the concentration of particulate matter smaller than or equal to 10 and 2.5 microns (PM10 and PM2.5). Due to the less complicated surface, the dynamics characterizing the rural BL are not the same as for the UBL. Mean BL temperature, momentum and heat fluxes are different outside the urban area and depend more on general wind circulation aloft. For this reason it is easier to parameterize the BL development in rural areas. Conversely, it is necessary to collect a large database in order to create a climatology and to use it to forecast future UBL development using models. This chapter presented not only the database containing the UBL height daily development for 89 cases, but also a consistency study between lidar and meteorological in-situ data for two case studies. The comparison between remote lidar and in-situ meteorological measurements provided a comprehensive information of the UBL dynamics and showed once more that lidar can provide large datasets as well as for specific and detailed BL investigation.

The BUBBLE project, in which our lidar was deployed for one year in the city of Basel, was part of COST 715(COoperation in the field of Scientific and Technical Research). The task of our lidar was the detection of the UBL height in an almost uninterrupted modality for one year. The final report of the COST 715 program (Piringer and Joffre, 2005; Fisher et al., 2005) presented the measurements of UBL height shown in this chapter as a reference value for this important atmospheric variable during the whole BUBBLE project.

The achieved results represent a basis of investigation and an improvement of the BL knowledge in urban environment not only in the frame of the BUBBLE project. They also represent a further perspective to operate the ecological monitoring in urban sites and in continuous way using the elastic backscatter lidar as a ground-based measurement station.

Chapter 5 presents measurements of thin sub-visible clouds and aerosol layers in the upper troposphere and the lower stratosphere (UTLS), i.e., a region comprised between about 8 and 30 km. The scientific interest of this atmospheric region is in the necessity to study the ways the chemicals enter the stratospheric polar vortex and the initialization of the reactions depleting the ozone layer. The production of active chlorine by chemical processes occurring on the surface of polar stratospheric cloud (PSC) particles inside the polar vortex causes the chemical ozone loss (WMO, 1999). The next question is how the chemical ingredients are transported to the polar lower stratosphere from the BL, where they are produced and accumulated. The present hypothesis is that this is fulfilled by general transport of chemicals from tropical BL to the tropical lower stratosphere and then to lower stratosphere in the polar regions. The way the chemicals are injected in the tropical UTLS is by deep convection as well as by large scale upwelling motions in tropical areas. This convective transport is traced by the formation of high cumulus clouds (Corti et al., 2006). The balance of water vapour at these altitudes is connected with the formation of cirrus (ice) clouds. The four field campaigns described in Chapter 5 have the common objective to investigate these two processes – the processes of ozone destruction and the processes for the transport of the chemical ingredients, participating in the destruction. On this purpose, the scientific aircraft M55 was used, with installed remote and in situ instruments. The contribution of our lidar to the scientific community has been in detecting the presence of convective cumulus clouds, thin aerosol and cirrus layers and PSCs. The synergy of all the instruments installed on the aircraft allowed a full comprehensive analysis of the retrieved data and provided the possibility to improve the knowledge on the principal mechanisms that lead to the ozone depletion in the polar atmosphere.

Presently, two high-altitude research aircrafts are used in UTLS studies, one is NASA ER-2 (McGill et al., 2002) and the other is M55 "Geophysica" (Luo et al., 2003; Matthey et al., 2004; Martucci et al, 2005). The recognition of the potential of the backscatter lidar, leaded to the installation of these remote sensing instruments on both aircrafts. The lidar is also used in lower flying aircrafts investigating the UTLS from below (Svendsen et al., 2005; Dörnbrack et al., 2002). As described in Chapter 5 the four field campaigns in which our two airborne backscatter lidars participated, represent a successful way to investigate the possible aerosol contribution to the processes leading to the ozone destruction in Polar regions.

The relevance of the results in Chapter 5 is in the extensive clouds database in this atmospheric region accumulated during all campaigns. The relevance of the results is also in the demonstration that the compact backscatter lidar may operate from a demanding platform and may bring such valuable knowledge. My contribution to the obtained results was in the research to improve the information that can be retrieved from backscatter data, applying filters and in realizing routines capable to extract the useful inputs concerning cloud parameters for the model previsions.

The principal objective of my PhD thesis work aimed at enlarging and deepening the application field of backscatter lidars. Since 2002 till now, my work has been to demonstrate by lidar measurements in specific studies and by the use of algorithms that a backscatter lidar is an instrument with a multitude of possibilities for atmospheric applications. My belief is that the obtained results will help consolidating the role of a lidar as a key instrument in atmospheric science and for environmental control.

List of acronyms

List of the acronyms used through the chapters of the thesis in alphabetic order

a.g.l.	Above Ground Level
APD	Avalanche PhotoDiode
a.s.l.	Above Sea Level
BL	Boundary Layer
BR	Backscatter Ratio
BUBBLE	Basel Urban Boundary Layer Experiment
CALIPSO	Cloud-Aerosol Lidar and Infrared Pathfinder Satellite Observations
CBL	Convective Boundary Layer
CBLH	Convective Boundary Layer Height
DR	Depolarization Ratio
EARLINET	European Aerosol Research Lidar Network
ENVISAT	Environmental Satellite
EUPLEX	EUropean Polar stratospheric clouds and Lee waves Experiment
EZ/EZT	Entrainment Zone/Entrainment Zone Thickness
GS	Gradient Signal
KH	Kelvin-Helmhotz wave
FFT	Fast Fourier Transform
FOV	Field Of View
FT	Free Troposphere
LCL	Lifting Condensation Level
LITE	Lidar In-space Technology Experiment
MAL1/2	Miniature Aerosol Lidar 1/2
ML/MLD	Mixed Layer/Mixed Layer Depth
NAL	Nocturnal Aerosol Layer
NBL	Nocturnal Boundary Layer
NBLH	Nocturnal Boundary Layer Height
NE	North East
NW	North West
PM10/2.5	Particulate Matter 10 or 2.5 micron
PMT	Photo Multiplier Tube
PSC	Polar Stratospheric Cloud
RCS	Range Corrected Signal
RL	Residual Layer
SCOUT-O3	Stratospheric-Climate links with Emphasis on the Upper

	Troposphere and Lower Stratosphere
SE	South East
SNR	Signal to Noise Ratio
SW	South West
TROCCINOX	TROpical Convection, CIrrus and Nitrogen OXides
UBL	Urban Boundary Layer
UBLH	Urban Boundary Layer Height
UTLS	Upper Troposphere and Lower Stratospheric
UTC	Coordinated Universal Time
UTTC	Ultra-Thin Tropical Cirrus
Var	Variance
θ	Potential temperature

Bibliography

Alpers, W. & Stilke, G., 1996: "Observation of nonlinear wave disturbance in the marine atmosphere by the synthetic aperture radar aboard the ERS-1 satellite". *J. Geophys. Res.*, **101**, No. C3, 6513-6525.

Balling, R.C., Jr, Cerveny R.S. 1987: "Long-term associations. between wind speeds and the heat island of Phoenix, Arizona.", *J. Clim. Appl. Meteorol.*, **26**, 712–716

Beyrich, F., and Gryning, S. E., 1997: "Estimation of the Entrainment Zone Depth in a Shallow Convective Boundary Layer from Sodar Data", *Jour. of Appl. Meteorol*, **37**, 255-268

Blumen, W., 1990: *Atmospheric processes over complex terrain*. William Blumen Editor, American Meteorological Society, 45 Beacon Street, Boston, Massachusetts

Borrmann, S., A. Thomas, V. Rudakov, V. Yushkov, B. Lepuchov, T. Deshler, N. Vinnichenko, V. Khattatov, L. Stefanutti, 2000: "Stratospheric aerosol measurements in the Arctic winter of 1996/97 with the Geophysika high altitude research aircraft", *Tellus*, **52B**, 1088-1103

Bösenberg, J., H. Linné, 2002**:** "Laser remote sensing of the planetary boundary layer", *Met. Zeitschrift*, **11**, pp. 233-240.

Bösenberg, J., and Coauthors, 2002: "EARLINET: Establishing the European Aerosol Research Lidar Network". *Lidar Remote Sensing in Atmospheric and Earth Sciences, Proceedings of the 21st International Laser Radar Conference*, L. Bissonette, G. Roy, G. Vallèe eds., Quebec City, Canada, Defense R&D Canada – Valcartier, Val-Belair, Quebec, Canada, pp. 293-296 .

Bösenberg, J., V. Matthias, 2003: "EARLINET: European Aerosol Research Lidar Network to establish an aerosol climatology". *Final report for the period of February 2000 to February 2003,* (Contract EVRI-CTI999-40003)

Brooks, I. M., 2003: "Finding Boundary Layer Top: Application of a Wavelet Covariance Transform to Lidar Backscatter Profiles", *Journal of Atmos. Oceanic Technol.*, **20**, 1092-1105.

Browell, E.V., C.F. Butler, S. Ismail, P. A. Robinette, A. F. Carter, N. S. Higdon, O.B. Toon, M.R. Schoeberl, and A.F. Tuck, 1990: "Airborne lidar observations in the wintertime Arctic stratosphere: polar stratospheric clouds", *Geophys. Res. Lett.*, **19**, 385-388.

Caccia, J. L., B. Benech, and V. Klaus, 1997: Space–time description of nonstationary trapped lee waves using ST radars, aircraft and constant volume balloons during the PYREX experiment. *J. Atmos. Sci.,* **54,** 1821–1833.

Calheiros, R.V., G. Held, V. Mitev, C.A.d.A. Antonio, G. Martucci and R. Matthey, 2005: "Ground and airborne validation plans for GPM in the central State of São Paulo, Brazil", *Proceeding of the 32nd Conference on Radar Meteorology, AMS, Albuquerque, USA*

Carswell, A.I., Hahn, J.F., Podoba, V.I., Ulitsky, A., Ussyshkin, V., Michelangeli, D.V., Taylor, P.A., Duck, T.J., and Daly. M., 2004: Lidar For Mars Atmospheric Studies On 2007 Scout Mission "Phoenix", *Proceeding of the 22nd International Laser Radar Conference*, **2**, 973-976

Caughey, S. J., and S. G. Palmer, 1979: Some aspects of turbulence structure through the depth of the convective boundary layer. *Quart. J. Roy. Meteor. Soc.,* **105,** 811–827.

Chen, W. N., Chiang, C. W., Nee, J. B., 2002: "Lidar ratio and depolarisation ratio for cirrus clouds." *Appl. Opt.,* **41**, 6470-6476.

Cohn, S. A, and W. M. Angevine, 2000: "Boundary Layer height and entrainment zone thickness measured by lidars and wind profiling radars", *J. Appl. Meteorol.*, **39**, 1233-1247.

Corti T., Luo B.P., Fu Q., Vomel H., Peter T., 2006: "The impact of cirrus clouds on tropical troposphere-to-stratosphere transport", *Atmos. Chem. Phys*., **6**, 2539-2547.

Cramer, O.P., 1972: "Potential Temperature Analysis For Mountainous Terrain". *J. Appl. Meteorol.* **11**, 44-50.

Davis, K. J., N. Gamage, C. R. Hagelberg, C. Kiemle, D. H. Lenschow, and P. P. Sullivan, 2000: "An objective method for deriving atmospheric structure from airborne lidar observations, *J. Atmos. Oceanic Technol.*, **17**, 1455-1468.

Deardorff, J.W., 1969: "Numerical study of heat transport by internal gravity waves above a growing unstable layer", *Phys. Fluids, Suppl. II*, **12**, 184-194

De Wekker, S.F.J., M. Kossmann, and F. Fielder, 1997: "Observations Of Daytime Mixed Layer heights Over Mountainous Terrain During The TRACT Field Campaign". *Proceedings of the 12th AMS Symposium on Boundary Layers and Turbulence, Vancouver, BC, Canada* (American Meteorological Society, 45 Beacon Street, Boston, MA), pp. 498-499.

De Wekker, S.F.J. D.G. Steyn, and S. Nyeki, 2004: "A Comparison of Aerosol-Layer and Convective Boundary-Layer Structure Over a Mountain Range During STAAARTE '97" *Boundary-Layer Meteorol*. **113**, 249-271.

Dörnbrack, A., Birner, T., Fix, A., Flentje, H., Meister, A., Schmid, H., Browell, E. V., and Mahoney M. J., 2002: " Evidence for inertia gravity waves forming polar stratospheric clouds over Scandinavia", *Jour. of Geoph. Resear.,* **107**, No. D20, 8287, doi:10.1029/2001JD000452

Doyle, JD, and RB Smith, 2002: "Mountain waves over the Hohe Tauern: Influence of upstream diabatic effects". *Quart. J. Roy. Meteor. Soc*., **129**, 799–824.

Dupont, E., J. Pelon, C. Flamant, 1994: "Study of the moist-convective boundary-layer structure by backscatter lidar". *Boundary-Layer Meteorol*., **69**, 1-25.

Dupont, E., Menut, L., Carissimo, C., Pelon, L., and P.H. Flamant, 1999: "Observations of the atmospheric boundary layer inParis and its rural suburbs: the ECLAP experiment," *Atmos. Envirn.*, **33**, 979-994

Fernald, F.G., 1984: Analysis of atmospheric lidar observations: some comments. *Appl. Opt.,* **23,** 652–653.

Flamant, C., J. Pelon, P.H. Flamant, and P. Durand, 1997: "Lidar determination of the entrainment zone thickness at the top of the unstable marine atmospheric boundary layer," *Bound. Layer. Meteorol*. **83**, 247-284.

Frioud, M., V. Mitev, R. Matthey, C. Häberli, H. Richner, R. Werner, and S. Vogt, 2003: "Elevated Aerosol Stratification above Rhine Valley under strong anticyclonic conditions," *Atmos. Environ*. **37**, 1785-1797.

Frioud, M., V. Mitev, R. Matthey, H. Richner, M. Furger, and S. Gubser, 2004: "Variation of the aerosol stratification over the Rhine Valley during Foehn development: a backscatter lidar study." *Meteorol. Zeitschr*. **NF 13**, 175-181.

Garratt, J.R., 1992: *The atmospheric boundary layer*. Cambridge University Press, 316.

Greenhut, G. K., and S.J.S. Khalsa, 1987: "Convective elements in the marine atmospheric boundary layer. Part I: Conditional sampling statistics.", *J. Appl. Meteor.*, **26**, 813-823.

Gubser S., Furger M., von Arx F., and H.Richner, 2001: "Wave Activity in the Boundary Layer and the Erosion of the Cold Air Pool in the Rhine Valley". *MAP Meeting 2001*, Schliersee, Germany (http://www.map.meteoswiss.ch/map-doc/NL15/abstract.htm).

Hägeli, P., 1998: "*Evaluation of a New Technique for Extracting Mixed Layer Depth and Entrainment Zone Thickness from Lidar Backscatter Profiles*". Diploma thesis at the Dept. of Geography of the Swiss Federal Institute of Technology ETHZ.

Hägeli, P., D. G. Steyn, and K. B. Strawbridge, 2000: "Spatial and temporal variability of mixed-layer depth and entrainment zone thickness". *Boundary-Layer Meteorol*. **97**, 47-71.

Hayden, K.L., K.G. Anlauf, R.M. Hoff, J.W. Strapp, J.W. Bottenheim, H.A. Wiebe, F.A. Froude, and J.B. Martin, 1997:"The Vertical chemical and Meteorological Structure of The Boundary Layer in The Lower Fraser Valley during Pacific '93". *Atmos. Environ*. **31**, 2089-2105.

Heffer, J.L., 1980: *Air Resource Laboratories Atmospheric Transport and dispersion model* NOAA Tech. Memo., ERL, ARL-81, pp 24.

Hoff, R.M., M. Harwood, A. Sheppard, F. Froude, and J.B. Martin, 1997: "Use of Airborne Lidar to Determine Aerosol Sources and Mouvement in the Lower Fraser Valley (LFV), BC". *Atmosph. Environ.* **31**, 2123-2134.

Hoopar, W.P., and E. Eloranta, 1986: "Lidar measurements of wind in the planetary boundary layer: the method, accuracy and results from joint measurements with radiosonde and kytoon". *J. Clim. Appl. Meteorol*. **25**, 990-1001.

Jelalian, A. V., 1991: "Laser Radar System", *Artech House,* London-Boston

Jensen, E., and L. Pfister. 2004. Transport and freeze-drying in the tropical tropopause layer. *J. Geophys. Res.*, **109**, doi:10.1029/2003JD004022.

Lane, T.P., M.J. Reeder, B.R. Morton and T.L. Clark. 2000: "Observations and numerical modelling of mountain waves over the Southern Alps of New Zealand". *Quart. J. Roy. Meteor. Soc.,* **126**, 2765-2788.

Luo, B. P., T. Peter, H. Wernli, S. Fueglistaler, M. Wirth, C. Kiemle, H. Flentje, V. A. Yushkov, V. Khattatov, V. Rudakov, A. Thomas, S. Borrmann, G. Toci, P. Mazzinghi,

J. Beuermann, C. Schiller, F. Cairo, G. DiDonfrancesco, A. Adriani, C. M. Volk, J. Ström, K. Noone, V. Mitev, A. R. MacKenzie, K. S. Carslaw, T. Trautmann, V. Santacesaria, and L. Stefanutti, 2003: "Dehydration potential of ultrathin clouds at the tropical tropopause," *Geophys. Res. Lett.*, **30(11)**, 1557, doi: 10.1029/2002GL016737;

Martucci, G., V. Mitev, R. Matthey, M. K. Srivastava, 2003: " Remote-Controlled automatic backscatter lidar for PBL and troposphere measurements: Description and first results", Remote Sensing Of Clouds And Atmosphere VIII: proceeding of SPIE Conference, 5235, 661-672

Martucci, G., V. Mitev, R. Matthey, 2004: "Two case studies of daily cycle PBL-dynamics over Basel: backscatter lidar measurements" *Proceeding of the 22nd International Laser Radar Conference*, **2**, 765-768

Martucci, G., R. Matthey, V. Mitev and V. Makarov, 2005: "Compact backscatter lidar for cloud detection on a stratospheric aircraft", *Remote Sensing Of Clouds And Atmosphere X: proceeding of SPIE Conference*

Martucci, G., Matthey, R., Mitev, V., Fix, A., Kiemle, C., 2006: "Detection of ultra-thin tropical cirrus during TROCCINOX: a case study performed by two airborne lidars", *Reviewed and Revised Papers Presented at the 23rd International Laser Radar Conference, Editors Chikao Nagasawa and Nobuo Sugimoto part A, Nara - Japan, 24-28 July 2006*, **ISBN 4-9902916-0-3**, 585-588.

Matthey, R., 2000: "Development of compact elastic backscatter lidar: from numerical simulation to atmospheric measurements". Travail de Thèse presenté à la faculté des Sciences de Neuchâtel, Suisse.

Matthey, R., Cacciani, M., Fiocco, G., Alfaro Martinez, A., Martucci, G., Mitev, V., Pace, G., Stefanutti, L., 2003: " Observations Of Aerosol And Clouds With The Able And Mal Lidars During The Mid-Latitude And Arctic Envisat Validation Campaigns", *16th ESA Symposium on European Rocket and Balloon Programmes and Related ResearchJune 2003, St-Gallen, Switzerland*

Matthey, R., G. Martucci, V. Mitev and V. Makarov, 2004: "Lidar detection of thin clouds from high altitude air craft M55 Geophysica", *Proceeding of the 22nd International Laser Radar Conference*, **1**, 95-98

Matthias, V., and Coauthors, 2004: "Vertical aerosol distribution over Europe: Statistical analysis of Raman lidar data from 10 European Aerosol Research Lidar Network (EARLINET) stations". *J. Geophys. Res.* **109**, No. D18, D1820110.1029/2004JD004638.

McFarquhar, G. M., A. J. Heymsfield, J. D. Spinhirne, and W. D. Hart, 2000: "Thin and subvisula tropopause tropical cirrus: Observations and radiative impacts, *J. Atmos. Sci.*, **57**, 1841-1853.

McGill, M.J., Hlavka, D.L., Hart, W.D., Scott, V.S., Spinhirne, J.D., and Schmidt, B., 2002: "Cloud Physics Lidar: Instruments description and initial measurement results." *Appl. Opt.*, **41**, 3725-3734.

McIlveen, R., 1992: *Fundamentals of Weather and Climate*. Chapman & Hall, London, Weinheim, New York, Tokyo, Melbourne, Medras.

McIlveen, R., 1992: "Airflow over uneven surfaces" in *Fundamentals of Weather and Climate* (Chapman & Hall, London, Weinheim, New York, Tokyo, Melbourne, Medras), pp. 315-317.

Measures, R. M., 1984: "Laser Remote Sensing, Fundamentals and Applications", *John Whiley & Sons*

Melfi, S.H., J. D. Spinhire, S.-H. Chou and S. P. Palm, 1985: "Lidar observation of vertically organized convection in the planetary boundary layer over the ocean". *J. Clim. Appl. Meteorol.* **24**, 806-821.

Menut, L., 1997: "Etude expérimentale et théorique de la couche limite atmosphérique en agglomeration Parisienne," Ph.D. dissertation (Université Pierre et marie Curie, Paris)

Menut, L., C. Flamant, J. Pelon, and P.H. Flamant, 1999: "Urban boundary layer height determination from lidar measurements over the Paris area". *Appl. Opt.* **38**, 945-954.

Nance, L., and D. Durran, 1997: A modeling study of nonstationary trapped mountain lee waves. Part I: Mean flow variability. *J. Atmos. Sci.,* **54,** 2275–2291.

Nance, L., and D. Durran, 1998: A modeling study of nonstationary trapped mountain lee waves. Part II: Nonlinearity. *J. Atmos. Sci.,* **55,**1429–1445.

Neu, U., T. Künzle, and H. Wanner, 1994: "On the relation between ozone storage in the residual layer and the daily variation in near-surface ozone concentration—A case study". *Bound.-Layer Meteor.,* **69,** 221–247.

Peter T., Luo B.P., Wirth M., Kiemle C., Flentje H., Yushkov, V.A., Khattatov V., Rudakov V., Thomas A., Borrmann S., Toci G., Mazzinghi P., Beuermann J., Schiller C., Cairo F., Di Donfrancesco G., Adriani A., Volk C.M., Strom J., Noone K., Mitev V., MacKenzie R.A., Carslaw K.S., Trautmann T., Santacesaria V., Stefanutti L., 2003:

"Ultrathin Tropical Tropopause Clouds (UTTCs): I. Cloud morphology and occurrence", *Atmos. Chem. Phys.,* **3,** 1083-1091.

Piironen, A.K., and E. Eloranta, 1995: "Convective boundary layer mean depths and cloud geometrical properties obtained from volume imaging lidar data". *J. Geophys. Res*. **100**, 25569-25576.

Ralph, F. M., P. J. Neiman, T. L. Keller, D. Levinson, and L. Fedor, 1997: Observations, simulations, and analysis of nonstationary trapped lee waves. *J. Atmos. Sci.,* **54,** 1308–1333.

Rampanelli G., and D. Zardi, 2004: "A method to determine the capping inversion of the convective boundary layer". *J. Appl. Meteor.* **43**, 925-933.

Raupach MR, Antonia RA, Rajagopalan S., 1991: "Rough-wall turbulent boundary layers" *Appl Mech Rev*, **44**, 1–25.

Rayment, R. and C.J. Readings 1974: "A Case Study of the Structure and Energetics of an Inver-. sion", *Quart. J. Roy. Meteorol. Sot.*, **100**, 221-233.

Rotach, M.R., R. Vogt, C. Bernhofer, E. Batcharova, A. Christen, A. Clappier, B. Feddersen, S.-E. Gryning, G. Martucci, H. Mayer, V. Mitev, T.R. Oke, E. Parlow, H. Richner, M. Roth, Y.-A. Roulet, D. Ruffieux, J.A. Salmond, M. Schaltzmann, and J.A. Voogt, 2005: "BUBBLE – anUrban Boundary-Layer Meteorology Project", *Theor. and Appl. Climat.*, **81**, 231-261

Russel, P.B., E.E. Uthe, F.L. Ludwig and N.A. Shaw, 1974: "A comparison of atmospheric structure as observed with monostatic acoustic sounder and lidar technique". *J. Geophys. Res*. **79**, 5555-5566

Salby, M.L., 1996: "*Foundamentals of Atmospheric physics*". Academic Press, New York.

Saleh, B.E.A., Teich, M.C., 1991: "Fundamentals of photonics", *John Whiley & Sons*

Schreiner J., Voigt C., Kohlmann A., Anold F., Mauersberger K., Larsen N., 1999: "Chemical analysis of polar stratospheric cloud particles", *Science*, **283** (5404), 968-970

Scorer, R.S., 1957: "Experiments on convection of isolated masses of buoyant fluid", *J. Flui Mech.*, **2**, 583-594

Siebert, P., F. Beyrich, S.E. Gryning, S. Joffre, A. Rasmussen, and Ph. Tercier, 2001: “Review and intercomparison of operational methods for the determination of the mixing height,” *Atmos. Environ.* **34**, 1001-1027.

Smith, R. B., Skubis, S., Doyle, J. D., Broad, A. S., Kiemle, C., Volkert, H., 2002: "Mountain Waves over Mont Blanc: Influence of a Stagnant Boundary Layer". *Jour. of the Atmos. Scie.*, **59**, 2073-2092

Stein, B., C. Wedekind, H. Wille, F. Immler, M. Muller, L. Woste, M delGuasta, M. Morandi, L. Stefanutti, A. Antonelli, P. Agostini, V. Rizi, G. Readelli, V. Mitev, R. Matthey, R. Kivi, E. Kyro, 1999: "Optical classication, existence temperatures, and coexistence of different polar stratospheric clouds." *J. Geophys. Res*., **104**, 23983-23993.

Steyn, D.G., M. Baldi, and R. M. Hoff, 1998: "A New Technique to Derive Mixed Layer Depth and Entrainment Zone Thickness from Lidar Profiles". *Abstracts of Papers of the 19th International Laser Radar Conference (ILRC), Annapolis - USA, 6-10 July 1998,* pp. 461-464.

Steyn, D.G., M. Baldi, and R. M. Hoff, 1999: "The detection of mixed layer depth and entrainment zone thickness from lidar backscatter profiles", *J. Atmos. Oceanic Technol.* **16**, 953-959.

Stull, R.B., 1973: "Inversion rise model based on penetrative convection.", *J. Atmos. Sci.*, **30**, 1092-1099

Stull, R.B., 1988: *An introduction to boundary layer meteorology*. Kluwer Academic Publishers, P.O. Box 17, NL-3300 Dordrecht, The Netherland.

Stull, R.B., 1988:“Prognostic Equations for Turbulent Fluxes and Variances” in *An introduction to boundary layer meteorology* (Kluwer Academic Publishers, P O Box 17, 3300, AA Dordrecht, The Netherlands. 1988), pp 117-120.

Svendsen, S.H., Larsen, N., Knudsen, B., Eckermann, S.D., Browell, E.V., 2005: "Influence of mountain waves and NAT nucleation mechanisms on polar stratospheric cloud formation at local and synoptic scales during the 1999-2000 Arctic winter". *Atmosph. Chem. And Phys.*, **5**: 739-753.

Tilmes, S., Müller, R., Grooß, J., Höpfner, M., Toon, G. and Russell, J., 2004: "Correction to Very early chlorine activation and ozone loss in the Arctic winter 2002-2003." *Geophysical Research Letters*, **30**(18): doi: 10.1029/2004GL021347. issn: 0094-8276.

Ting, C.L., and D.R. Hay, 1973: " On the Heat Flux and Friction Velocity in Free Convection Near the Ground", *J. of the Atm. Sci.*, **32**, 637-638

Van Pul, W.A.J., and A.A.M. Holtslag, 1994: "A Comparison of ABL-heights Inferred Routinely from Lidar and Radiosondes at Noontime", *Boundary-Layer Meteorol.* **68**, 173-191.

Voigt C., J. Schreiner, A. Kohlmann, P. Zink, K. Mauersberger, N. Larsen, T.Deshler, C. Kröger, J. Rosen, A. Adriani, F. Cairo, G. Di Donfrancesco, M. Viterbini, J. Ovarlez, H. Ovarlez, C. David, A. Dörnbrack, 2000: "Nitric acid trihydrate (NAT) in polar stratospheric cloud particles", *Science*, **290**, 1756

Yariv, A., 1991: "Optical Electronics", 4th edition, *Sounders College Publishing*

Young, G. S., 1988: Convection in the atmospheric boundary layer. *Earth. Sci. Rev.,* **25,** 179-198.

Young, G. S., 1988: Turbulence structure of the convective boundary layer I: Variability of Normalized Turbulence Statistics. *J. Atmos. Sci.,* **45,** 719-726.

Young, G. S., 1988: Turbulence structure of the convective boundary layer II: PHOENIX 78 aircraft observations of thermals and their environment. *J. Atmos. Sci.,* **45,** 727-735.

Young, G. S., Cameron, B. K., and Hebble, E. E., 1999: "Observations of the Entrainment Zone in a Rapidly Entraining Boundary Layer", *Jour. of the Atmos. Scie.s:* **57**, No. 18, pp. 3145–3160

Wallace, J.M., and P.V. Hobbs, 1977: *Atmospheric Science - An Introductory Survey*. Academic Press, New York.

Wandinger, U., 2005: "Introduction to lidar" in *Lidar: Range-Resolved Optical Remote Sensing of the Atmosphere* (Weitkamp, C., Editor, Springer Series of Optical Sciences vol. 102)

Weitkamp, C., 2005: *Lidar: Range-Resolved Optical Remote Sensing of the Atmosphere*, Springer Series of Optical Sciences vol. 102.

Werne, J., 1994: "Plume model for the boundary layer dynamics in hard turbulence." *Phys. Rev.*, **E 49**, 4072–4076.

World Meteorological Organisation, 1999: "Scientific assessment of ozone depletion", Rep. 44, Geneva.

Zampieri, M., P. Malguzzi, and A. Buzzi, 2005: "Sensitivity of quantitative precipitation forecast to boundary layer parameterization: a flash flood case study in the Western Mediterranean", *Natural Hazards and Earth Sys. Scie.* **5**, 603-612.

List of Publications

Lionello, P., Martucci, G., Zampieri, M., 2003: "Implementation of coupled atmosphere-wave-ocean model in the Mediterranean Sea: sensitivity of the short time scale evolution to the air-sea coupling mechanism", *The Global Atmosph. and Ocean System*, **9**, 65-95

Calheiros, R.V., Held, G., Mitev, V., Antonio, C. A. de A., Martucci G., and R. Matthey, 2005: "Ground and airborne validation plans for GPM in the central State of São Paulo, Brazil", *Proceeding of the 32nd Conference on Radar Meteorology, AMS, Albuquerque, USA*

Martucci, G., Srivastava, M. J. K., Mitev, V., Matthey, R., Frioud, M., and H. Richner, 2003:" Comparison of lidar methods to determine the Aerosol Mixed Layer top", *Remote Sensing Of Clouds And Atmosphere VIII: proceeding of SPIE Conference*, **5235**, 447-456

Martucci, G., V. Mitev, R. Matthey, M. K. Srivastava, 2003: " Remote-Controlled automatic backscatter lidar for PBL and troposphere measurements: Description and first results", Remote Sensing Of Clouds And Atmosphere VIII: proceeding of SPIE Conference, **5235**, 661-672

Martucci, G., V. Mitev, R. Matthey, 2004: "Two case studies of daily cycle PBL-dynamics over Basel: backscatter lidar measurements" *Proceeding of the 22nd International Laser Radar Conference*, **2**, 765-768

Martucci, G., R. Matthey, V. Mitev and V. Makarov, 2005: "Compact backscatter lidar for cloud detection on a stratospheric aircraft", *Remote Sensing Of Clouds And Atmosphere X: proceeding of SPIE Conference*

Martucci, G., Mitev ,V., Matthey, R., and H. Richner, 2005: " Lidar determination of mixing layer height with high resolution " *Remote Sensing Of Clouds And Atmosphere X: proceeding of SPIE Conference*

Martucci, G., Matthey, R., Mitev ,V., and H. Richner, "Comparison between backscatter lidar and radiosonde measurements of the diurnal and nocturnal stratification in the lower troposphere". **Submitted to *Journal of Atmospheric and Oceanic Technology* (March 2006)** :

Matthey, R., G. Martucci, V. Mitev and V. Makarov, 2004: "Lidar detection of thin clouds from high altitude air craft M55 Geophysica", *Proceeding of the 22nd International Laser Radar Conference*, **1**, 95-98

Rotach, M.R., R. Vogt, C. Bernhofer, E. Batcharova, A. Christen, A. Clappier, B. Feddersen, S.-E. Gryning, G. Martucci, H. Mayer, V. Mitev, T.R. Oke, E. Parlow, H. Richner, M. Roth, Y.-A. Roulet, D. Ruffieux, J.A. Salmond, M. Schaltzmann, and J.A. Voogt, 2005: "BUBBLE – anUrban Boundary-Layer Meteorology Project", *Theor. and Appl. Climat.*, **81**, 231-261